

# **Quantum Mechanical Modeling of Surface Reactions in Storage Catalytic Converters**

**INAUGURAL-DISSERTATION**

submitted to the

Faculty of Chemistry and Geosciences  
of the Rupertus-Carola University of Heidelberg, Germany

for the degree of  
Doctor of Natural Sciences

presented by

Monica Țuțuianu, M. Sc. Chem. Eng.

born in Galați, Romania

Examiners: Prof. Dr. Dr. h. c. Jürgen Warnatz

Prof. Dr. Olaf Deutschmann

Heidelberg, 13<sup>th</sup> of July 2007

**Interdisziplinäres Zentrum für Wissenschaftliches Rechnen**

**Ruprecht-Karls-Universität Heidelberg**

**2007**



**INAUGURAL-DISSERTATION**

submitted to the

Faculty of Chemistry and Geosciences  
of the Rupertus-Carola University of Heidelberg, Germany

for the degree of  
Doctor of Natural Sciences

presented by

Monica Țuțuianu, M. Sc. Chem. Eng.

born in Galați, Romania



# **Quantum Mechanical Modeling of Surface Reactions in Storage Catalytic Converters**

Examiners: Prof. Dr. Dr. h. c. Jürgen Warnatz

Prof. Dr. Olaf Deutschmann



**To my family**





## ***Abstract***

Pollutant reduction of internal combustion engines plays an essential role in automotive industry research and development. Exhaust-gas after-treatment using catalytic converters is of key importance to this goal. Storage catalytic converters based on barium oxide are a technology with promising potential to meet current and future emission standards for nitric oxides (NO<sub>x</sub>) abatement of lean-burning gasoline and Diesel engines.

The aim of this work was to develop elementary reaction steps and determine kinetic parameters for the NO<sub>x</sub> storage reaction mechanism by means of *density functional theory* (DFT). DFT has proven a powerful tool in investigating microscopic aspects of heterogeneous reactions. Electronic structure calculations were performed for adsorption of different molecules on two surfaces relevant in automotive exhaust gas purification: barium oxide and platinum.

The interaction of different species (NO, NO<sub>2</sub>, CO<sub>2</sub>, H<sub>2</sub>O) with the BaO(100) surface was investigated in terms of adsorption site and adsorption geometry in dependence on surface coverage. It could be shown that all species form stable adsorbates and adsorption strength increases in the order NO<sub>2</sub> < H<sub>2</sub>O < NO ≤ CO<sub>2</sub>. It was found that high coverages strongly reduce the adsorption energy.

Oxygen adsorption, decomposition and diffusion on Pt(111) have been studied. Kinetic parameters of the reactions of oxygen and the diffusion of atomic oxygen on the surface and their dependence on surface coverage were determined. It was found that molecular adsorption of oxygen molecules on a clean surface has a more favorable configuration in the side-on geometry. The decomposition process is favored at low surface coverages while at higher coverages it is inhibited. Furthermore, the surface diffusion of atomic oxygen from an fcc threefold site to a hcp threefold site was investigated. A strong dependence on surface coverage was observed with activation energies increasing with increasing coverages. Moreover, the influence of various coadsorbates on surface diffusion of atomic oxygen was

presented. A linear relationship between the coadsorbate's electronegativity and the reaction energy was observed.

The kinetic data obtained by DFT investigations were used in a thermodynamic study of the BaO surface state under realistic operating conditions. Numerical calculations of the competitive adsorption/desorption equilibria of NO, NO<sub>2</sub>, CO<sub>2</sub>, H<sub>2</sub>O for a typical exhaust gas composition showed that CO<sub>2</sub> plays an essential role in the surface processes during NO<sub>x</sub> storage on BaO. Furthermore, the DFT results obtained were used in a kinetic model of oxygen surface reaction mechanism on platinum applied in NSR catalysis. The study was performed in order to better understand the properties of the oxygen spillover reaction as well as its coupling with surface transport (diffusion).

This thesis presents a detailed quantum chemical study of surface processes relevant in storage catalytic converters. The study allows a valuable insight into the processes that govern and potentially limit these types of catalysts.

## ***Kurzfassung***

Die Reduktion der Schadstoffemissionen von Verbrennungsmotoren spielt eine herausragende Rolle in der Forschung der Automobilbranche. Eine wichtige Rolle spielt dabei die Abgasnachbehandlung mittels Katalysatoren. Bariumoxid-basierte Stickoxid-(NO<sub>x</sub>)-Speicher-katalysatoren sind eine vielversprechende Technologie zum Erreichen aktueller und zukünftiger Emissionsziele von mager-verbrennenden Otto- und Dieselmotoren.

Ziel dieser Arbeit ist es, elementare Reaktionsschritte für den NO<sub>x</sub>-Speichermechanismus und deren kinetische Parameter mit Hilfe der Dichtefunktionaltheorie (DFT) zu bestimmen. Die DFT hat sich als leistungsfähiges Werkzeug für die Untersuchung mikroskopischer Aspekte heterogener Reaktionen erwiesen. Berechnungen elektronischer Strukturen wurden für die Adsorption verschiedener Moleküle auf zwei für die Autoabgasreinigung relevanten Oberflächen - Bariumoxid und Platin - durchgeführt.

Die Wechselwirkungen verschiedener Spezies (NO, NO<sub>2</sub>, CO<sub>2</sub>, H<sub>2</sub>O) mit der BaO(100)-Oberfläche wurde in Bezug auf Adsorptionsplätze und Adsorptionsgeometrie in Abhängigkeit von der Oberflächenbedeckung untersucht. Es konnte gezeigt werden, dass alle Spezies stabile Adsorbate bilden und dass die Adsorptionsenergie in der Reihenfolge NO<sub>2</sub> < H<sub>2</sub>O < NO ≤ CO<sub>2</sub> ansteigt. Hohe Bedeckungen haben dabei eine starke Reduktion der Adsorptionsenergie zur Folge.

Adsorption, Dissoziation und Diffusion von Sauerstoff auf Pt(111) wurden untersucht. Kinetische Parameter der Reaktionen von molekularem Sauerstoff und der Diffusion von Sauerstoff-Atomen sowie deren Abhängigkeit von der Oberflächenbedeckung wurden bestimmt. Es wurde beobachtet, dass die molekulare Adsorption von Sauerstoff auf einer sauberen Oberfläche in einer side-on Geometrie erfolgt. Die Dissoziation wird bei niedrigen Oberflächenbedeckungen favorisiert, während sie bei höheren Bedeckungen gehemmt wird. Außerdem wurde die Oberflächendiffusion von atomarem Sauerstoff zwischen fcc- und hcp-Adsorptionsplätzen untersucht. Auch hier wurde eine starke Abhängigkeit von der Oberflächenbedeckung beobachtet. Des Weiteren wurde der Einfluss verschiedener

Koadsorbate auf die Oberflächendiffusion untersucht. Dabei konnte eine lineare Relation zwischen der Elektronegativität der Koadsorbate und der Aktivierungsbarriere festgestellt werden.

Die durch DFT-Untersuchungen erhaltenen Daten wurden für eine thermodynamische Untersuchung des BaO-Oberflächenzustandes unter realistischen Betriebsbedingungen verwendet. Numerische Simulationen der kompetitiven Adsorptions/Desorptionsgleichgewichte von NO, NO<sub>2</sub>, CO<sub>2</sub>, und H<sub>2</sub>O für eine typische Abgaszusammensetzung zeigen, dass CO<sub>2</sub> eine wichtige Rolle für die Oberflächenprozesse während der Speicherung von NO<sub>x</sub> auf BaO spielt. Weiterhin wurden die durch DFT erhaltenen Ergebnisse in einem kinetischen Modell von Sauerstoffreaktionen auf einer Platinoberfläche verwendet. Diese Studie wurde durchgeführt, um sowohl die Eigenschaften von Sauerstoff-Spillover als auch dessen Kopplung mit Oberflächentransport besser zu verstehen.

Diese Arbeit stellt eine detaillierte quantenchemische Studie von Oberflächenprozessen vor, die in Speicherkatalysatoren relevant sind. Die Studie erlaubt wertvolle Einblicke in die Prozesse, die die katalytische Aktivität beeinflussen und möglicherweise einschränken.

---

## Table of Content

### Chapter 1 Introduction

1.1 Vehicle Emissions and Environmental Problems.....	1
1.2 After-treatment Systems and Vehicle Emissions Legislations .....	2
1.3 Cleaning Methods for Toxic Emissions.....	6
1.3.1 Methods of NO <sub>x</sub> Reduction at Oxidizing Conditions.....	6
1.3.2 Non-Thermal Plasma Technology.....	9
1.3.3 Methods for Soot Removal.....	9
1.4 Multi-scale Modeling in Heterogeneous Catalysis.....	11
1.5 Scope and Content of this Thesis.....	13

### Chapter 2 Quantum Mechanics

2.1 The Schrödinger Equation.....	16
2.2 The Born-Oppenheimer Approximation.....	17
2.3 The Density Functional Theory (DFT).....	18
2.3.1 Kohn-Sham Equation.....	19
2.3.2 The Exchange-Correlation Functional.....	20
2.4 DFT Implementation in the CASTEP Code.....	21
2.4.1 “Supercell” Approach.....	22
2.4.2 The Plane-Wave Basis Set.....	24
2.4.3 Pseudo-Wave Function and Pseudo-Potential Approximation.....	26
2.4.4 Brillouin-Zone Sampling.....	27
2.4.5 Mulliken Charge Analysis.....	28
2.5 Calculation of Magnetic Moment.....	29

**Chapter 3 Sensitivity of Calculations Results on DFT Parameters**

3.1	Energy Dependence on Vacuum Thickness.....	31
3.2	Energy Dependence on $k$ -point Spacing.....	32
3.3	Energy Dependence on Cut-off Energy.....	33
3.4	Surface Structural Relaxation.....	34
3.5	Influence of Spin Effect and Surface Relaxation on the Calculations.....	39
3.6	Computational Time of CASTEP Calculations – Examples.....	42

**Chapter 4 NO, NO<sub>2</sub>, CO<sub>2</sub> and H<sub>2</sub>O Adsorption on BaO(100)**

4.1	Pure Bulk and Gas-phase Species.....	48
4.2	Nitrogen Monoxide (NO) Adsorption.....	48
4.3	Nitrogen Dioxide (NO <sub>2</sub> ) Adsorption.....	52
4.4	Carbon Dioxide (CO <sub>2</sub> ) Adsorption.....	55
4.5	Water Adsorption (H <sub>2</sub> O).....	61
4.6	Comparison to Previous DFT Studies.....	65
4.7	Linear Fit of the Coverage Dependence of NO, NO <sub>2</sub> , CO <sub>2</sub> and H <sub>2</sub> O.....	68
4.8	Conclusions.....	69

**Chapter 5 Oxygen Adsorption, Dissociation and Surface Diffusion on Pt(111)**

5.1	Platinum Bulk and Molecular Oxygen.....	72
5.2	Molecular Oxygen Adsorption on Pt (111).....	72
5.3	Molecular Oxygen Decomposition.....	78
5.4	Atomic Oxygen Adsorption on Platinum (111).....	82
5.5	Surface Diffusion of Atomic Oxygen.....	85
5.6	Influence of Coadsorbates on the Surface Diffusion of Atomic Oxygen.....	86
5.7	Conclusions.....	89

---

**Chapter 6 Simulations of Surface Coverages and Transport Processes**

6.1	Thermodynamic Simulation of the BaO Surface Coverage.....	91
6.1.1	Conclusions.....	96
6.2	Kinetic Simulation of Oxygen Reaction and Spillover Processes on Pt.....	96
6.2.1	Background.....	96
6.2.2	Simulations of Pt(111) Reaction, Diffusion and Spillover .....	98
6.2.3	Application of DFT Results.....	103
6.2.4	Conclusions.....	108
<b>Chapter 7 Summary.....</b>		<b>109</b>
<b>References.....</b>		<b>111</b>
<b>List of Publications.....</b>		<b>123</b>
<b>Appendix A: Estimation of the Adsorption Entropy.....</b>		<b>125</b>
<b>Appendix B: Calculation of Atomic Oxygen Diffusion Coefficients.....</b>		<b>127</b>
<b>Appendix C: Atom Coloring in Surface Visualizations .....</b>		<b>131</b>
<b>Acknowledgments.....</b>		<b>133</b>





## ***Chapter 1: Introduction***

### **1.1 Vehicle Emissions and Environmental Problems**

Atmospheric pollution is nowadays one of the most important problems concerning our environment. There are two main pollution sources responsible for this phenomenon: the mobile sources (e.g., passenger cars, trucks, trains, ships, aircrafts etc.) and the stationary sources such as industry (e.g., power plants) or natural sources (e.g., volcanoes). The main pollutants emitted in the atmosphere are carbon oxides (CO, CO<sub>2</sub>), nitrogen oxides (NO, NO<sub>2</sub>, N<sub>2</sub>O), sulfur oxides (SO<sub>2</sub>, SO<sub>3</sub>), volatile organic compounds (VOC), and solid particles (e.g., soot) known also as particulate matter (PM). The applicability of this work is on automotive catalysis, therefore in this chapter the focus is on the effects due to the mobile emissions sources and on the methods used for their reductions.

The internal combustion engines' emissions have a large contribution to the total amount of main gases responsible for the green house effect, carbon dioxide (CO<sub>2</sub>) and the nitrous oxide (N<sub>2</sub>O). The other pollutants from the automotive exhaust gas such as carbon monoxide (CO), nitrogen oxides (NO and NO<sub>2</sub>), the unburned hydrocarbons (HC), sulfur oxides (SO<sub>x</sub><sup>a</sup>) and solid particles have also a harmful effect on the environment as well as on human health. Volatile organic compounds and soot are toxic for mankind, having a carcinogenic effect; the sulfur oxides are responsible for the acid rain (leading to acidification of soil and forest degradation); the nitrogen oxides are harmful for the human respiratory and defence systems and they also have contributions to acid rain, smog formation and the depletion of the stratospheric ozone layer.

---

<sup>a</sup> SO<sub>x</sub> is an abbreviation for a mixture of SO<sub>2</sub> and SO<sub>3</sub>.

The exhaust gas is a complex mixture, the composition depending strongly on the type of engine and on the operating conditions of the after-treatment systems. Table 1.1 shows a typical composition of the exhaust gas of different engines.

	CO (%)	HC (ppm C)	NO <sub>x</sub> (ppm)	PM (g/kWh)	O <sub>2</sub> (%)
Diesel	0.01-0.2	100-2000	200-1000	0.15-0.5	3-15
Otto lean-burn	0.05-0.5	1000-5000	100-1000	-	0.5-5
Otto	0.3-1	1000-5000	50-2500	-	0.1-0.5

**Table 1.1:** Exhaust gas composition for different types of engines. Adapted from Koltsakis *et al.* [1].

## 1.2 After-treatment Systems and Vehicle Emissions Legislations

The negative impact of the toxic emissions has led to the introduction of exhaust emission legislations and to the development of after-treatment systems.

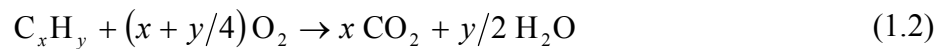
The first step towards reduction of the toxic pollutants from passenger cars was done in 1975 in USA. The technology used for emission control systems employed an oxidation catalyst for the oxidation of carbon monoxide (CO) and unburned hydrocarbons (HC). A typical oxidation catalyst consists of precious metals such as platinum (Pt) and palladium (Pd) supported on fine particles of high-surface-area  $\gamma$ -alumina, which are then coated onto porous alumina pellets or a monolith.

In the 1980s a new generation of automotive catalysts, the so-called three-way catalysts (TWC), was developed and extended also in Japan and Europe. The three-way catalysts were employed in order to reduce also NO<sub>x</sub><sup>b</sup> emissions from the exhaust gas, in addition to CO and HC removal. Under stoichiometric conditions, the TWC catalysts convert simultaneously CO, HC and NO<sub>x</sub> into CO<sub>2</sub>, H<sub>2</sub>O and N<sub>2</sub>, according to the following overall oxidation and reduction reactions:

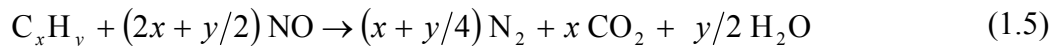
---

<sup>b</sup> NO<sub>x</sub> is an abbreviation for a mixture of NO and NO<sub>2</sub>.

Oxidation reactions:



Reduction reactions:



The exhaust gas purification system consists of a catalytic converter and an oxygen sensor which measures the oxygen content so that a stoichiometric ratio between air and fuel is provided. The three-way catalytic converter is a stainless steel container which incorporates a honeycomb monolith made of cordierite<sup>c</sup> or metal. The catalyst is a multi-component material containing the precious materials platinum, rhodium, and a smaller amount of palladium, supported on  $\gamma$ -alumina and other metal oxides (e.g. BaO, CeO<sub>2</sub>).

The first drawback of this technology is the control of the air-to-fuel ratio within a narrow window (so-called lambda window) around the stoichiometric value of 14.6 (cf. Fig. 1.1). Within the lambda window, a high conversion (> 80%) of CO, HC and NO<sub>x</sub> is achieved simultaneously. At air-to-fuel ratios lower than 14.6 (fuel-rich<sup>d</sup> conditions, i.e. insufficient air) the combustion process is incomplete and the exhaust gas contains high amounts of hydrocarbons (HC) and carbon monoxide (CO). At stoichiometric conditions as well as at air-to-fuel ratios higher than 14.6 (fuel-lean<sup>e</sup> conditions, i.e. excess of oxygen) the amount of CO<sub>2</sub> and NO<sub>x</sub> increases while the CO, HC and partial oxidation compounds decrease.

The second drawback of the three-way catalyst is the high temperature ( $T > 550 \text{ K}$ ) needed to work properly otherwise the pollutants from the exhaust gas are released into the

---

<sup>c</sup> Cordierite is a magnesium aluminosilicate with the chemical formula  $2\text{MgO} \cdot 2\text{Al}_2\text{O}_3 \cdot 5\text{SiO}_2$ .

<sup>d</sup> Fuel-rich conditions mean excess of CO, HC and H<sub>2</sub> in the exhaust gas.

<sup>e</sup> Fuel-lean conditions mean excess of O<sub>2</sub> in the exhaust gas.

atmosphere unconverted. This deficiency is known as the cold-start behavior<sup>f</sup> of automotive three-way catalysts.

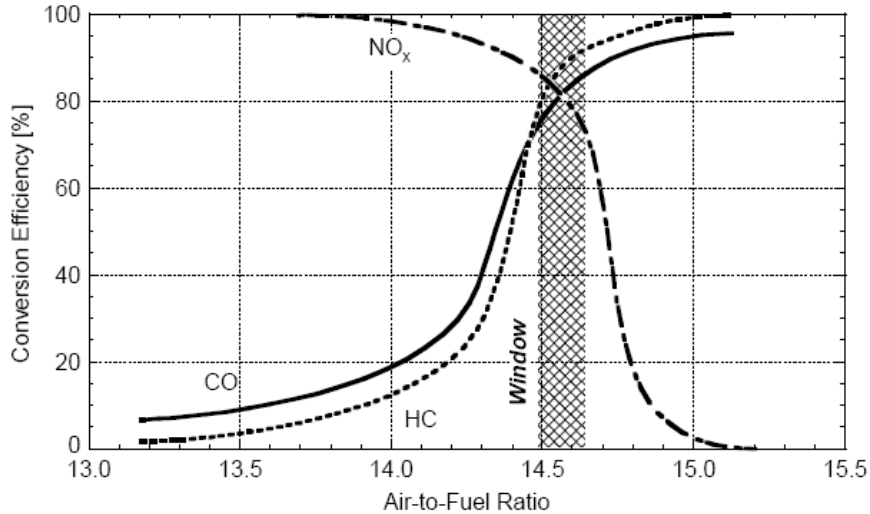


**Fig. 1.1:** The CO, HC and NO<sub>x</sub> conversion efficiency dependence on air-to-fuel ratio. Stoichiometric combustion corresponds to a ratio of 14.7 g of air for each gram of gasoline fuel [2].

Following the restrictions in the 1990s, due to the fast increase of the passenger cars production, more stringent emissions limits on NO<sub>x</sub>, CO and HC from vehicle engines have been introduced by the European Commission. In 2000 the Euro-3 norm was introduced, followed up by the Euro-4 norm in 2005. The next step proposed for lower emission standards, the Euro-5 norm, is scheduled for either 2008 or 2009. The limits imposed by these norms for Diesel and gasoline passenger cars are shown in Table 1.2.

<sup>f</sup> Cold-start behavior is the time period right after the engine starts until the catalyst becomes active ( $T = 200\text{ }^{\circ}\text{C}$ ).

	Euro-nom	Year	CO (g/km)	HC (g/km)	HC + NO <sub>x</sub> (g/km)	NO <sub>x</sub> (g/km)	PM (g/km)
Diesel	Euro-3	2000	0.64	-	0.56	0.50	0.05
	Euro-4	2005	0.50	-	0.30	0.25	0.025
	Euro 5	2009	0.50	-	0.25	0.20	0.005
Gasoline	Euro-3	2000	2.30	0.20	-	0.15	-
	Euro-4	2005	1.0	0.10	-	0.08	-
	Euro 5	2009	1.0	0.075	-	0.06	0.005

**Table 1.2:** Limits of the Euro-3, Euro-4 and Euro-5 norms for Diesel and gasoline passenger cars [3-5].

Due to several political decisions, further reduction of the emissions from internal combustion engines could be achieved. In 1997 the Kyoto Protocol was approved implying an agreement between 129 countries on reducing green house gases emissions.

These strategies have been employed not only for reduction of the toxic emissions, but in conjunction with improvement of the fuel consumption. Therefore, new concepts of the catalytic converters have been developed.

One of the most promising approaches for fuel efficiency and reduced CO<sub>2</sub> emissions of combustion engines is the lean-burn gasoline or Diesel engine technology. These engines are operated under oxidizing conditions (using excess of oxygen, air-to-fuel ratios of 25:1 and above, while for stoichiometric engines air-to-fuel ratios of 14.5:1 are used) which improve the fuel consumption up to 30% compared with stoichiometric engines [6] and implicitly reduce the CO<sub>2</sub> emissions. Very low emissions of CO and relatively low HC emissions are attained that can further be reduced by a three-way catalyst under oxidizing conditions. However, the lean-burn concept is problematic for reducing the nitrogen oxides (NO<sub>x</sub>) using the conventional three-way catalysts. Another drawback of these engines is that considerable amounts of soot can be formed. Therefore, several approaches to remove soot and reduce NO<sub>x</sub> from the exhaust gas at oxidizing (lean) conditions were developed.

## 1.3 Cleaning Methods for Toxic Emissions

### 1.3.1 Methods of NO<sub>x</sub> Reduction at Oxidizing Conditions

Two major catalytic technologies have been developed for reducing nitrogen oxides in an oxidizing environment. The first is the selective catalytic reduction (SCR) [7] approach, using ammonia or hydrocarbons (HC) as reductant and the second is the NO<sub>x</sub> storage and reduction (NSR) [8,9] approach.

#### *1) The Selective Catalytic Reduction (SCR)*

The SCR method uses an external reductant, such as urea (CO(NH<sub>2</sub>)<sub>2</sub>), ammonia (NH<sub>3</sub>) or fuel (HC), for converting the toxic NO<sub>x</sub> into N<sub>2</sub>.

#### *a) Urea/NH<sub>3</sub> Selective Catalytic Reduction*

Depending on the area of application, several N-containing reductants such as urea, cyanuric acid, or ammonia have been proposed to be used for selective catalytic reduction of NO<sub>x</sub> emissions. However, the one used most in practice is NH<sub>3</sub>. The NO is converted into N<sub>2</sub>, according to the following overall reaction:



The selective catalytic reduction of NO<sub>x</sub> with ammonia is mainly applied to small stationary engines or power plants. Generally, liquid ammonia is injected into the exhaust gas before the catalyst. The catalysts used in the SCR of NO<sub>x</sub> with NH<sub>3</sub> are metal oxides, supported noble metals and metal zeolites. The main drawbacks of this technology are the need to store ammonia and the infra-structure for its distribution. Additionally, the method is limited due to the possible formation of ammonium sulphates.

### b) *Hydrocarbon Selective Catalytic Reduction (HC-SCR)*

The selective catalytic reduction with hydrocarbons uses the hydrocarbons contained in the exhaust gas to reduce  $\text{NO}_x$  into  $\text{N}_2$  under catalyzed conditions. However, as the exhaust gas from internal combustion engines contains only low levels of CO and HC under oxidizing operating conditions, only small amounts of  $\text{NO}_x$  could be reduced without additional reductant. The active catalysts used for  $\text{NO}_x$  conversion with HC are noble metals (e.g., Pt, Pd, Rh, Ir), metal oxides supported on silica or alumina, or transition metals (e.g., Co or Cu) supported on zeolites. The major drawbacks of this approach are the low durability (especially at high temperature) and the low resistance towards sulphur poisoning. Moreover, the green-house gas nitrous oxide (due to incomplete reduction) is also formed.

### II) *$\text{NO}_x$ Storage and Reduction (NSR)*

The  $\text{NO}_x$  storage and reduction catalytic converters offer high promise for current and future nitric oxides ( $\text{NO}_x$ ) abatement technology from lean-burning engine exhaust. The operation principle is based on periodic long lean (storage of  $\text{NO}_x$  into the catalyst  $\sim 60$  seconds) and short rich (release of  $\text{NO}_x$  from the catalyst and reduction  $\sim 5$  seconds) engine combustion phases [9,10]. In NSR catalytic converters, a material with storage potential, e.g., metal oxides BaO,  $\text{CeO}_2$ , is included into the catalysts, and its storage function is combined with the mixed operation condition of the engine. These materials are considered to improve the  $de\text{NO}_x$  activity (removal of nitric oxides) as well as the cold-start behavior of automotive catalysts. The catalyst consists of noble metals for the three-way function, metal oxides for the storage function and  $\gamma$ -alumina as high-surface-area support.

During the lean phase, the  $\text{NO}_x$  from the engine, mainly in the form of NO, is oxidized to  $\text{NO}_2$  on the noble metal component (Pt) and stored in the storage component as nitrite and nitrate. When the storage component is saturated, the catalyst is regenerated by briefly switching the engine operation to fuel-rich conditions. Under rich condition, the stored  $\text{NO}_x$  is released and reduced on the noble metal sites using the excess components CO, HC and  $\text{H}_2$  to form  $\text{N}_2$ ,  $\text{CO}_2$  and  $\text{H}_2\text{O}$ . The  $\text{NO}_x$  storage and reduction principle is illustrated in Fig. 1.2.

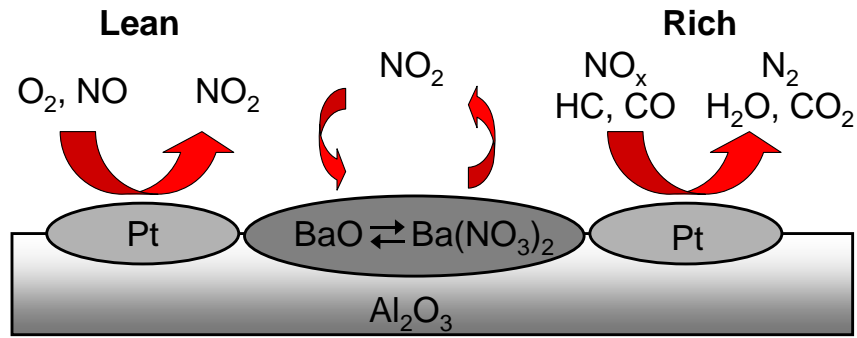
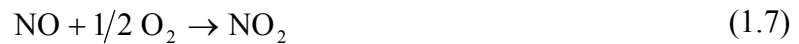


**Fig. 1.2:** NO<sub>x</sub> storage and reduction mechanism.

The NO<sub>x</sub> storage and reduction reaction mechanism can be divided in four steps:

Under net oxidizing (lean) conditions:

- *NO oxidation to NO<sub>2</sub> on platinum:*



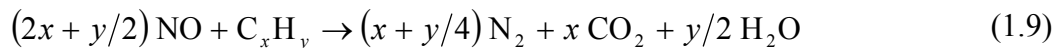
- *NO<sub>2</sub> storage on BaO:* Different mechanisms have been proposed in the literature. They are presented in more detail in Chapter 4.

Under rich condition:

- *Regeneration of the storage component:*



- *NO<sub>x</sub> reduction to N<sub>2</sub>:*



High fuel efficiency and low NO<sub>x</sub> emissions are obtained applying this concept. However, the major problem of the NSR catalysts is the sulphur poisoning due to the sulphur species (SO<sub>x</sub>) present in the fuel and in the exhaust gas. The storage component forms stable sulfate which accumulate in the catalyst and reduces its storage capacity. Accordingly, lower



emissions can be obtained by reducing the sulphur content in the fuel. Therefore, a further improvement of fuel composition and of the catalyst technology is required for the NSR concept.

### 1.3.2 Non-Thermal Plasma Technology

An effective method used for  $\text{NO}_x$  removal from the exhaust gas of internal combustion engines (especially for Diesel engines) is based on non-thermal plasma technology [11-13]. The plasma can be produced by electrical discharge methods such as pulsed corona [14] and dielectric-barrier discharge [15] techniques. The technology uses a plasma reactor (or a combination of a plasma reactor and a catalyst), and the exhaust gas is lead through the reactor with the non-thermal plasma inside. High energy electrons are produced in the exhaust gas, and the collisions of the energetic electrons with the neutral gas molecules generate chemically active species (radicals, excited molecules) that undergo further chemical reactions, leading to dissociation of gaseous pollutants ( $\text{NO}_x$ ,  $\text{SO}_x$ ,  $\text{C}_x\text{H}_y$ , etc).

A non-thermal plasma reactor can also be used as particulate matter (PM) trap. Another advantage of this technology is the high efficiency during the cold-start period.

### 1.3.3 Methods for Soot Removal

#### *a) Diesel Particulate Filter*

Diesel engines have several advantages over their gasoline counterparts, such as: higher thermal efficiencies, better durability and reliability, higher tolerance to fuel properties and higher fuel efficiency. However, Diesel emissions are characterized by a significant level of particulate matter and nitrogen oxides ( $\text{NO}_x$ ). The “particulate” refers to combustion products such as carbon-based particles, sulphates, nitrates, etc. The larger particles are observed as “black smoke”, while the smaller particulates are invisible to the eye and the most carcinogenic particles from the exhaust gas.

A standard method to reduce harmful emissions of soot particles is the use of Diesel particulate filters (DPF) installed in the exhaust stream. Soot removal from Diesel exhaust gas is a two-step technology. In the first step, the solid particles from the gas phase are filtered using the particulate filter. In the second step the filter is regenerated by oxidizing the accumulated solid particles. This need to periodically regenerate the filter is the main drawback of these systems. Moreover, oxidation of soot particles inside the filters is a challenging task as a high temperature ( $550^{\circ}\text{C}$  -  $600^{\circ}\text{C}$ ) is needed while the Diesel exhaust gas temperature lies between  $200^{\circ}\text{C}$  and  $400^{\circ}\text{C}$ . This could be overcome with an oxidation catalyst to promote soot oxidation. Moreover, during regeneration the exothermic reactions can lead to damage of the filter system.

The particulate filter consists of a honeycomb structure, commonly made from ceramic materials (e.g., cordierite), with alternate channels plugged at the opposite ends. The flow enters into the open end of a channel, and the plug at the opposite end forces the flow to pass through the porous wall, and go out through the neighboring channel. The solid particles are captured in the porous wall while the exhaust gas is allowed to go out in order to maintain low pressure drop. The filter is then regenerated to its original state burning the accumulated particulate matter. The soot decomposition is facilitated using a catalyst coated on the filter or added to the fuel. Fig. 1.3 shows a typical Diesel particulate filter with the flow passing through the filter.

Today, many Diesel particulate filter types are available and commercialized by various manufactures. However, to meet the upcoming regulations for mobile Diesel applications, higher efficiency of the particulate filter is required.

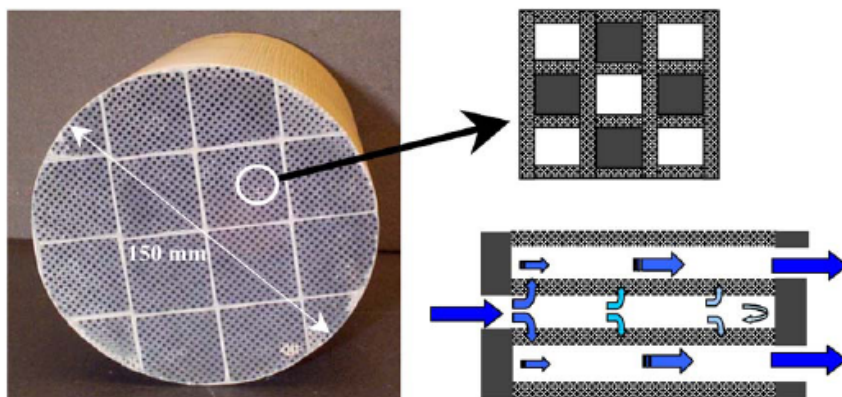


**Fig. 1.3:** Typical ceramic Diesel particulate filter with the flow path through the filter [16].

### b) Advanced Particulate Filter

An attractive alternative for simultaneous removal of  $\text{NO}_x$  and soot from the exhaust gas of Diesel engines are iron containing catalysts. Kureti *et al.* [17] showed that iron-containing oxide catalysts coated on a particulate filter can effectively remove  $\text{NO}_x$  and soot simultaneously. Moreover, this catalytic system is highly selective towards nitrogen conversion.

## 1.4 Multi-scale Modeling in Heterogeneous Catalysis

Heterogeneous catalysis in flow reactors is an outstanding example for multi-scale process in chemistry. Microscopic aspects of surface reactivity couple to macroscopic fluid flow in the gas phase, and length and time scales involved cover the range from macroscale to nanometers and from minutes to picoseconds, respectively. Fig. 1.4 shows different size scales of processes occurring in an automotive catalytic converter.

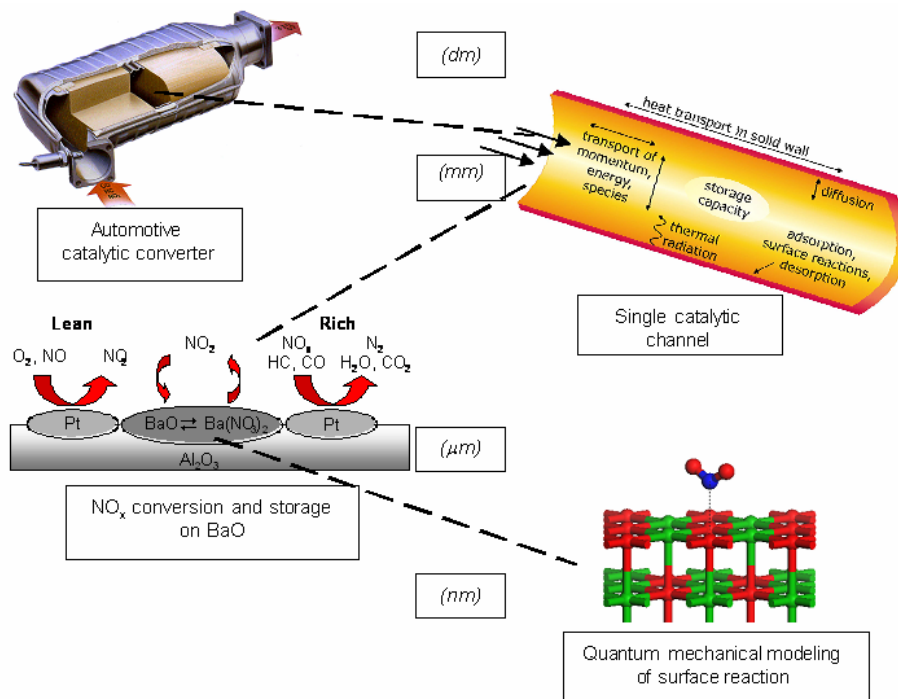


**Fig. 1.4:** Different size scales of processes occurring in an automotive catalytic converter. The catalytic converter image is a picture courtesy of J. Eberspächer GmbH & Co. The channel image was taken from Ref. [18].

The monoliths are multi-channelled ceramic structures on whose walls there is a coated high-surface-area porous layer (washcoat) with finely-dispersed catalytic particles. The exhaust gas molecules flow through the channels and diffuse through the pores of the washcoat to adsorb on the catalytically active surfaces. On the active surfaces the molecules can decompose, diffuse until they react with another molecule, or desorb. The product molecules undergo the reverse pathway to the final exhaust gas stream. The length scales of these processes cover a range from decimeters (the catalytic converter) to nanometers (the catalytic surface site) and the time scales span from minutes (entire catalytic converter thermal behaviour) to picoseconds (the surface reactions).

At macroscopic scale, understanding of the catalytic converters can be obtained from engineering approaches using reactor setups under real working conditions. At this scale concentrations profiles, overall reaction rates, and overall transport properties can be measured experimentally. The computer modeling approaches used are continuum methods such as fluid dynamics calculations, studying transport phenomena.

Downscaling one step to the meso-scale (length scale between  $10^{-3}$  to  $10^{-6}$  meters on a time scale of milliseconds to microseconds) understanding of the catalyst-reactive walls porous structure can be obtained. At this level, phenomena such as transport and reaction of species in the pores of the washcoat are investigated. The theoretical methods employed are molecular dynamics and Monte-Carlo simulation methods.

At microscopic scale, understanding of the surface reactivity and structure at atomic level (nanometers and picoseconds scales) is considered. At this level, the theoretical approaches employ semi-empirical and *ab-initio* methods. Quantum mechanical modeling is of prime importance in providing a detailed insight into elementary-step surface reactions, giving information on electronic structures (surface geometries), energetics (adsorption energies, activations energies of surface reactions) and reaction pathways of the system.

Given the large range of size and time scales of the catalytic processes, multi-scale modeling combined with experimental results should be considered for the development and improvement of the catalytic systems. The obtained higher-scale information (often experimental) can be used to build parameters for lower-scale methods, and the obtained detailed knowledge from a lower-scale can be applied to a macroscopic level to improve prediction of the entire catalytic converter performance.

## 1.5 Scope and Content of this Thesis

The aim of this thesis was to develop elementary steps of the surface reactions in automotive storage catalytic converters and to determine kinetic parameters for them. The obtained detailed knowledge was further used in kinetic simulations of a catalytic converter under real working conditions to understand the NO<sub>x</sub> storage and reduction catalytic behavior. The work can be divided in two parts: i) microscopic level understanding of elementary step surface reactions by means of quantum mechanical calculations and ii) macroscopic level understanding of the entire catalytic converter by means of numerical simulations.

In Chapter 2, the quantum mechanics background and the *density functional theory* (DFT) method used for the electronic structure calculations performed in this work are described.

Prior to all calculations performed in this thesis a comparative study was carried out (Chapter 3) to understand the sensitivity of calculation results on DFT parameters.

Chapter 4 presents quantum-chemical studies of the adsorption on BaO(100) surface of four gas-phase species relevant for exhaust-gas catalysis. Adsorption geometry and adsorption energy of NO, NO<sub>2</sub>, CO<sub>2</sub> and H<sub>2</sub>O in dependence on adsorption site and surface coverage were calculated. The BaO(100) was chosen as a model surface for NO<sub>x</sub> storage process as it has been shown that BaO is indeed a material with storage capacity [19].

In Chapter 5, DFT calculations were performed to determine thermodynamic and kinetic parameters of reactions of oxygen on a Pt(111) surface and their dependence on surface coverage. Precious metals play an essential role in exhaust-gas catalysis as the oxidation and reduction reactions occur at noble metal centers. Three processes were investigated: (1) adsorption of molecular oxygen, (2) the dissociation into atomic oxygen, and (3) the surface diffusion of atomic oxygen.

The information obtained in Chapters 4 and 5 was furthermore used in Chapter 6 for a detailed understanding of a catalytic converter under real working conditions. Numerical simulations of the competitive adsorption/desorption equilibrium of the four species, investigated in Chapter 4, were performed. The results of oxygen reactions on Pt (Chapter 5) were used in a kinetic model of oxygen surface reactions.

In Chapter 7 the results are summarized and general conclusions are given.



## Chapter 2: Quantum Mechanics

Quantum mechanics [20] is a mathematical description of theoretical chemistry describing matter at microscopic level. Quantum theory goes back to the beginning of the 20<sup>th</sup> century, when experimental evidence showed that the behavior of atomic and subatomic particles could not be explained by the laws of classical mechanics introduced in the 17<sup>th</sup> century by Isaac Newton. However, it has been shown that classical mechanics fails only when it is applied to very small particles (atoms, nuclei, and electrons) and to very small transfers of energy. In particular, the observations applied to black-body radiation, heat capacities, the photoelectric effect, the atomic and molecular spectra showed that systems can exchange energy only in discrete values. The quantization of energy was proposed in 1900 by the German physicist Max Planck proving that the energy of an electromagnetic oscillator of frequency  $\nu$  is limited to an integral multiple of the quantity  $h\nu$  ( $E = n \cdot h\nu$ , where  $n = 0, 1, 2, \dots$  and  $h = 6.626 \times 10^{-34}$  J·s is Planck's constant) and can not be varied arbitrarily. The most convincing evidence for the quantization of energy came from the observation of spectroscopic lines. From a typical atomic and molecular spectrum it was observed that the radiation is absorbed or emitted at a series of discrete frequencies.

The experimental evidence (the photoelectric effect, diffraction) proved also the dualism of matter and light. It has been shown that light behaves like a wave as well as a particle, and microscopic particles behave also wave-like. The concept, called the “wave-particle dualism”, could be explained by quantum theory and was introduced by Louis de Broglie in 1924. Electrons (particles) were found do give diffraction patterns (typical characteristic of waves) when passed through a double slit in a similar way to light waves, and radiation was found (the photoelectric effect) to behave as particles (metals ejected electrons upon exposure to ultraviolet radiation).

In 1926 the concepts of quantum mechanics and equations for describing them were developed.

## 2.1 The Schrödinger Equation

The Schrödinger equation extends Louis de Broglie's concept (1924) of atomic particles described in terms of waves. De Broglie's postulate states that the motion of a microscopic particle (electron, proton, atom, etc) behaves also wave-like. Therefore, it was considered that a wave equation explains the behavior of atomic particles.

A wave equation (the Schrödinger equation) was proposed by the Austrian physicist Erwin Schrödinger in 1926. For a system of electrons and nuclei the time-independent (stationary) many-body Schrödinger equation is generally written as

$$\hat{H}\Psi = E\Psi \quad , \quad (2.1)$$

where  $\hat{H}$  is the total energy operator (Hamiltonian operator)<sup>§</sup>,  $\Psi$  is the wave function, and  $E$  is the total energy of the system. The Hamiltonian operator is the sum of the kinetic energy operator  $\hat{T}$  (the kinetic energy of the electrons and nuclei respectively) and the potential energy operator  $\hat{V}$  (the attractive electrostatic interaction between the nuclei and electrons, the repulsive potential due to electron-electron and nucleus-nucleus interactions):

$$\hat{H}\Psi(r) = -\frac{\hbar^2}{2m}\nabla^2\Psi(r) + \hat{V}(r)\Psi(r) = E\Psi(r) \quad . \quad (2.2)$$

For the evolution of a system with time, the time-dependent Schrödinger equation is solved:

$$\hat{H}\Psi = i\hbar\frac{\partial}{\partial t}\Psi \quad . \quad (2.3)$$

$$i\hbar\frac{\partial}{\partial t}\Psi(r,t) = -\frac{\hbar^2}{2m}\nabla^2\Psi(r,t) + \hat{V}(r,t)\Psi(r,t) \quad (2.4)$$

The wave function is a measure for the probability of finding the particle at a certain position. The probability density of a particle is the square of the amplitude of the wave function,  $|\Psi|^2$ .

---

<sup>§</sup> Operators are typed with a hat (^) throughout this thesis.



Solving the Schrödinger equation, the allowed energy levels of quantum mechanical systems (such as atoms) can be determined. The eigenvalues of the energy operator  $\hat{H}$  represent the allowed energy levels of the system.

The Schrödinger equation has an analytical solution only for very small systems (e.g., for the hydrogen atom). The position of each electron in the system relative to the nucleus is described by three coordinates; thus the wave function depends on three coordinates of each electron in the atom. For larger systems (polyatomic molecules) approximations have been introduced in order to find the wave function of the system.

## 2.2 The Born-Oppenheimer Approximation

A fundamental approximation used for solving many-body Schrödinger's equation was proposed by Born and Oppenheimer in 1927. The Born-Oppenheimer approximation separates between the nuclei and electrons' motion [21]. It assumes that, since nuclei are much heavier than electrons, they move much more slowly and can be considered fixed. Thus, the wave function of the electrons solely depends on the actual position of the nuclei. Within this approximation, as the nuclei are fixed, their kinetic energy is zero and the potential energy due to nucleus-nucleus repulsion is a constant. Thus, the Hamiltonian operator becomes a sum of the kinetic energy of the electrons ( $\hat{T}$ ), the potential energy due to electron-electron interaction ( $\hat{V}_{ee}$ ), and the attractive potential energy between the electrons and nuclei, known as the external potential ( $\hat{V}_{ext}$ ),

$$\hat{H}_{elec} = \hat{T} + \hat{V}_{ee} + \hat{V}_{ext} . \quad (2.5)$$

Employing this approximation the nuclear and electronic wave functions are decoupled, and the Schrödinger equation is solved only for the electronic wave function:

$$\hat{H}_{elec} \Psi_{elec} = E_{elec} \Psi_{elec} . \quad (2.6)$$

### 2.3 The Density Functional Theory (DFT)

Another approach used in first-principles<sup>h</sup> studies for solving Schrödinger's equation relies on *Density Functional Theory* (DFT) [22]. This method is a powerful *ab-initio* tool of quantum chemistry used for determining geometrical structures and for calculating the total energy of a system. DFT is a widely-used method as it is computationally more efficient than other quantum-chemical methods (e.g., Hartree-Fock method) with similar accuracy. The greatest contribution to *density functional theory* dates from 1964 and was developed by Hohenberg and Kohn [23]. The *density functional theory* is a ground-state theory and is based on two theorems.

The first theorem states that the total energy of a system of electrons and nuclei is a unique functional<sup>i</sup> of the electron density. The total energy is written as

$$E[\rho(r)] = T[\rho(r)] + V[\rho(r)] + E_{xc}[\rho(r)] , \quad (2.7)$$

where  $T[\rho(r)]$  is the kinetic energy of a system of non-interacting particles of density  $\rho(r)$ ,  $V[\rho(r)]$  is the classical electrostatic energy due to Coulombic interactions, and  $E_{xc}[\rho(r)]$  represents the exchange and correlation energies.

According to this theorem all ground-state properties (the potential, the wave function, the Hamiltonian) are functionals of the charge density  $\rho(r)$ . The total energy is written in terms of the electron density as

$$E = E[\rho(r)] , \quad (2.8)$$

and the density is written in terms of the wave function of the non-interacting electrons as

$$\rho(r) = \int \Psi(r) dr . \quad (2.9)$$

---

<sup>h</sup> First-principles (synonymous to *ab-initio*) calculations involve no adjustable parameters.

<sup>i</sup> A functional is a function whose argument is itself a function.

The second Hohenberg-Kohn theorem states that the ground-state electron density can be calculated exactly using the variational method<sup>j</sup>. This principle is applied to determine the electron density from which the total energy of the ground state is calculated. The variational principle states that a trial value of a quantity is greater than (or equal to) its lowest possible value, e.g.,

$$E[\rho'] \geq E_0[\rho_0], \quad (2.10)$$

where  $\rho_0$  and  $\rho'$  are the ground-state energy and any trial density satisfying the boundary conditions  $\rho'(r) \geq 0$ ,  $\int \rho(r) dr = N$ , with the corresponding ground state energy  $E_0$  and any trial energy  $E$  respectively.  $N$  denotes the number of electrons in the system.

### 2.3.1 Kohn-Sham Equation

A more ingenious approach for applying density functional, awarded with the Nobel prize, was proposed in 1965 by Kohn and Sham [24]. They introduced the concept of non-interacting particles which results in a set of one-electron Schrödinger-like equations moving in an effective potential

$$\hat{H}\psi_n = \left( -\frac{\hbar^2}{2m} \nabla^2 + V_{\text{eff}} \right) \psi_n = E \psi_n. \quad (2.11)$$

Here,  $\psi_n$  are the  $n$  one-electron wave functions, and  $V_{\text{eff}}$  is the effective potential which includes the ionic potential, the electron-electron Coulomb interaction and the exchange-correlation potential.

---

<sup>j</sup> For further details on this principle the book by Parr and Yang is recommended [22].

The total energy is written as

$$E[\rho(r)] = \int V_{\text{ext}}(r)\rho(r)\mathrm{d}r + F[\rho(r)] = V_{\text{ext}}[\rho(r)] + F[\rho(r)] , \quad (2.12)$$

where  $V_{\text{ext}}$  is the external potential of the nuclei and  $F$  is the functional of the total energy .

The electron density is obtained as a sum of the one-wave functions of the non-interacting electrons:

$$\rho(r) = \sum_i |\psi_i(r)|^2 , \quad (2.13)$$

where,  $\psi_i(r)$  are the so-called Kohn-Sham orbitals.

The total energy functional  $F$  in the Kohn-Sham method is separated into the following contributions:

$$F[\rho(r)] = T[\rho(r)] + V_{\text{ee}}[\rho(r)] + E_{\text{xc}}[\rho(r)] , \quad (2.14)$$

where  $T[\rho]$  is the kinetic energy of the non-interacting electrons,  $V_{\text{ee}}$  is the electron-electron interaction and  $E_{\text{xc}}$  is the so-called exchange-correlation energy which includes everything that was not included in the previous terms, such as electron exchange, electron correlation, the correction needed for the kinetic energy and the correction for self-interaction.

The explicit form of the exchange-correlation energy functional is unknown and has to be approximated. However, the contribution of this term is small compared to the other terms included in Equation (12). The approximations used for estimating the exchange-correlation energy are given in the subsequent section.

### 2.3.2 The Exchange-Correlation Functional

Several approximations for estimating the exchange-correlation energy have been developed. The simplest approach is the so-called local-density approximation (LDA) [24] which

considers the electron density as for a uniform electron gas. The LDA functional form is described by the equation:

$$E_{xc}[\rho(r)] = \int \varepsilon_{xc}[\rho(r)]\rho(r)dr , \quad (2.15)$$

where,  $\varepsilon_{xc}[\rho(r)]$  is the exchange-correlation energy and  $\rho(r)$  is the electron density. In this functional the exchange-correlation energy at a certain point depends only on the density at that point independent of other points. Despite this simple approach, local density approximation gives good results for bulk materials. However, LDA is inadequate for molecular systems as the charge density is non-uniform around atoms and the exchange-correlation energy is influenced by the gradient of the electron density.

A better approximation which includes the gradient of the electron density is the generalized gradient approximation (GGA) [25] in the form

$$E_{xc}[\rho(r)] = \int f[\rho(r), \nabla\rho(r)]\rho(r)dr . \quad (2.16)$$

Within the generalized gradient approximation there are used several functionals (named after their authors): PW91 – proposed by Perdew and Wang [26], PBE – proposed by Perdew *et al.* [27], and RPBE – a revised form of the PBE functional proposed by Hammer *et al.* [28]. The former functional gives an accurate description of chemical surface processes and, therefore, in the present work the generalized gradient approximation (GGA) as proposed by Perdew and Wang (PW91) has been applied. The PBE functional is recommended for bulk calculations and molecules interacting with metallic surfaces.

## 2.4 DFT Implementation in the CASTEP Code

In this thesis plane-wave pseudo-potential calculations have been performed using the CASTEP (Cambridge Sequential Total Energy Package) [29] program. CASTEP is a commercially available code for *ab-initio* quantum mechanical calculations based on density-functional theory. Calculations are performed on 3D periodically repeating unit cells,

usually referred to as „supercells“. This approach makes it particularly suitable for bulk structures and surfaces and therefore for the investigations performed in this work. The electronic wave functions are expanded in terms of plane waves, and the core electrons are represented by an effective potential (pseudo-potential). The exchange-correlation contribution to the total energy is implemented through the use of local density approximation (LDA) or general gradient approximation (GGA). A self-consistent field method is applied for electron density variation to find the ground state energy. In order to understand electronic effects between the surface and the adsorbed molecules, Mulliken charge transfer was calculated according to a formalism described by Segall *et al.* [30]. A short description of CASTEP's implementations is given in the subsequent paragraphs.

#### 2.4.1 “Supercell” Approach

Structures optimization as implemented in CASTEP are performed on one unit cell periodically repeated in 3D. Surfaces are represented as slabs extending in three dimensions. In this case, the lateral sizes of the supercell as well as the distance between the slabs (vacuum thickness = the distance between the first layer of one slab and the last layer of the next periodic cell) have to be large enough to avoid adsorbate interaction with the next periodic image (lateral interactions) or with the subsequent slab, respectively. The slab must also be thick enough to represent both bulk and surface atoms. For illustration of a supercell, Fig. 2.1 shows one unit cell repeated in vertical direction. In the present work various lateral sizes of the supercell were chosen. The distance between the slabs was set to 1000 pm and considered to be enough as tests performed for vacuum thicknesses between 800 and 1500 pm showed variations in adsorption energies of less than 0.1 eV (cf. Chapter 3).

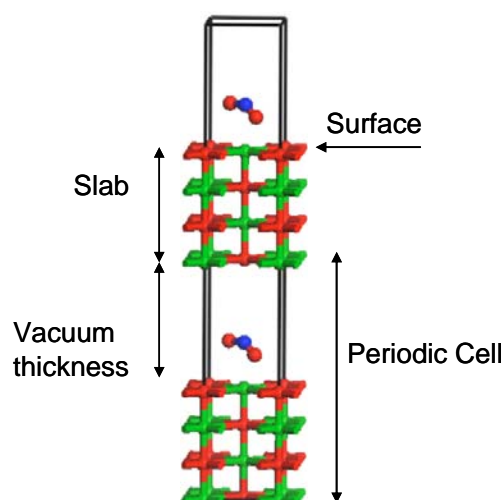


**Fig. 2.1:** Periodic unit cell with a slab consisting of four atomic layers, repeated in vertical direction.

The geometry optimization process allows to find the most stable structure corresponding to the energy minimum. CASTEP performs geometry optimization using an iterative process. The atomic coordinates and the cell parameters are modified until a defined convergence tolerance of the calculated stresses and forces is reached.

Adsorption energies ( $E_{\text{ads}}$ ) are calculated as the difference between the total energy of the surface slab with adsorbate after geometry optimization and the total energy sum of the surface slab alone and the gas-phase molecule after geometry optimization. The adsorption energies are calculated according to

$$E_{\text{ads}} = E_{(\text{slab} + \text{adsorbate})} - (E_{\text{slab}} + E_{\text{adsorbate}}) . \quad (2.17)$$

To determine activation energies, the potential energy surface (PES) of a reaction is calculated by performing a linear synchronous transit (LST) method combined with a quadratic synchronous transit (QST) calculation and conjugate gradient refinements [31] as implemented in CASTEP. The LST/QST method is an interpolation method. The transition state energy is obtained iteratively as the minimum of maxima on the potential energy surface interpolated linearly between the energies of the optimized geometries of reactants and products. The algorithm starts with the LST method. An energy maximum (Fig. 2.2, green point) on the potential energy surface is found to which a conjugate gradient (QST/CG) minimization (red point) is applied until the convergence is reached. The transition state

represents the highest point along the lowest energy pathway between the reactants and products. Fig. 2.2 shows a schematic drawing of the transition states search using the LST/QST method.

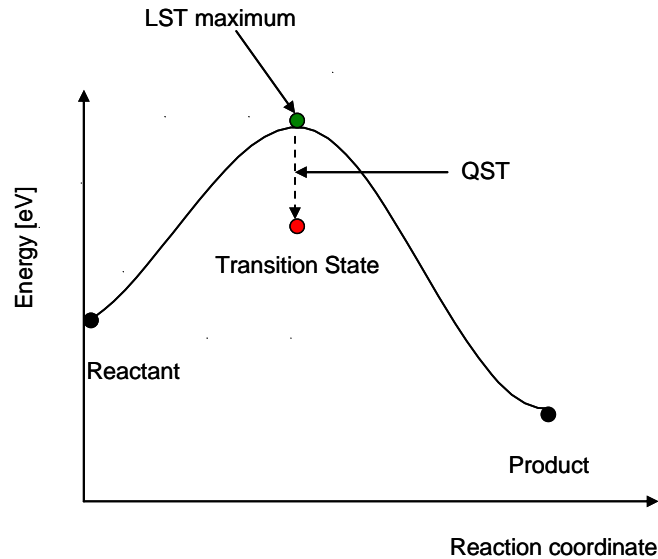


**Fig. 2.2:** Transition state search based on the LST/QST method.

The activation energy is calculated according to

$$E_{\text{act}} = E_{\text{transition state}} - E_{\text{reactant}} . \quad (2.18)$$

The reaction energy is calculated as the difference between the product energy and reactant energy

$$\Delta E_{\text{reaction}} = E_{\text{product}} - E_{\text{reactant}} . \quad (2.19)$$

#### 2.4.2 The Plane-Wave Basis Set

The plane-wave method is applied to 3D periodic systems and is based on Bloch's theorem [32,33]. According to this theorem, due to the translational symmetry, each



electronic wave function can be expressed as a product of a cell periodic part  $u_i(r)$  and a plane wave part  $e^{ik \cdot r}$  with the wave vector  $k$ ,

$$\Psi_i(r) = u_i(r)e^{ik \cdot r} . \quad (2.20)$$

The cell periodic part  $u_i(r)$  is expanded using a basis set of plane waves with reciprocal lattice vectors  $G$ :

$$u_i(r) = \sum_G c_{i,G} e^{iG \cdot r} , \quad (2.21)$$

where,  $c_{i,G}$  represent the expansion coefficients. The electronic wave function becomes a sum of plane waves:

$$\Psi_i(r) = \sum_G c_{i,k+G} e^{i(k+G) \cdot r} . \quad (2.22)$$

Here, the exponential term is a plane wave of wave vector  $k$ .

Bloch's theorem simplifies the problem of calculating a large number of plane waves for an infinite number of  $k$ -points<sup>k</sup> to a reduced number of plane waves for an infinite number of  $k$ -points over the reciprocal lattice vectors. This simplification known as  $k$ -point mesh (or  $k$ -point sampling) is achieved by considering that the change in the wave function with  $k$  becomes negligible for  $k$ -points that are close to each other, and therefore a finite set of plane waves is calculated.

The electronic wave function at each  $k$ -point is expressed in terms of a discrete plane wave basis set. The plane wave basis set is truncated such as to include plane waves with coefficients that have kinetic energy smaller than a particular cut-off energy,

---

<sup>k</sup>  $k$ -points is a set of points in the Brillouin-zone. The Brillouin-zone is a primitive unit cell in the reciprocal lattice. For more details the book by Ashcroft *et al.* [32] is recommended.

$$E_{\text{cut-off}} = \frac{\hbar^2(G + k)^2}{2m} \quad (2.23)$$

However, the plane wave's coefficients with a smaller kinetic energy have a more important role than those with a very high kinetic energy. In the calculations performed in this work, the plane wave basis set was truncated at a kinetic energy of 300 eV for BaO investigations and 400 eV for the Pt results.

### 2.4.3 Pseudo-Wave Function and Pseudo-Potential Approximation

The pseudo-potential approximation distinguishes between the valence electrons and core electrons, and replaces the ionic potential of the nucleus and the core electrons with an effective potential (pseudo-potential). This approximation reduces the number of calculated plane waves as only the valence electrons are treated in the calculation while for the core electrons a pseudo-wave function is approximated. Fig. 2.3 illustrates this implementation.

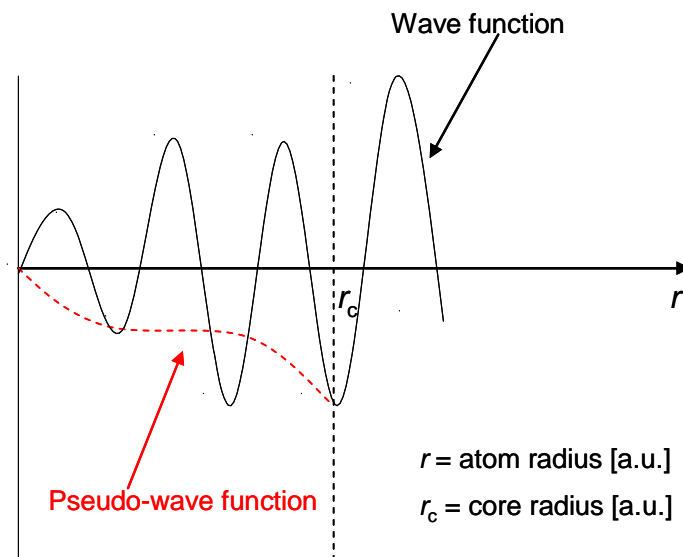


**Fig. 2.3:** The pseudo-potential approximation

In CASTEP two forms of the pseudo-potential are implemented: the ultra-soft pseudo-potential and the norm-conserving pseudo-potential. The ultra-soft pseudo-potential calculations are performed at a low  $E_{\text{cut-off}}$  while for the norm-conserving pseudo-potential implementation a larger cut-off energy is applied which makes it computationally more expensive. Therefore, in all calculations performed in this thesis an ultra-soft pseudo-potential as proposed by Vanderbilt [34] was employed.

#### 2.4.4 Brillouin-Zone Sampling

Another implementation used together with the plane wave approach is the  $k$ -point mesh in the reciprocal space<sup>1</sup>. Applying Bloch's theorem in a periodic system, the infinitely extended integrals in real space over the system are replaced by the finite integrals over the Brillouin zone in reciprocal space. For minimization of the number of  $k$ -points needed to integrate the Brillouin zone, different methods have been developed [35-37]. In CASTEP the method proposed by Monkhorst and Pack is implemented [36].

The Monkhorst-Pack scheme produces a homogeneous grid of  $k$ -points in the three dimensions of the reciprocal space. The number of  $k$ -points is determined by three integers,  $q_i$  along the coordinates. The integers generate a sequence of numbers according to

$$u_i = \frac{2r - q_i - 1}{2q_i}, \quad (2.24)$$

where  $r$  varies from 1 to  $q_i$ . The grid size determined by the Monkhorst-Pack scheme is obtained according to

$$k_{xyz} = u_x t_1 + u_y t_2 + u_z t_3, \quad (2.25)$$

---

<sup>1</sup> The reciprocal-space lattice is a set of all vectors  $K$  satisfying  $e^{iK \cdot R} = 1$  for all  $R$  in the Bravais lattice. The reciprocal-space lattice is itself a Bravais lattice. For more details the book by Ashcroft *et al.* [32] is recommended.

where  $t_1$ ,  $t_2$  and  $t_3$  are the lattice vectors in reciprocal space.

In all calculations performed in this work, the  $k$ -points spacing was set to  $5 \text{ pm}^{-1}$  within the Brillouin zone as generated by the Monkhorst-Pack scheme [36].

### 2.4.5 Mulliken Charge Analysis

Mulliken charge analysis [38] is one of the most common methods of population analysis for assigning partial charges of individual atoms in a molecule. The method is able to calculate the net electron transferred from the surface to the adsorbant upon adsorption or to the transition state of a surface reaction.

The distribution of electrons in a molecule and the properties related to the charge distribution can provide enormous help in interpreting the chemical surface processes. For example in case of a surface covered with different adsorbants, all adsorbants will compete for the charge density offered by the surface, and the net electron transferred will vary depending on the coverage as well as on the chemical nature of the adsorbants.

Various schemes to partitioning the total electron density onto charges of individual atoms have been developed. In CASTEP the Mulliken charges are calculated according to a formalism described by Segall *et al.* [30].

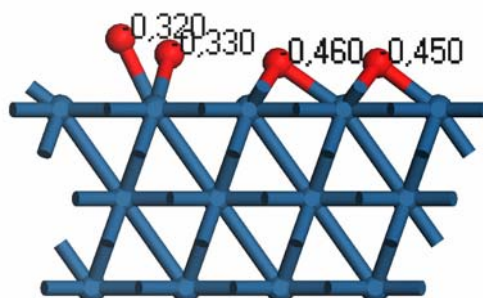


**Fig. 2.4:** Mulliken partial charges in the transition state of oxygen decomposition on Pt(111).

## 2.5 Calculation of Magnetic Moment

The electron possesses an intrinsic angular momentum, called the electron spin, and is characterized by its mass  $m_0$ , its charge  $q = -e$ , its orbital angular momentum  $l$  and its spin quantum number  $s$  which is connected with a magnetic moment  $\mu_s$  that can interact with magnetic fields.

The spin can exhibit two different orientations: clockwise or counterclockwise, which can take the values  $+1/2$  and  $-1/2$  denoted as  $\alpha$  or  $\uparrow$  and  $\beta$  or  $\downarrow$ . According to Pauli's exclusion principle, electrons occupying the same state (the same orbital) have to have different spins. Therefore, the overall spin of a fully occupied molecular orbital is zero, since the two orientations cancel each other. For molecules with unpaired electrons such as radicals or odd-electron molecules, the unpaired spin may be either  $\uparrow$  or  $\downarrow$ , and the overall spin differs from zero.

In order to calculate the magnetic moment in terms of spin density, charge densities for both electronic orientations ( $\rho_\alpha(r)$ ,  $\rho_\beta(r)$ ) are calculated using a spin-unrestricted version of the GGA functional (GGSA). From these charge densities for different electron polarizations, the spin density is calculated according to

$$\rho_{spin}(r) = \rho_\alpha(r) - \rho_\beta(r) . \quad (2.26)$$

The total electron density of the supercell is calculated according to

$$\rho_{spin}^{total} = \int \rho_{spin}(r) dr . \quad (2.27)$$

Furthermore, the local electron density is calculated according to

$$\rho_{spin}^{local} = \int |\rho_{spin}(r)| dr . \quad (2.28)$$

The local electron spin density is a measure of the spin polarization inside a certain system. To assume that a system is non-spin-polarized, both the local and the total spin densities have to be zero. A detailed description of spin influence on the calculations performed in this thesis is given in Chapter 3.



## **Chapter 3: Sensitivity of Calculations Results on DFT Parameters**

Density-functional theory (DFT) *ab-initio* calculations are becoming a useful tool for calculating thermodynamic and kinetic parameters for detailed surface reaction mechanisms. Its absolute accuracy for adsorption and activation energies, based on state-of-the-art functionals, is estimated to be in the order of tenths of an electron volt [27,39,40]. It can successfully predict trends and relative stabilities. Its versatility in the choice of substrate (oxidic, metallic) and adsorbate (atomic, molecular) makes it particularly valuable when information is not easily accessible with conventional experimental techniques (e.g., surface diffusion coefficients, coverage-dependence of thermodynamic parameters [41]).

In the present work, DFT calculations were performed using the Cambridge Sequential Total Energy Package (CASTEP) [29]. A short description of the program was given in Chapter 2. Prior to all calculations performed in this work, a comparative study was carried out in order to understand the sensitivity of calculations on DFT parameters. The obtained results are presented in the following subchapters.

### **3.1 Energy Dependence on Vacuum Thickness**

Vacuum thickness represents the distance between the first layer of a slab and the last layer of the next periodic unit cell (for illustration see Fig. 2.1). This parameter has to be large enough to ensure that the adsorbate does not interact with the subsequent slab. To understand the total energy dependence on the vacuum thickness, tests have been performed for a  $(1 \times 1)$  supercell of a BaO(100) surface varying the vacuum thickness from 700 pm to 1500 pm. The BaO(100) surface was built cleaving a four-layer slab from the bulk structure. As adsorbate a symmetric NO<sub>2</sub> molecule above the surface was considered. The

total energy dependence on the vacuum thickness is represented in Figure 3.1. Calculated  $\text{NO}_2$  absolute energies showed negligible variations (less than 0.1 eV) for vacuum thicknesses between 800 pm and 1500 pm. Therefore in all calculations performed in this work the distance between the slabs was set to 1000 pm.

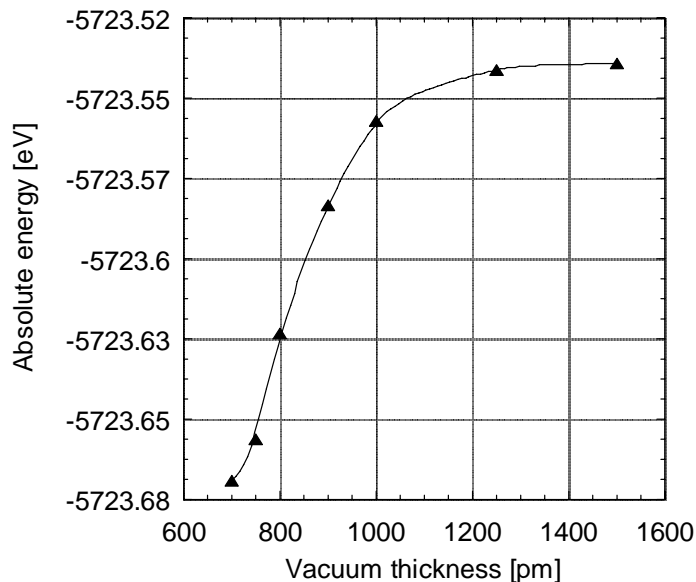


**Fig. 3.1:** Energy dependence on vacuum thickness for an  $\text{NO}_2$  molecule adsorbed on a four-layer BaO slab.

### 3.2 Energy Dependence on $k$ -point Spacing

$k$ -point spacing represents the number of integration points to integrate the wave function in reciprocal space and thus defines the accuracy of the Brillouin zone sampling. The method used for generating and minimizing the  $k$ -point mesh was described in Chapter 2. In the present subchapter the influence of  $k$ -point precision on adsorption energies was determined.

In CASTEP different qualities of the  $k$ -point precision are implemented corresponding to a  $k$ -point separation of  $4 \text{ pm}^{-1}$ ,  $5 \text{ pm}^{-1}$ ,  $7 \text{ pm}^{-1}$ , and a single point calculation respectively. The  $k$ -point grid can be also specified using custom grid parameters. For the  $4 \text{ pm}^{-1}$ ,  $5 \text{ pm}^{-1}$ ,  $7 \text{ pm}^{-1}$ , and a single point calculation, adsorption energies of a symmetric  $\text{NO}_2$  molecule adsorbed on a BaO(100) surface were calculated. The adsorption energy dependence on



$k$ -point spacing is shown in Fig. 3.2.

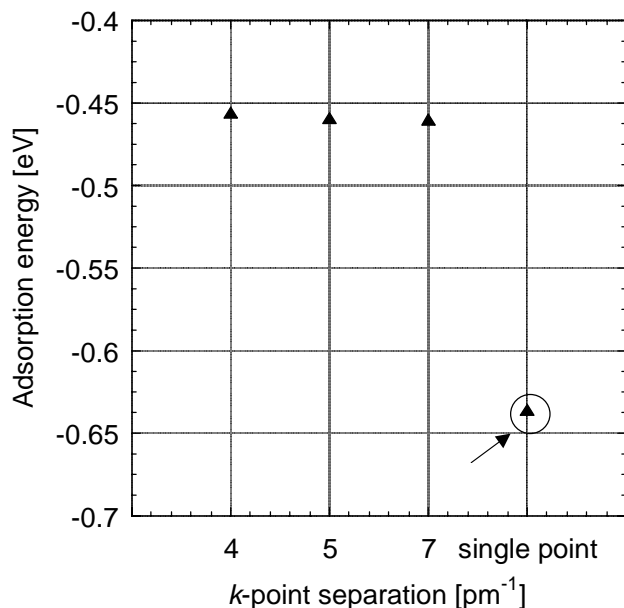


**Fig. 3.2:** Adsorption energy dependence on  $k$ -point precision for an  $\text{NO}_2$  molecule adsorbed on  $\text{BaO}(100)$  surface. The marked case corresponds to a single-point calculation.

The obtained results showed a difference of 0.01 eV in adsorption energies for the  $4 \text{ pm}^{-1}$ ,  $5 \text{ pm}^{-1}$ ,  $7 \text{ pm}^{-1}$   $k$ -point precision. Therefore it was concluded that a spacing of  $5 \text{ pm}^{-1}$  within the Brillouin zone was sufficient. The single-point calculation (the marked case in Fig. 3.2) is the least representative sampling of the Brillouin zone as it corresponds to the origin of the reciprocal space and gives less accurate results.

### 3.3 Energy Dependence on Cut-off Energy

The kinetic cut-off energy is one of the parameters associated with the electronic Hamiltonian and represents the precision of the plane wave basis set. It is one of the most important parameters that determine the accuracy (and the computational cost) of the calculated properties.

Convergence tests were carried out for adsorption energies of a NO<sub>2</sub> molecule adsorbed on BaO(100) surface. The adsorption energies were calculated for two values of the cut-off energy, 300 eV and 340 eV.

The results showed a difference of only 0.01 eV in adsorption energies and no further improvements of the convergence; therefore in this work a cut-off energy of 300 eV was used. This small difference in adsorption energies does not require to perform the calculations with a higher cut-off energy given that the calculation costs are double in memory and time.

For the second system investigated in this work, O<sub>2</sub>/Pt(111), a cut-off energy for the plane wave expansion of 400 eV was selected, assuring a very good convergence of the energy.

### 3.4 Surface Structural Relaxation

Surface structural relaxation<sup>m</sup> is an important parameter which has to be taken into account in order to understand the correct surface structure. In this thesis electronic structure calculations were performed for adsorption of different molecules on two surfaces relevant in automotive exhaust gas purification particularly for storage catalytic converters, Pt(111) and BaO(100) surfaces. The notation (111) and (100) represent the Miller indices of lattice planes in the crystalline structure. They are used for orientation and are determined by the planes intersection with the crystal axes<sup>n</sup>. Note that a 0 indicates that a plane is parallel to the corresponding axis, e.g., the (100) plane is parallel both to the *y* and *z* axes, and hence to the *yz* plane. Figure 3.3 shows the (111) and (100) lattice planes.

---

<sup>m</sup> The surface relaxation refers to a small displacement of a layer of atoms. It involves adjustments in the layer spacing perpendicular to the surface.

<sup>n</sup> For further details the book by Ashcroft *et al.* is recommended [32]

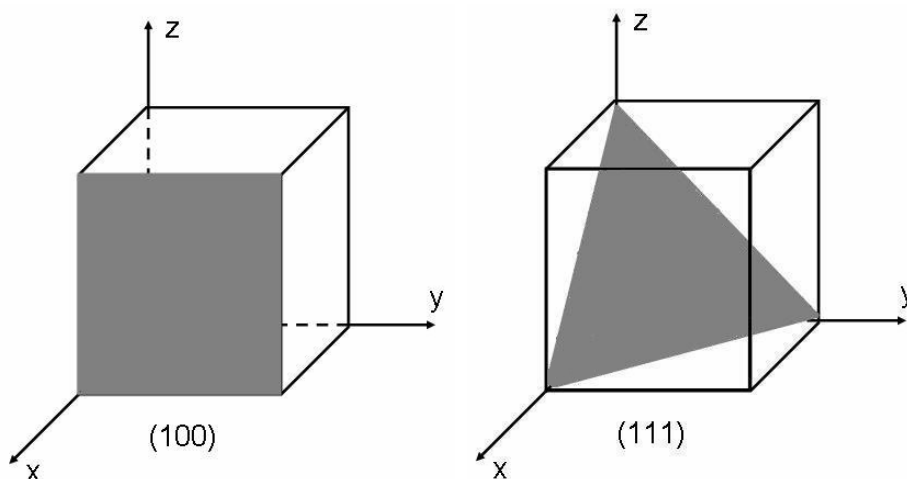


**Fig. 3.3:** Lattice planes and their Miller indices in a cubic unit cell.

The Pt(111) surface was modeled as a slab consisting of three atomic layers (see Chapter 5), extending by symmetry to an infinite surface. Such a model with a three-layers slab thickness has been used previously in other theoretical calculations [42-44] for modeling Pt(111) and other transition metal surfaces [45]. In the present work surface relaxation of Pt(111) has not been considered, as dynamical LEED structural analysis of the Pt(111) performed by Materer *et al.* [46] found that the relaxation is less than 1%. Moreover, Eichler *et al.* [47] showed also that surface relaxation has only a small influence on energies as well as geometries of O<sub>2</sub> adsorbed on Pt (111).

In case of BaO(100), the surface was represented as a slab consisting of four atomic layers extending by symmetry to an infinite surface. The slab structure was obtained taking into account surface relaxation by the following procedure: Bulk BaO was geometry-optimized, and a five-layer slab in a (1×1) periodic supercell with a vacuum thickness of 1000 pm was cleaved. To understand the surface distortions, tests have been performed, where the first atomic layer, the upper two atomic layers and the upper three atomic layers were allowed to relax. Fig. 3.4 shows a (1×1) periodic supercell with five atomic layers. The red layers were constrained (fixed) to the optimized-bulk distance while the grey layers were allowed to geometry optimization.

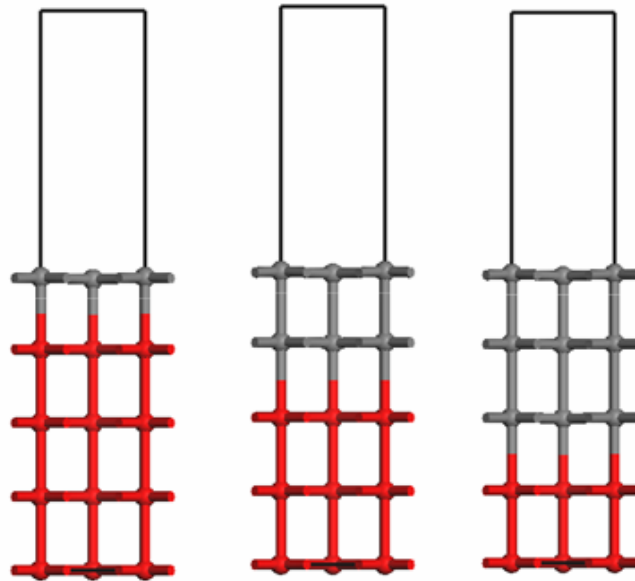


**Fig. 3.4:** A  $(1 \times 1)$  periodic supercell with a five-layers slab. The red layers were constrained (fixed) to the optimized bulk distance while the grey layers were allowed to geometry optimization.

The obtained interlayer spacing after relaxation of different numbers of layers (the first atomic layer, the upper two atomic layers and the upper three atomic layers) is shown in Fig. 3.5. The BaO surface contains two types of atoms; therefore, the surface distortions can be separated into an interlayer distance when the oxygen atom is terminating the surface, and the interlayer distance when the barium atom is terminating the surface. An average interlayer spacing is plotted in Fig. 3.5. Fig. 3.6 shows the interlayer spacing between the central atoms (with O as central atom in the top layer) between the upper two atomic layers, the upper three, the upper fourth, and all five atomic layers after consecutive relaxation.

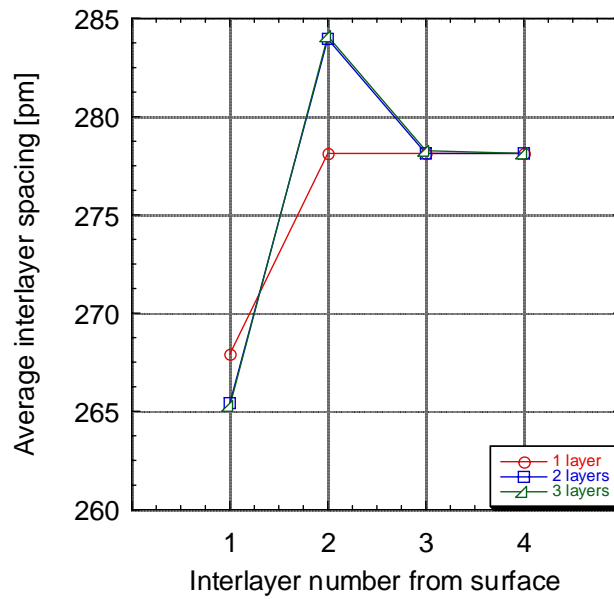


**Fig. 3.5:** The average interlayer spacing variation of the  $d(\text{Ba-O})$  and  $d(\text{O-Ba})$  distances between the layers of the unit cell.

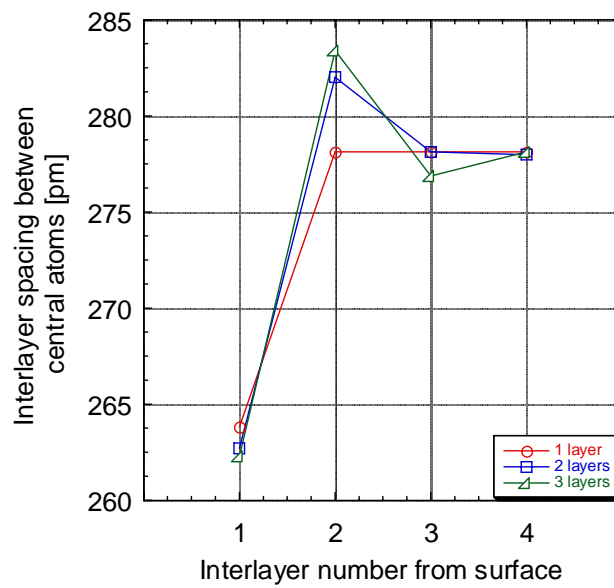


**Fig. 3.6:** The interlayer spacing of the central atoms between the layers of the unit cell.

After surface relaxation the interlayer spacing varied from the upper layers to the lower layers as follows: It decreased between the first and second layers, increased between the second and the third layer and decreased again between the third and fourth layers.

A considerable surface relaxation was obtained for the second case where the positions of the upper two atomic layers of the slab were geometry-optimized. The obtained values are given in Table 3.1. Allowing the upper three atomic layers of the slab to geometry-optimization, the results showed a very small difference of the interlayer spacing in comparison to the relaxation of the upper two atomic layers. In particular, differences of 0.2 pm, 0.15 pm and again 0.15 pm between the first and second layer, between the second and the third layer and between the third and the fourth layer were obtained.

	O <sub>surf</sub> site in top layer	Ba <sub>surf</sub> site in top layer
Top layer – 2 <sup>nd</sup> layer	262.7 pm	268.2 pm
2 <sup>nd</sup> layer – 3 <sup>rd</sup> layer	285.9 pm	282.0 pm
3 <sup>rd</sup> layer – 4 <sup>th</sup> layer	278.1 pm *	278.1 pm *
4 <sup>th</sup> layer – 5 <sup>th</sup> layer		

\* (= bulk distance)

**Table 3.1:** Surface relaxation after geometry-optimizing the first two atomic layers of a five-layer BaO slab in a (1×1) supercell.

The total energies of the optimized slabs with one, two, and three atomic layers allowed for relaxation are shown in Fig. 3.7. The results showed a difference of 0.01 eV between the energies of the optimized slab with relaxation of the upper two atomic layers ( $E = -5723.38$  eV) and the slab with relaxation of the upper three atomic layers ( $E = -5723.39$  eV).

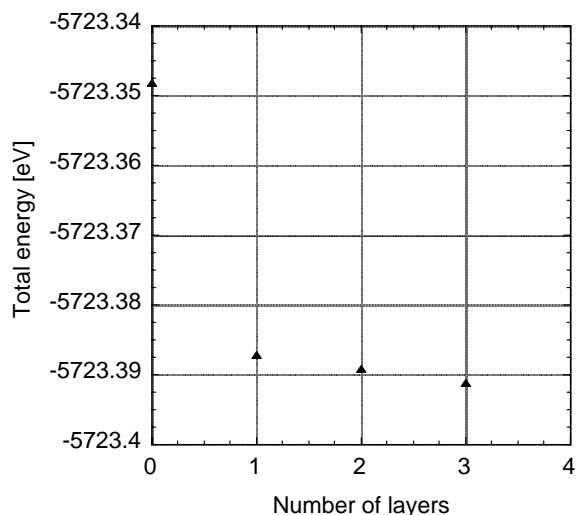


**Fig. 3.7:** The total energies of the optimized slabs with one, two, and three atomic layers relaxation.

Given these small differences of the interlayer spacing as well as of the total energy of the slab, it was concluded that a four-layer model is appropriate to understand the BaO(100) surface and to have the bulk well represented in the slab. This allows also keeping computation times below a reasonable limit as DFT calculations are numerically extremely demanding (see Subchapter 3.6).

The upper four atomic layers of the optimized slab as obtained after relaxation of the upper two atomic layers were used for all subsequent calculations of surface reactions with fixed atomic coordinates (frozen slab). However, to quantify the errors due to the use of a frozen slab, additional calculations on surface relaxation in the presence of adsorbates were performed. They are described together with the influence of spin effects on the calculations in the subsequent paragraph.

### 3.5 Influence of Spin Effect and Surface Relaxation on the Calculations

The calculations performed throughout this thesis rely on two simplifying assumptions, that are (1) the disregard of spin effects and (2) the use of a frozen slab for calculations with adsorbates. These assumptions were necessary to keep calculation times to a reasonable limit. In order to justify them, a set of calculations was performed for an NO<sub>2</sub> molecule (an odd

electron molecule) on a BaO surface using a (1×1) supercell where the assumptions were consecutively relaxed. The obtained geometrical parameters of the optimized structure, energetic and charge values of the NO<sub>2</sub> molecule for the investigated cases are presented in Table 2. In all cases, the adsorbed molecule was geometry-optimized, using either (1) a frozen slab cleaved from the bulk geometry without further optimization, (2) the frozen slab used throughout the present thesis (cf. Table 1), (3) additional relaxation of the surface adsorption site atom, (4) additional relaxation of the complete first slab layer.

Investigated cases of surface relaxation	(1)		(2)		(3)		(4)	
	GGA	GGSA	GGA	GGSA	GGA	GGSA	GGA	GGSA
Adsorption energy [eV]	-0.6	-0.5	-0.7	-0.6	-0.8	-0.7	-0.8	-0.7
Distance O <sub>surf</sub> - NO <sub>2</sub> [pm]	229.3	229.3	236.7	234.5	253.1	250	246.5	245.2
Distance O - NO [pm]	123.7	123.6	123.8	123.8	124.1	124.2	124.6	124.5
Angle ONO [°]	128.6	128.8	127.9	127.6	126.6	126.6	125.7	125.6
Mulliken charge analysis. Net electron transfer to adsorbate [e]	-0.3	-0.3	-0.4	-0.4	-0.4	-0.4	-0.5	-0.5
Interlayer distance Ba <sub>surf</sub> (top layer) - O (2 <sup>nd</sup> layer) [pm]	276.1	276.1	268.2	268.2	268.2	268.2	288.1	285.7
Interlayer distance O <sub>surf</sub> (top layer) - Ba (2 <sup>nd</sup> layer) [pm]	276.1	276.1	262.7	262.7	243.5	245.8	249.5	250.5

**Table 3.2:** Influence of surface relaxation and spin polarization on the DFT results. (1) Frozen slab cleaved from the bulk geometry without further optimization, (2) geometry-optimized (cf. Table 1) and subsequently frozen slab, (3) additional relaxation of the surface adsorption site atom, (4) additional relaxation of the complete first slab layer. GGA = general gradient approximation, GGSA = general gradient spin approximation. Case (2)/GGA corresponds to the calculations performed throughout this thesis.



Fig. 3.8 shows the calculated adsorption energies of an  $\text{NO}_2$  molecule adsorbed on a  $\text{BaO}(100)$  surface in a  $(1 \times 1)$  supercell for all investigated cases of relaxation. The results showed that the induced error due to neglecting spin effects and surface relaxation was small compared to other effects such as surface coverage (see Chapter 4). The adsorption energy gained by full relaxation in comparison to the fully non-relaxed surface was  $\sim 0.25$  eV. In all cases, spin polarized (DFT-GGSA) and unpolarized (DFT-GGA) calculations resulted in a difference in adsorption energies of only 0.1 eV and almost insignificant difference in the geometry of the adsorbed molecule. The same influence of the spin effect was obtained for  $\text{NO}_2$  adsorption on larger supercells and also for  $\text{NO}$ . These results are also in agreement with earlier studies of  $\text{NO}$  on  $\text{Rh}(111)$  [45]. It is interesting to note that the energy gain from additional surface relaxation is to a large extent canceled by the energy loss due to the inclusion of spin effects.

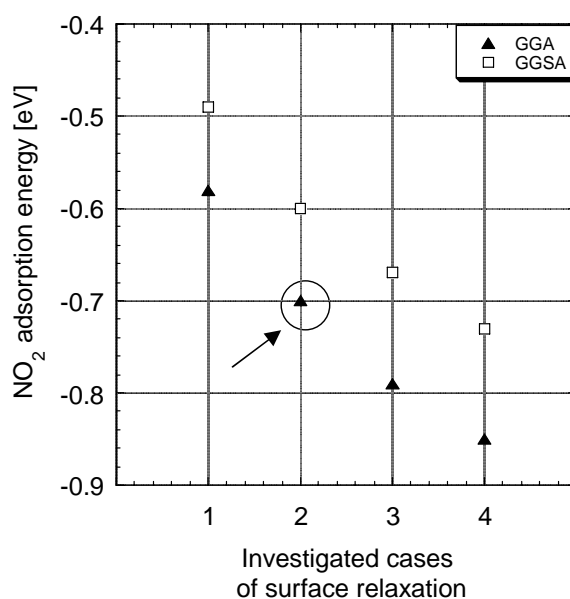


**Fig. 3.8:**  $\text{NO}_2$  adsorption energy dependence on surface relaxation and spin polarization. The marked case corresponds to the calculations performed throughout this thesis.

### 3.6 Computational Time of CASTEP Calculations - Examples

In Subchapter 3.4 it was claimed that DFT calculations are numerically extremely challenging, and the assumptions used throughout this thesis were also chosen in order to keep computational times to a reasonable limit. The computational time required for a CASTEP calculation increases with the cube of the number of atoms in the system. Three examples are given in the following:

(I) Geometry optimization of an NO molecule at surface coverage 0.5, 0.25 and 0.125. The calculations have been performed both spin-polarized and un-polarized. The results are shown in Fig. 3.9.

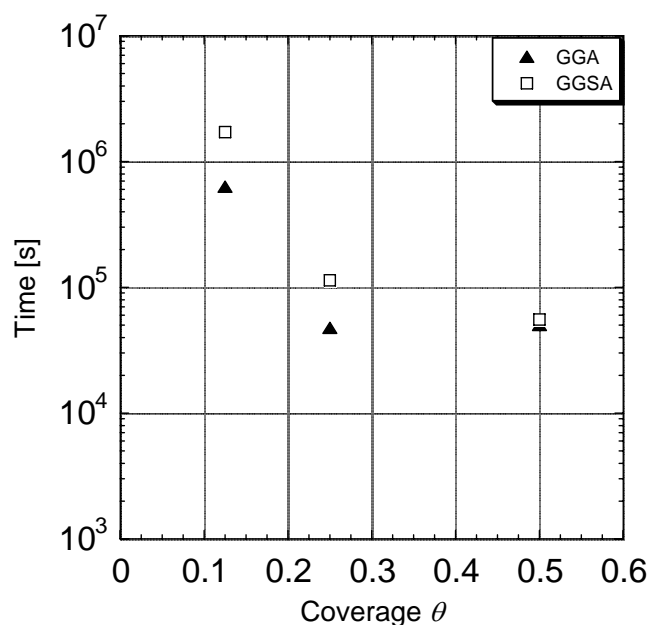


**Fig. 3.9:** Time of calculation for geometry optimization of an NO molecule in dependence on surface coverage and on spin polarization.

The computational time cost multiplies by 12 between surface coverages 0.5 and 0.125 respectively while for the spin-polarized and unpolarized calculations at the same surface coverage 0.125, the time increases by a factor of 2.7.

(II) Geometry optimization of an  $\text{NO}_2$  molecule at surface coverages 0.5 and 0.25. Again, calculations have been performed both spin-polarized (GGSA) and un-polarized (GGA). The results are shown in Fig. 3.10. The calculation time cost is 2.8 times higher between surfaces coverage of 0.5 and 0.25, while between spin un-polarized and polarized calculations for the same surface coverage the calculation time is 1.5 times higher.

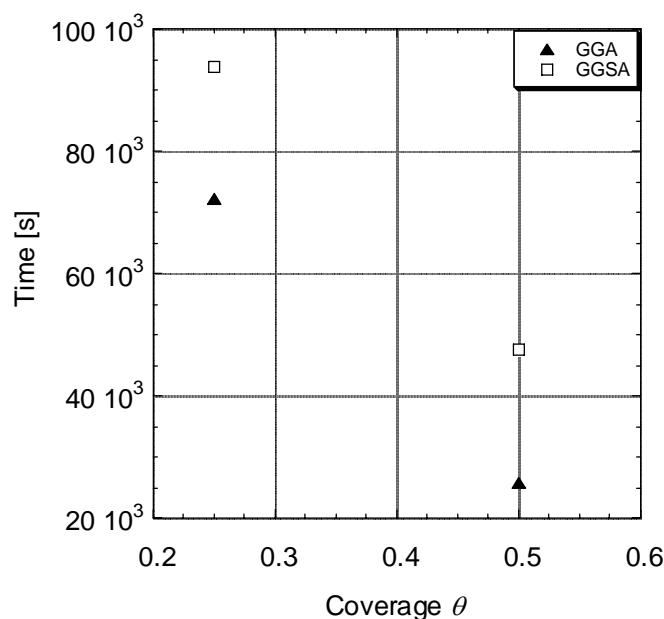


**Fig. 3.10:** Time calculation for geometry optimization of an  $\text{NO}_2$  molecule dependence on surface coverage and on spin effect.

(III) Geometry optimization of an  $\text{NO}_2$  molecule at surface coverage 0.5 for different cases of surface relaxation: (1) a frozen slab cleaved from the bulk geometry without further optimization, (2) the frozen slab used throughout the present thesis (cf. Table 1), (3) additional relaxation of the surface adsorption site atom, (4) additional relaxation of the complete first slab layer.

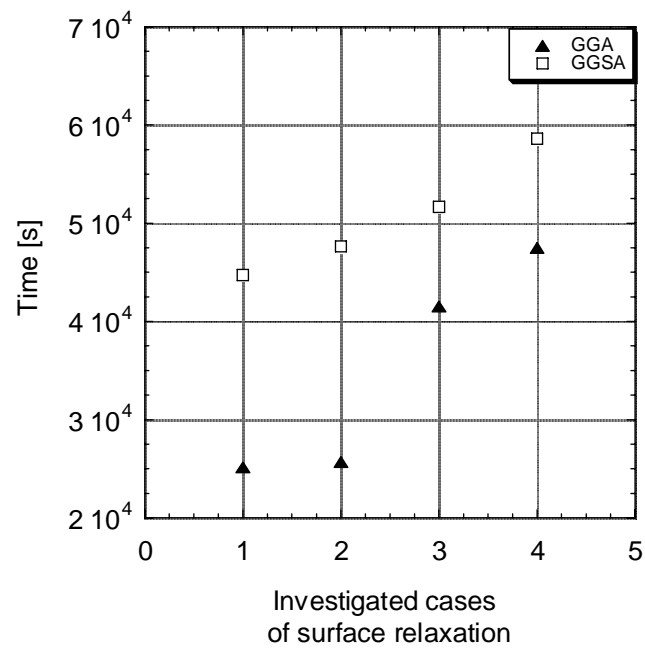


**Fig. 3.11:** Calculation times for different cases of surface relaxation (cf. Subchapter 3.5)

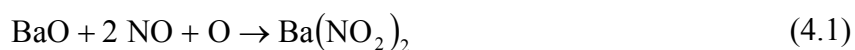
In this example the computational cost increases as follows:

- 1.6 times between cases (1)/GGA and (3)/GGA
- 1.8 times between cases (1)/GGA and (3)/GGSA
- 2.2 times between the fully non-relaxed surface (1)/GGA and full relaxation (4)/GGSA

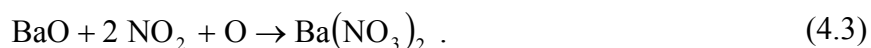
## Chapter 4: NO, NO<sub>2</sub>, CO<sub>2</sub> and H<sub>2</sub>O Adsorption on BaO(100)

Storage catalytic converters based on barium compounds are a technology with promising potential for the abatement of nitric oxides (NO<sub>x</sub>) from lean-burning engine exhaust [7,48]. However, despite considerable research effort, the chemical-mechanistic details of these storage and release processes are not very well understood [19,49-52]. The nature of the active storage sites (barium oxide, barium hydroxide, barium carbonate, or other compounds) still remains an open question [53]. Lietti *et al.* [54,55] showed that at  $T = 360^\circ\text{C}$  BaO, Ba(OH)<sub>2</sub>, and BaCO<sub>3</sub> coexist at the surface and that NO<sub>x</sub> storage occurs first at the Ba sites in the oxide form, then the hydroxide and finally the carbonate. Gas-phase species present under real operating conditions, such as carbon dioxide (CO<sub>2</sub>) and water (H<sub>2</sub>O), may influence the nature of the storage site, even if they are not directly involved in the storage process. They play an essential role in the surface processes during NO<sub>x</sub> storage on BaO, where it can block available surface sites, affecting the NO<sub>x</sub> storage capacity. Recently, previous experimental work on NO<sub>x</sub> storage and reduction catalysts has been reviewed by Epling *et al.* [56]. Several NO<sub>x</sub> storage mechanisms pathways proposed by experiments have been summarized in Ref. 56 as follows:

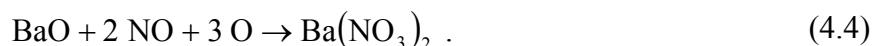
- Barium nitrites formed from BaO, NO, and oxygen and subsequent oxidation leads to formation of barium nitrates [57-59],



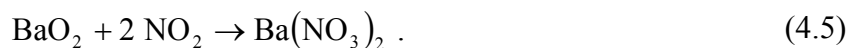
- NO<sub>2</sub> molecules react with the Ba species precursor and oxygen to form the barium nitrate [53,54,57-62],



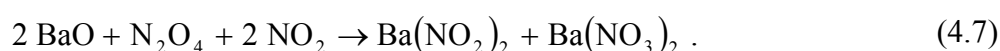
- NO molecules react with the Ba species precursor and multiple oxygen atoms to form nitrate [19,57,58,62],



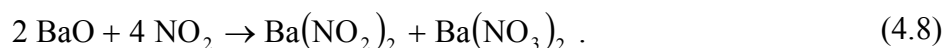
- Barium peroxide as an intermediate reacts to form nitrates [50,61,63],



- An N<sub>2</sub>O<sub>4</sub> dimer forms and reacts with the surface to form a mixture of nitrites and nitrates. The nitrites are subsequently oxidized to nitrates [54,64],



- A mixture of nitrites and nitrates are formed from NO<sub>2</sub> and oxygen. Again the nitrites are subsequently oxidized to nitrates [19,58,65],



Quantum mechanical calculations based on density-functional theory (DFT) have been used previously to study NO<sub>x</sub> interaction with BaO surfaces using either periodic-slab calculations [66-69] or cluster calculations [70-72]. However, in these studies the dependence of the adsorbate-surface interaction on surface coverage was not considered.

In order to bring more light into these questions, in the present work density-functional theory (DFT) quantum chemical calculations were performed to study adsorption of the relevant gas-phase species NO, NO<sub>2</sub>, CO<sub>2</sub> and H<sub>2</sub>O on BaO(100) surfaces. BaO(100) was chosen as a model surface for NO<sub>x</sub> storage as laboratory studies have shown that BaO is indeed a material with storage capacity [19], and moreover it has a lower structural complexity compared to other compounds (e.g. BaCO<sub>3</sub> [68]). Adsorption geometry and adsorption energy of NO, NO<sub>2</sub>, CO<sub>2</sub> and H<sub>2</sub>O in dependence on adsorption site and surface coverage were calculated. Adsorbate coverages were varied by choosing various lateral sizes of the supercell. In particular, surface coverages  $\theta$  of 0.5, 0.25, and 0.125 were obtained by studying single molecules adsorbed on the center atom of a (1×1), ( $\sqrt{2} \times \sqrt{2}$ ), and (2×2) unit cell, respectively. A slab structure with four atomic layers obtained as described in Chapter 3 was used.

#### 4.1 Pure Bulk and Gas-phase Species

Initially, the bulk geometry of cubic barium oxide, as well as the geometries of the various adsorbents investigated, were optimized using the DFT method as described in Chapter 2. The results are given in Table 4.1. The calculated bond distances and angles agree within 2% with reported experimental values.

	This work		Experiment [73,74]	
	bond distance [pm]	bond angle [°]	bond distance [pm]	bond angle [°]
BaO (bulk, cubic)	278	–	276	–
NO (gas)	118.6	–	114	–
NO <sub>2</sub> (gas)	122	133.7	120	134
CO <sub>2</sub> (gas)	117	179.9	116	180
H <sub>2</sub> O (gas)	97	105.1	96	104.5

**Table 4.1:** Comparison of DFT-calculated bulk and molecular geometries with reported experimental values.

#### 4.2 Nitrogen Monoxide (NO) Adsorption

The NO<sub>x</sub> in exhaust gas exits the engine primarily as NO. Under typical working conditions of NSR catalysts, Ba nitrites have been detected primarily at low temperatures (150°C - 200°C) [50,75,76] while at higher temperatures the Ba nitrates are the dominant species [59,75]. This is due to the lower stability of nitrites compared to nitrates at high temperatures. The nitrite species are considered to be precursors for the nitrate species.

Previous experiments [19,77] and DFT studies [67,72] have shown that nitric oxide (NO) adsorbs on barium oxide as nitrite-like species over an O<sub>surf</sub> site. In this work, DFT calculations were performed to investigate the coverage-dependence of NO molecular adsorption on a BaO(100) surface.

Figure 4.1 shows the optimized geometry of an adsorbed NO molecule on BaO(100) over an O<sub>surf</sub> site in a (1×1) supercell corresponding to a surface coverage  $\theta = 0.5$ . The optimized structure of the nitric oxide molecule is in good agreement with the ones reported by previous DFT studies [67,72]. The nitrogen atom resides 154.3 pm above the O<sub>surf</sub> site, the distance within the adsorbate molecule is  $d(\text{N-O}) = 126.5$  pm, and the O<sub>surf</sub>-N-O angle is 108.1°.

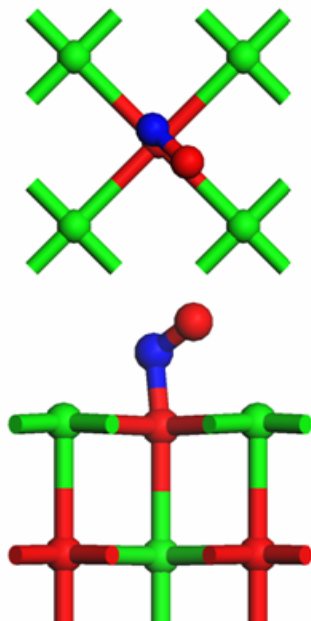


**Fig. 4.1:** Top and side view of the optimized structure of NO molecular adsorption over an O<sub>surf</sub> site on BaO(100) surface.

The influence of surface coverage on adsorption energies was investigated for coverages  $\theta$  of 0.5, 0.25, 0.125. The calculated NO adsorption energies are shown in Fig. 4.2, and geometric, energetic, and charge-transfer values are given in Table 4.2.



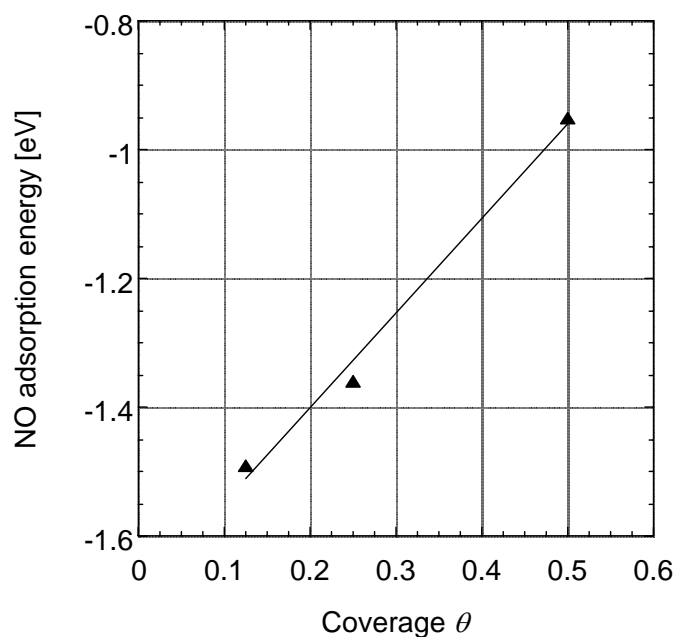


**Fig. 4.2:** Coverage dependence of NO adsorption energy. The line represents a linear fit (cf. Table 4.6).

The results show a strong interaction of the molecule with the basic surface anion even at high coverage ( $E_{\text{ads}} = -1.0$  eV at  $\theta = 0.5$ ), with almost linearly decreasing adsorption energy for decreasing coverage ( $E_{\text{ads}} = -1.5$  eV at  $\theta = 0.125$ ). The high adsorption energies, relatively short distance from the surface ( $d(\text{N-O}_{\text{surf}}) = 147.8$  pm at  $\theta = 0.125$ ) and an  $\text{O}_{\text{surf}}\text{-N-O}$  angle of  $110^\circ$  support the nitrite-like nature of this species (cf. free nitrite anion [73]:  $d(\text{N-O}) = 123.6$  pm,  $\text{ONO} = 115^\circ$ ).

The strong NO interaction with the surface is further supported by the Mulliken charge analysis performed which shows a high net electron transferred from the surface to the molecule. The NO adsorption energy versus net electron transferred from the surface to the adsorbate is shown in Figure 4.3.

Surface coverage	Distance surface atom – adsorbate atom [pm]	Bond distance within adsorbate [pm]	Bond angle of adsorbate [°]	Adsorption energy [eV]	Mulliken charge analysis. Net electron transfer to adsorbate [e]
$\theta = 0.125$ (Fig. 4.2)	147.8	129.7	109.7	-1.49	-0.8
$\theta = 0.25$ (Fig. 4.2)	147.8	128.9	109.8	-1.36	-0.7
$\theta = 0.5$ (Fig. 4.1; 4.2)	154.3	126.5	108.1	-0.95	-0.6

**Table 4.2:** Energetic and geometrical parameters of NO molecular adsorption on BaO(100) at different surface coverages.

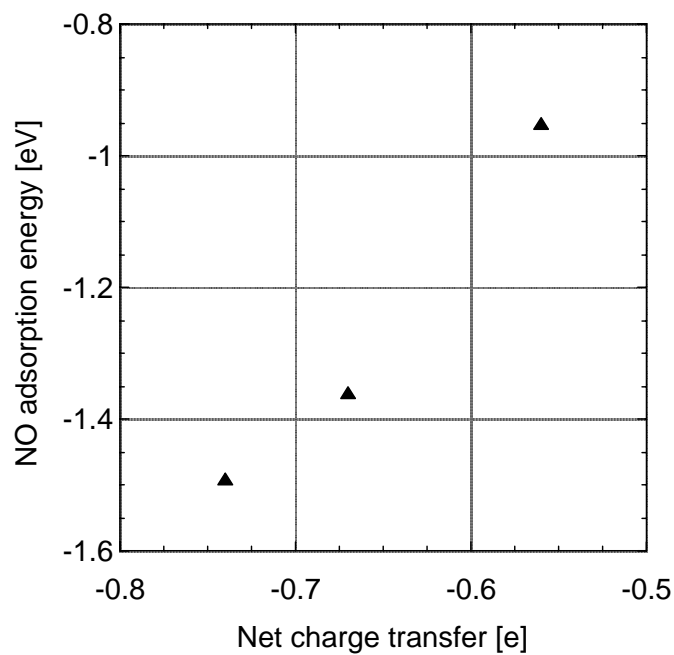


**Fig. 4.3:** NO adsorption energy dependence on the net electron transfer.

### 4.3 Nitrogen Dioxide (NO<sub>2</sub>) Adsorption

Molecular adsorption of NO<sub>2</sub> on BaO is believed to be the first step involved in the overall NO<sub>x</sub> storage mechanism [51,78]. Various adsorbate geometries have been identified both experimentally [49,77] and via quantum chemical calculations [67,69], including N- or O-bonded adsorbates, bridged chelate-type structures, and adsorption over either barium or oxygen surface sites (Ba<sub>surf</sub> or O<sub>surf</sub>, respectively). In this work the stability of two representative adsorption geometries, an O<sub>surf</sub>-NO<sub>2</sub> species and a Ba<sub>surf</sub>-O<sub>2</sub>N chelate-type species, was investigated. The optimized geometries are shown in Figure 4.4 for a (1×1) supercell ( $\theta = 0.5$ ).

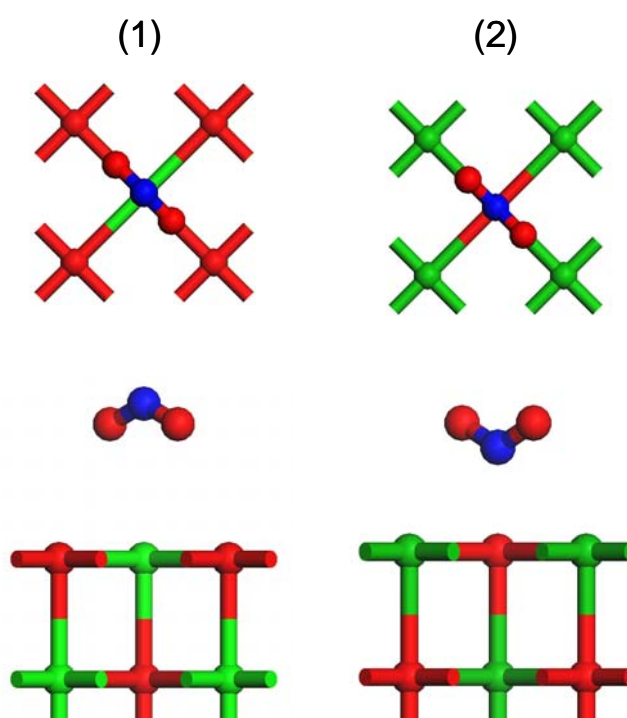


**Fig. 4.4:** Top and side view of the optimized structures of a NO<sub>2</sub> molecule adsorbed on BaO(100) surface for a surface coverage of  $\theta = 0.5$ . Structure (1) represents adsorption over a Ba<sub>surf</sub> site and structure (2) adsorption over an O<sub>surf</sub> site.

In both cases, the NO<sub>2</sub> molecule interacts strongly with the BaO(100) surface forming stable adsorbates ( $E_{\text{ads}} = -0.6$  eV for adsorption over a Ba<sub>surf</sub> atom and  $E_{\text{ads}} = -0.7$  eV adsorption over an O<sub>surf</sub> atom) with relatively long distances above the surface ( $d(\text{Ba}_{\text{surf}}\text{-N}) = 355.4$  pm,  $d(\text{O}_{\text{surf}}\text{-N}) = 236.7$  pm). Geometrical values of the optimized structures are given in Table 4.3.

Adsorbate structure	Distance surface atom – adsorbate atom [pm]	Bond distance within adsorbate [pm]	Bond angle of adsorbate [°]	Adsorption energy [eV]	Mulliken charge analysis. Net electron transfer to adsorbate [e]
NO <sub>2</sub> -Ba <sub>surf</sub> , $\theta = 0.125$ (Fig. 4.5)	361.3	126.3	120.0	-1.27	-0.6
NO <sub>2</sub> -Ba <sub>surf</sub> , $\theta = 0.25$ (Fig. 4.5)	358.5	125.1	122.9	-0.93	-0.5
NO <sub>2</sub> -Ba <sub>surf</sub> , $\theta = 0.5$ (Fig. 4.4, 4.5)	355.4	124.0	125.8	-0.6	-0.3
NO <sub>2</sub> -O <sub>surf</sub> , $\theta = 0.125$ (Fig. 4.5)	233.2	125.2	124.4	-1.13	-0.6
NO <sub>2</sub> -O <sub>surf</sub> , $\theta = 0.25$ (Fig. 4.5)	234.9	124.6	126.1	-0.9	-0.5
NO <sub>2</sub> -O <sub>surf</sub> , $\theta = 0.5$ (Fig. 4.4, 4.5)	236.7	123.8	127.9	-0.7	-0.4

**Table 4.3:** Adsorption energies and geometrical parameters of NO<sub>2</sub> molecular adsorption on BaO(100)

The influence of surface coverage on NO<sub>2</sub> adsorption energy was again studied for coverages  $\theta$  of 0.5, 0.25, and 0.125. The results are shown in Figure 4.5, and geometric, energetic, and charge-transfer values are given in Table 4.3.

The calculations show a strong dependence of adsorption energy on coverage, with the energy generally decreasing (i.e., the adsorbed molecule becoming more stable) with decreasing coverage. Calculated adsorption energies reach values down to -1.3 eV for the lowest investigated coverage ( $\theta = 0.125$ ). Results of a Mulliken charge analysis are shown in Figure 4.6. The adsorption energy increases linearly with increasing net charge transferred from the BaO surface to the adsorbed NO<sub>2</sub> molecule.

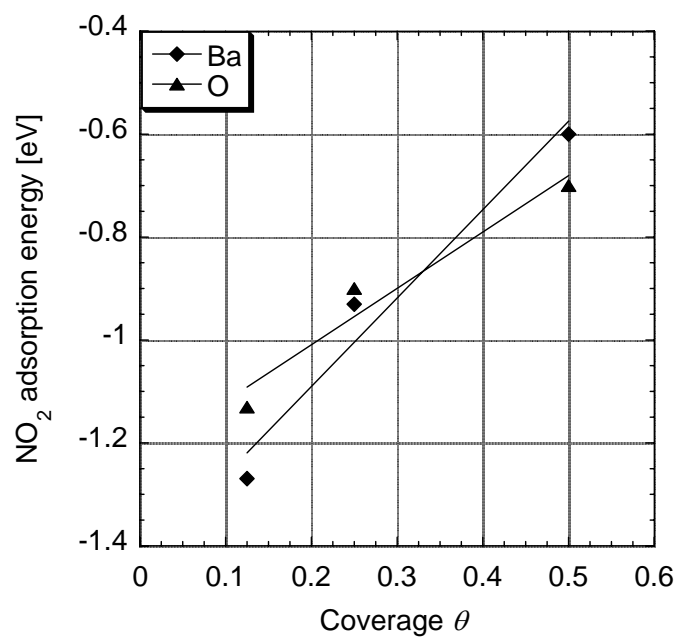


**Fig. 4.5:** Coverage dependence of NO<sub>2</sub> adsorption energy over a Ba<sub>surf</sub> site and an O<sub>surf</sub> site. The lines represent linear fits (cf. Table 4.6).

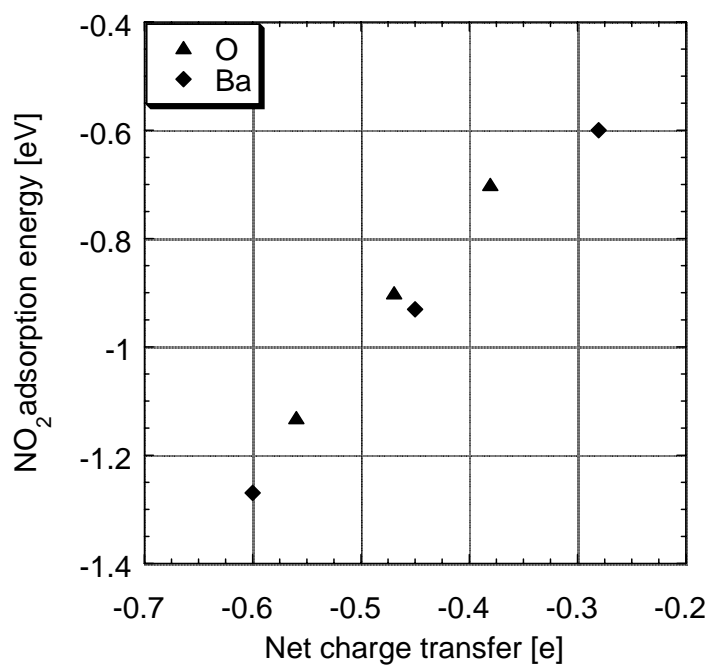


**Fig. 4.6:** Dependence of NO<sub>2</sub> adsorption energy over Ba<sub>surf</sub> and O<sub>surf</sub> sites on the net electron transfer.

#### 4.4 Carbon Dioxide (CO<sub>2</sub>) Adsorption

In the presence of CO<sub>2</sub>, formation of barium carbonates is expected. Experiments showed that CO<sub>2</sub> has indeed a negative impact on NSR catalysts trapping capacity [53,54,61,79,80].

Molecular adsorption of CO<sub>2</sub> on BaO represents a first step in the formation of carbonates. Using cluster DFT calculations, Karlsen *et al.* [71] observed two different adsorbate configurations for CO<sub>2</sub> on metal oxides: a strongly adsorbed (chemisorbed) species with nonlinear geometry on BaO, and a weakly adsorbed (physisorbed), almost linear species on MgO.

In the present work, for CO<sub>2</sub> adsorption on BaO(100) three local minima representing three different states have been identified on the potential-energy surface (PES). The optimized structures on a (1×1) supercell ( $\theta=0.5$ ) are shown in Figure 4.7.

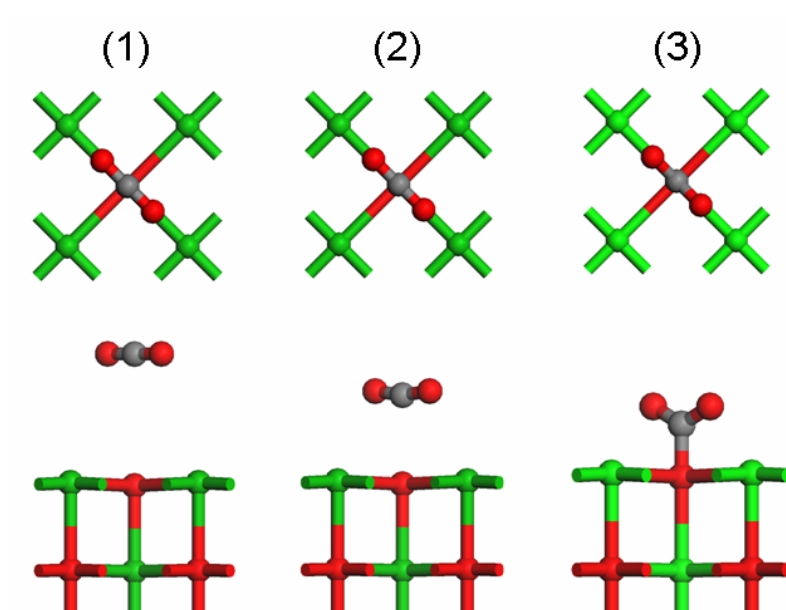


**Fig. 4.7:** Geometry of the three investigated adsorbate states of molecular CO<sub>2</sub>: (1) gas-phase, (2) physisorbed, (3) chemisorbed, carbonate-type species.

The results show a gas-phase species (Structure 1, cf. Fig. 4.7), a physisorbed species (Structure 2, cf. Fig. 4.7) almost linear and a chemisorbed species with a non-linear geometry (Structure 3, cf. Fig. 4.7). The adsorption energies of the three adsorbate states are plotted in Figure 4.8.

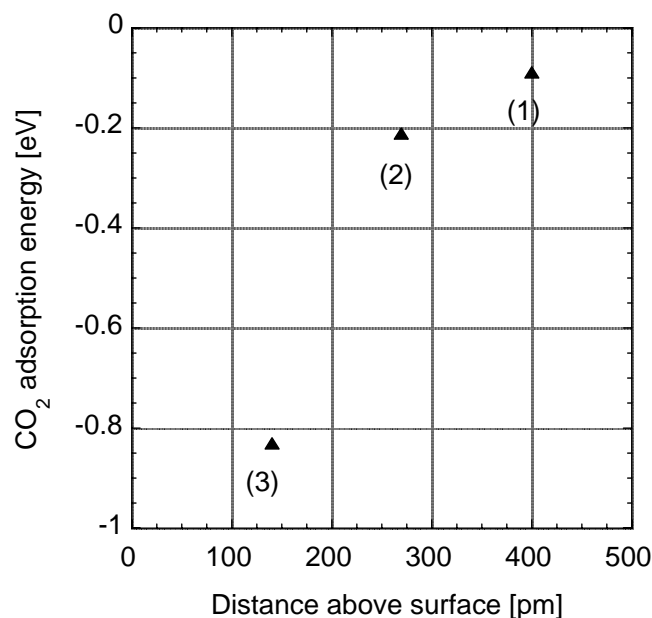


**Fig. 4.8:** Adsorption energy versus distance above the surface for the three investigated adsorbate states of CO<sub>2</sub> (cf. Fig. 4.7).

Further investigations of the three different molecular states are shown in Figs. 4.9, 4.10 and 4.11. Single point energy calculations of the CO<sub>2</sub> molecule adsorbed on BaO have been performed for different distances of the molecule above the surface: between 399.5 and 409.5 pm for the gas-phase species, between 261 and 285 pm for the physisorbed species and 137 and 156 pm for the chemisorbed state. The local minima correspond to the stable structures shown in Fig. 4.7, with distances above the surface of 404.5 pm, 278 pm and 147.1 pm respectively.

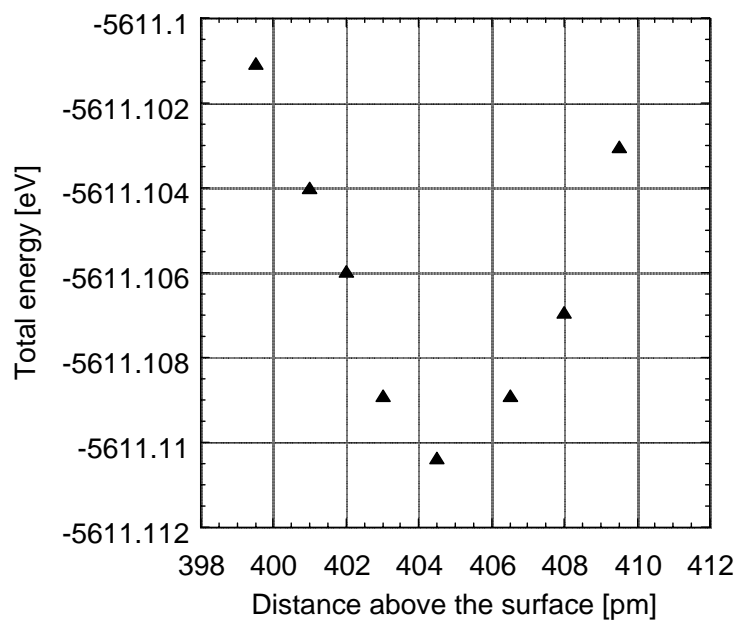


**Fig. 4.9:** Total energy dependence of the CO<sub>2</sub> gas-phase species on the distance of the molecule above the surface.

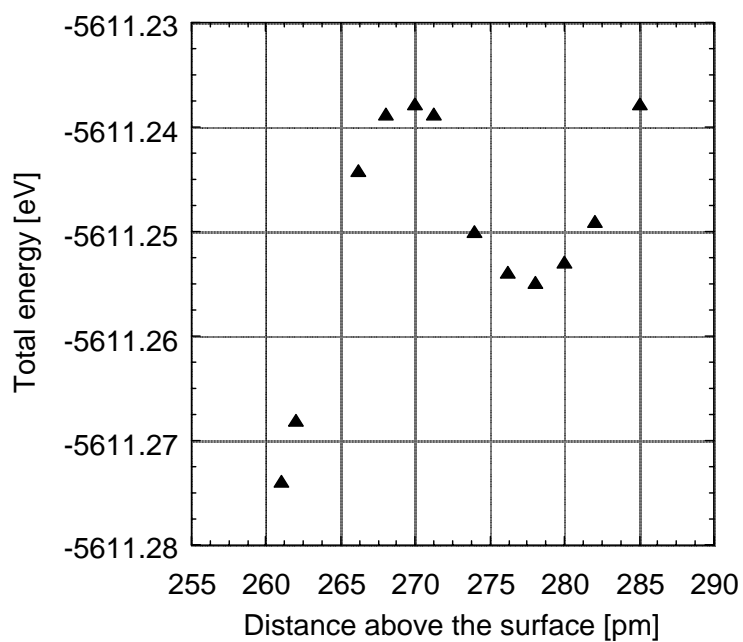


**Fig. 4.10:** Total energy dependence of the CO<sub>2</sub> physisorbed species on the distance above the surface.



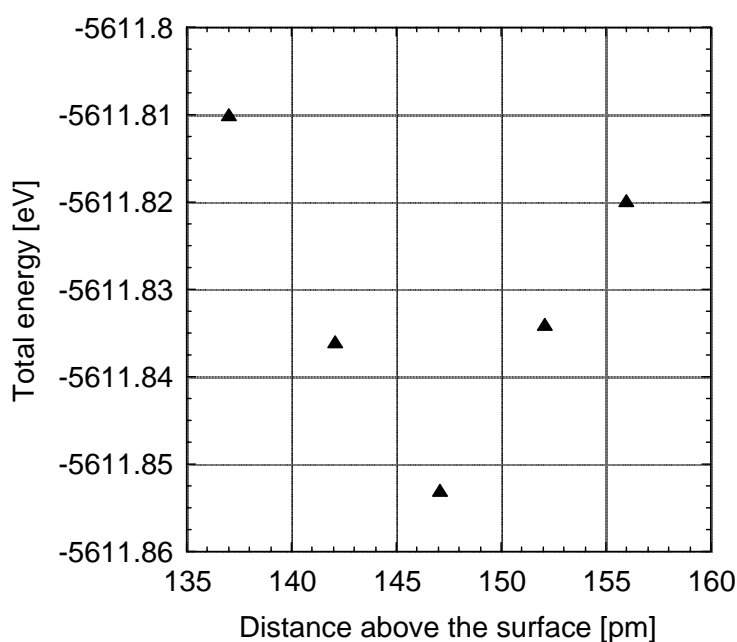


**Fig. 4.11:** Total energy dependence of the CO<sub>2</sub> chemisorbed species (carbonate type species) on the distance of the molecule above the surface.

The gas-phase species has a very low adsorption energy ( $E_{\text{ads}} = -0.1$  eV) and resembles very well the experimental geometrical parameters. It has a bond distance of  $d(\text{O-C}) = 116.9$  pm and a bond angle of  $\text{OCO} = 179.5^\circ$  (cf. experiment [73]  $d(\text{O-C}) = 116$ ,  $\text{OCO} = 180^\circ$ ). The physisorbed species adsorbs weakly with an energy of  $E_{\text{ads}} = -0.2$  eV, it has an almost linear geometry  $d(\text{O-C}) = 117.5$  pm and a bond angle of  $\text{OCO} = 168.8^\circ$ . The chemisorbed species is very stable ( $E_{\text{ads}} = -0.8$  eV). It has a carbonate-type structure involving one surface O atom ( $d(\text{O}_{\text{surf}}\text{-C}) = 147$  pm,  $d(\text{O-C}) = 123$  pm,  $\text{OCO} = 131.6^\circ$ ; cf. carbonate [73]:  $d(\text{O-C}) = 130$  pm,  $\text{OCO} = 120^\circ$ ). The calculations thus indicate the formation of a surface carbonate.

Geometric, energetic, and charge-transfer values of these structures are given in Table 4.4.

Adsorbate structure	Distance surface atom – adsorbate atom [pm]	Bond distance within adsorbate [pm]	Bond angle of adsorbate [°]	Adsorption energy [eV]	Mulliken charge analysis. Net electron transfer to adsorbate [e]
CO <sub>2</sub> , $\theta = 0.5$ (Fig. 4.7(1))	404.5	116.9	179.5	-0.09	0
CO <sub>2</sub> , $\theta = 0.5$ (Fig. 4.7(2))	278.0	117.5	168.8	-0.21	-0.2
CO <sub>2</sub> , $\theta = 0.125$ (Fig. 4.12)	140.6	125.5	125.8	-1.7	-0.8
CO <sub>2</sub> , $\theta = 0.25$ (Fig. 4.12)	142.3	124.9	127.5	-1.36	-0.8
CO <sub>2</sub> , $\theta = 0.5$ (Fig. 4.7(3), 4.12)	147.1	123.6	131.6	-0.83	-0.6

**Table 4.4:** Adsorption energies and geometrical parameters for CO<sub>2</sub> adsorption on BaO(100).

The coverage dependence of the CO<sub>2</sub> adsorption energy (carbonate-type structure) is shown in Fig. 4.12, and additional data is given in Table 4.4.

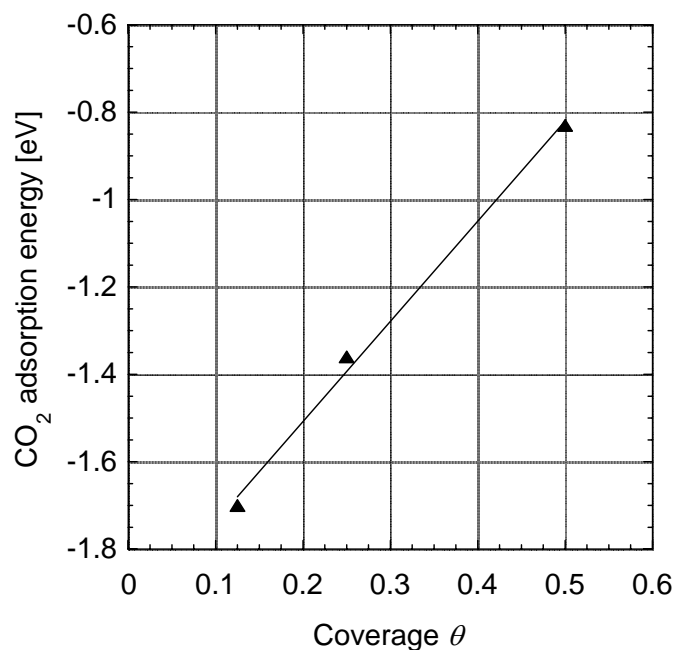


**Fig. 4.12:** Coverage dependence of CO<sub>2</sub> adsorption energy. The line represents a linear fit (cf. Table 4.6.)

The adsorption energy decreases strongly (i.e., the adsorbed molecule becomes more stable) with decreasing coverage, as in the case for NO<sub>2</sub> adsorption, reaching adsorption energies of -1.7 eV for the lowest investigated coverage ( $\theta = 0.125$ ).

The CO<sub>2</sub> adsorption energy versus net charge transferred from the surface to the adsorbate, according to a Mulliken population analysis, is shown in Fig. 4.13. Similar as for NO<sub>2</sub> adsorption, the net electron transfer decreases with increasing the coverage, but the effect is stronger for the CO<sub>2</sub> molecule. This confirms the strong electronic interaction of this molecule with the surface.

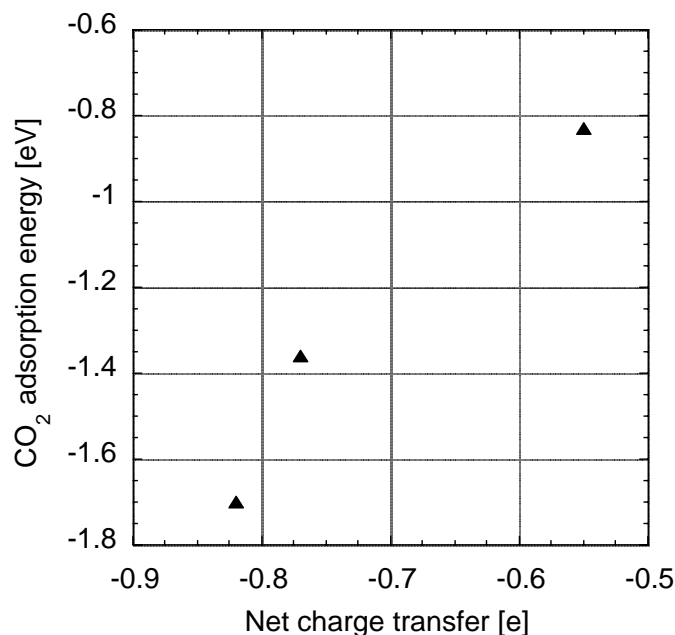


**Fig. 4.13:** CO<sub>2</sub> adsorption energy dependence on the net electron transfer.

#### 4.5 Water Adsorption (H<sub>2</sub>O)

H<sub>2</sub>O play a significant role in the NO<sub>x</sub> storage process. Experimental studies showed that the presence of H<sub>2</sub>O during the lean operation phase reduces the storage capacity up to 16% [79], reduces the overall catalyst performance [80] and decreases the stability of nitrate species [81].

In humid atmospheres, the surface of oxidic substrates is usually considered to be completely saturated with H and OH molecules [82]. This is due to the highly Lewis-basic and -acidic character of the free surface oxygen and metal ions, respectively. Water adsorption on BaO surfaces has not been investigated in earlier DFT studies. However, H<sub>2</sub>O on magnesium oxide (MgO) has been intensively investigated both experimentally [83] and theoretically [84-87], and it was observed that water can adsorb both molecularly and dissociatively.

In the present work adsorption geometry and energy of adsorbed H<sub>2</sub>O in dependence on surface coverage was investigated. Various different adsorption configurations (molecular and dissociative adsorption over different sites) were investigated. The optimized geometry of the

most stable structure on a (1×1) supercell is shown in Fig. 4.14, and geometrical parameters are given in Table 4.5.

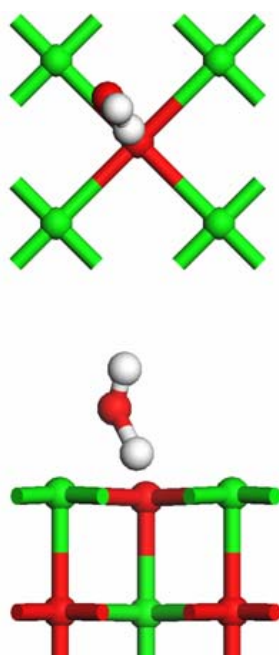


**Fig. 4.14:** Top and view side of the optimized geometry of a H<sub>2</sub>O molecule adsorbed on BaO(100) surface at surface coverage  $\theta = 0.5$ .

Adsorbate structure	Distance surface atom – adsorbate atom [pm]	Bond distance within adsorbate [pm]	Bond angle of adsorbate [°]	Adsorption energy [eV]	Mulliken charge analysis. Net electron transfer to adsorbate [e]
H <sub>2</sub> O, $\theta = 0.125$ (Fig. 4.16)	104.8	97.0 (O-H <sup>a</sup> ) 145.9 (O-H <sup>b</sup> )	126.2	-1.45	-0.4
H <sub>2</sub> O, $\theta = 0.25$ (Fig. 4.16)	106.5	97.0 (O-H <sup>a</sup> ) 141.1 (O-H <sup>b</sup> )	124.0	-1.13	-0.3
H <sub>2</sub> O, $\theta = 0.5$ (Fig. 4.14, 4.16)	108.7	96.7 (O-H <sup>a</sup> ) 137.8 (O-H <sup>b</sup> )	117.2	-0.94	-0.3

<sup>a</sup>Upper H atom

<sup>b</sup>Lower H atom

**Table 4.5:** Energetic and geometrical parameters of H<sub>2</sub>O molecular adsorption on BaO(100).

A strong adsorption energy ( $E_{\text{ads}} = -0.9$  eV) in the same range as for NO and CO<sub>2</sub> is observed. The optimized geometry has a short distance above the surface ( $d(\text{HOH}-\text{O}_{\text{surf}}) = 108$  pm,  $d(\text{H}_2\text{O}-\text{Ba}_{\text{surf}}) = 259$  pm), one short OH bond typical for an H<sub>2</sub>O molecule ( $d(\text{H}-\text{OHO}_{\text{surf}}) = 97$  pm) and a second, elongated OH bond ( $d(\text{HO}-\text{HO}_{\text{surf}}) = 137$  pm). The structure thus represents a partially dissociated water molecule forming a stable complex with O<sub>surf</sub> and Ba<sub>surf</sub> sites.

The adsorption energy of a fully dissociated structure (HO–Ba<sub>surf</sub> and H–O<sub>surf</sub>, Fig. 4.15) was also calculated. It varies between 0.1 and 0.5 eV for  $\theta = 0.5-0.125$  and is therefore considerable less stable. Hydrogen bonding between co-adsorbed water molecules [88] could not be identified in the present study. Note, however, that the adsorption behavior can be different at stepped surfaces [72,89]. The adsorption/dissociation behavior of water on oxidic surfaces is complex, and a full understanding of these effects would require further investigations, which are beyond the scope of the present study.

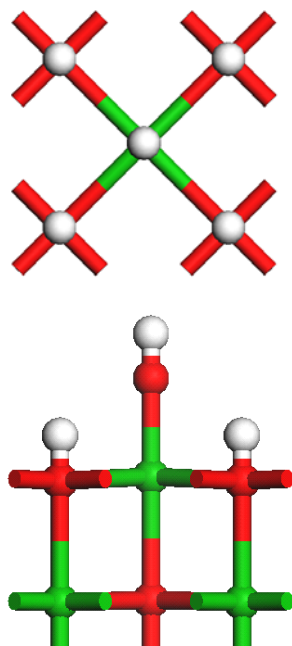


**Fig. 4.15:** Top and view side of the optimized geometry of dissociatively adsorbed water on BaO(100) surface at surface coverage  $\theta = 0.5$

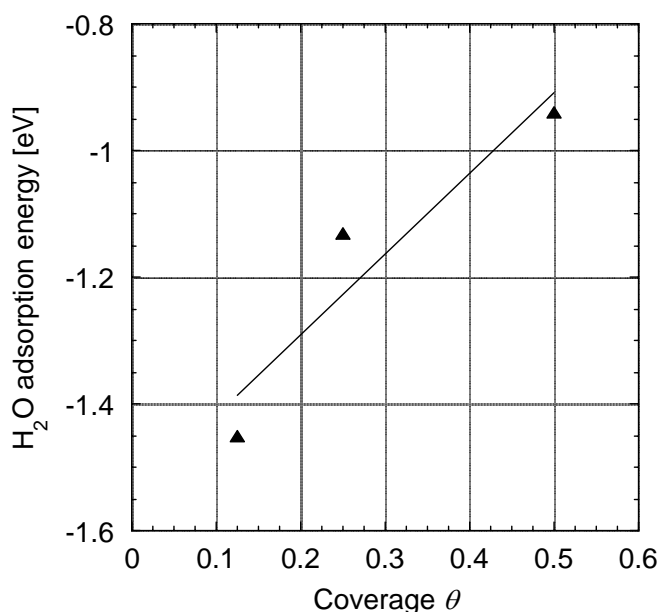


**Fig. 4.16:** Coverage dependence of H<sub>2</sub>O adsorption energy. The line represents a linear fit (cf. Table 4.6).

The influence of surface coverage on adsorption energy of the stable structure is shown in Fig. 4.16. As in the case for NO, NO<sub>2</sub> and CO<sub>2</sub>, a strong dependence is observed with adsorption energies becoming more stable with decreasing coverage. At high surface coverage  $\theta = 0.5$  the adsorption energy is -0.9 eV while for the lowest investigated coverage  $\theta = 0.125$  an adsorption energy of -1.5 eV is obtained. The strong H<sub>2</sub>O interaction with the BaO surface is further supported by a Mulliken charge analysis. The values for the electron transfer from the surface to the adsorbate are given in Table 4.5. A higher net electron donation is observed with decreasing surface coverage. The electron donation is lower than the one observed for NO, NO<sub>2</sub> and CO<sub>2</sub>.

Various geometries of the water molecule have been investigated for molecular adsorption on MgO(100) [84-86]. The calculated binding energies for H<sub>2</sub>O adsorption on BaO are slightly higher than the values reported for molecular water adsorption on MgO(100) [84-87]. Previous theoretical [85-87] studies of water adsorption on MgO(100) have also shown that dissociative adsorption of a single water molecule is an unfavorable process and only the presence of three or four water molecules leads to dissociative adsorption stabilized by hydrogen-bonding due to lateral interaction from neighboring water molecules.

## 4.6 Comparison to Previous DFT Studies

Density-functional theory calculations of the interaction of NO, NO<sub>2</sub> and CO<sub>2</sub> with BaO surfaces were previously published by several authors using either periodical-slab (Broqvist *et al.*, ( $\sqrt{2} \times \sqrt{2}$ ) [66]; Broqvist *et al.*, (3×3) [69]; Schneider, ( $\sqrt{8} \times \sqrt{8}$ ) [67]) or cluster (Broqvist *et al.* [70], Karlsen *et al.* [71], Branda *et al.* [72]) methods. There is quite some variation in these data. NO adsorption energies vary from -0.8 eV [72] to -1.5 eV [67], adsorption energies for NO<sub>2</sub> over an O<sub>surf</sub> site vary from -0.8 eV [70] to -1.5 eV [67], and CO<sub>2</sub> adsorption energies vary from -1.7 [71] to -2.3 eV [67]. In the case of NO<sub>2</sub>, this discrepancy was pointed out by Broqvist *et al.* [69] and ascribed to be probably due to differences in allowed surface relaxation. The present studies on surface relaxation (cf. Chapter 3) indicate that surface relaxation indeed plays a role, but its influence is too small (~0.25 eV difference in NO<sub>2</sub> adsorption energy between a non-relaxed and a fully relaxed slab) to be at the origin of the variation observed in literature. Instead, in the light of the results presented in this chapter, these variations can be explained to a large extent by the strong coverage-dependence of the adsorption energy. This is true for NO, NO<sub>2</sub> and CO<sub>2</sub>, as discussed in the following.

A comparison of the calculated NO adsorption energy in this work with previous studies is shown in Fig. 4.17. While the geometrical parameters are similar in all studies (bond angle ~110°, short distances above the surface of ~150 pm,  $d(\text{O-N}) \sim 128$  pm), the adsorption energies are quite different. For the periodic-slab calculations, the almost linear increase of adsorption energy with increasing surface coverage is obvious.

Fig. 4.18 shows calculated adsorption energies for NO<sub>2</sub> over an O<sub>surf</sub> site versus coverage for various studies. Again, the results of the various periodical-slab calculations fall together with the coverage dependent calculations performed in this study.

A summary of data for CO<sub>2</sub> adsorption over an O<sub>surf</sub> site is shown in Fig. 4.19. All studies show the formation of the stable carbonate-type species. This is also indicated by the calculated OCO bond angles (Karlsen *et al.*: 130°, Schneider: 126°, this work: 125.8°, ideal carbonate: 120°). Again, the difference in adsorption energies can be explained from the influence of surface coverage.



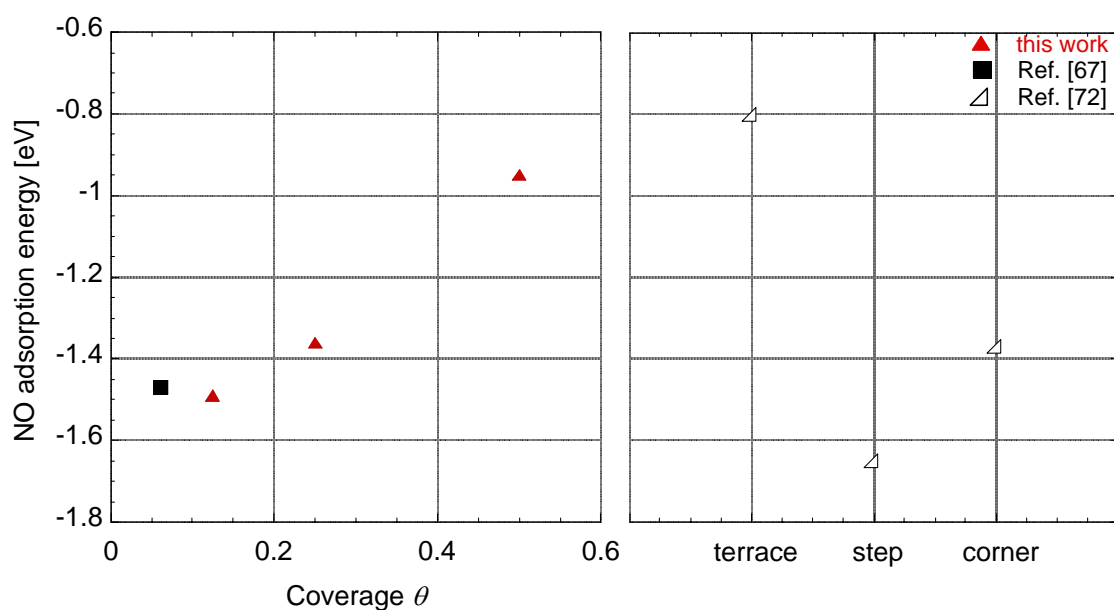


**Fig. 4.17:** NO adsorption energy obtained from various studies. The left panel represents DFT periodical-slab calculations, the right panel DFT cluster calculations.

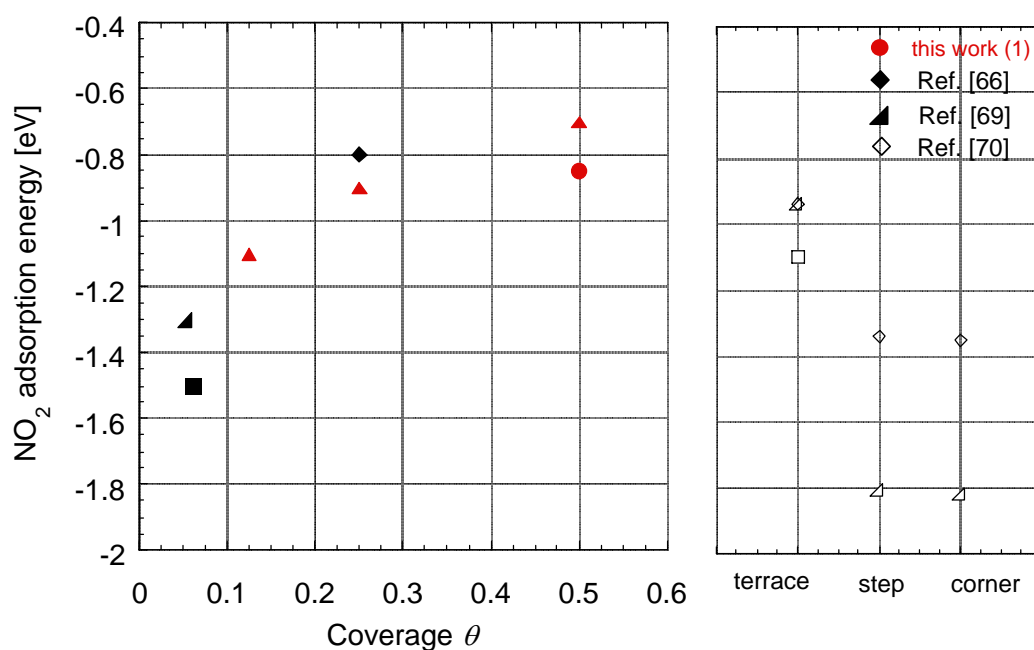


**Fig. 4.18:** Adsorption energy of NO<sub>2</sub> over an O<sub>surf</sub> site obtained from various studies. The left panel represents DFT periodical-slab calculations, the right panel DFT cluster calculations. (1) Adsorption energy after complete relaxation of the first slab layer.

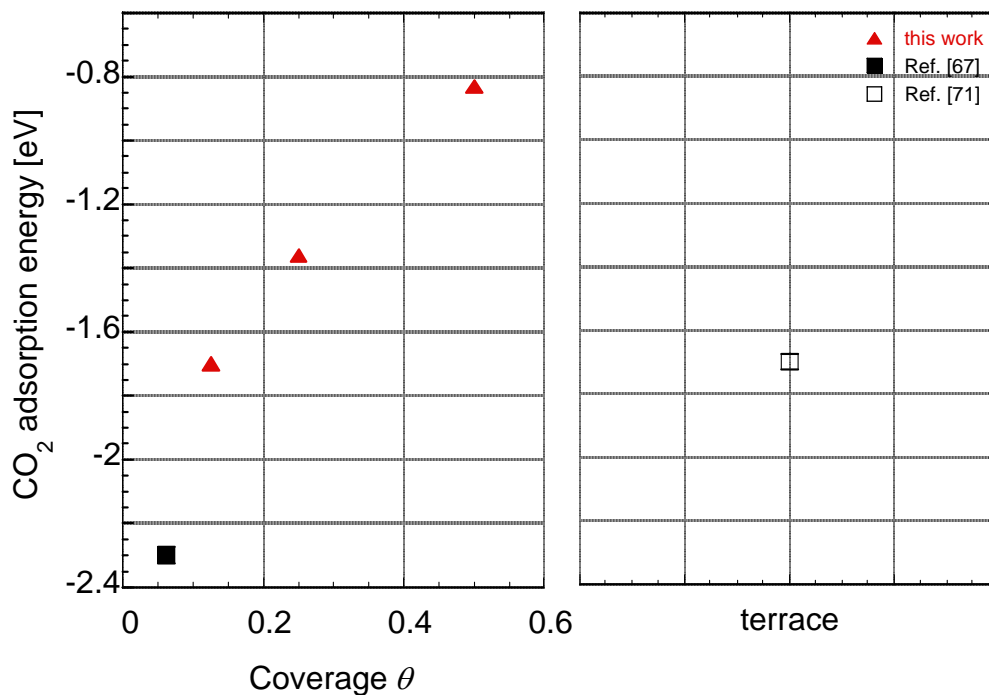


**Fig. 4.19:** Adsorption energy of CO<sub>2</sub> over an O<sub>surf</sub> site obtained from various studies. The left panel represents DFT periodical-slab calculations, the right panel DFT cluster calculations.

Combining the results of all authors, Figs. 4.17-4.19 clearly show the almost linear dependence of adsorption energy on surface coverage for all three species. The scatter in the data can be interpreted as an additional, smaller effect of surface relaxation: In the present study, the two upper layers of a four-layer slab were relaxed and frozen (cf. Chapter 3); Schneider [67] uses a fully relaxed three-layer slab; Broqvist *et al.* use a non-relaxed surface where only the adsorbent oxygen atom is geometry-optimized [66], respectively a fully relaxed first slab layer [69]. Figs. 4.17-4.19 further illustrate the problem of comparing the results from cluster calculations. Here, a direct relation to a particular coverage of flat surfaces is not possible. The adsorption energy of a cluster terrace site seems to correspond rather accidentally to coverages of 0.5 in the case of NO, and to coverages of 0.125 in the case of NO<sub>2</sub> and CO<sub>2</sub>. The strong influence of coverage on adsorption energy is likely to be ascribed to adsorbate-adsorbate interactions. They can principally consist of through-space and through-surface interactions. As the adsorbate stability keeps increasing even for coverages < 0.25, through-space interactions seem rather unlikely. Instead, surface-mediated effects from electron withdrawal by the adsorbates is probably the origin of this observation. Similar

effects were observed by Broqvist *et al.* for NO<sub>2</sub> adsorption on BaCO<sub>3</sub> [68], and by Inderwildi *et al.* for rhodium surfaces [45,89]. This interpretation is supported also by the Mulliken charge analyses that were performed in this work (Figs. 4.3, 4.6 and 4.13): for each species there is an almost linear relationship between adsorption energy and the charge exchanged between surface and adsorbate. This is indicative of the adsorbates' competition for slab electrons.

Different authors also studied various NO<sub>2</sub> adsorption geometries. Apart from the “N-down” geometry investigated here, Schneider and Broqvist *et al.* have additionally identified a nitrate-type species with short N-O<sub>surf</sub> bond, and a bridged Ba<sub>surf</sub>–ONO–Ba<sub>surf</sub> species. All three geometries have different electronic structure [69], but only a small difference in adsorption energy  $\leq 0.1$  eV [67,69]. Both Broqvist *et al.* and Schneider also observed that pair formation of two NO<sub>2</sub> adsorbates leads to an additional stabilization in the order of 0.2-0.3 eV per molecule through electronic effects [66,67]. Evidently, there is a large variety of possible adsorption geometries for NO<sub>2</sub> on a BaO surface. However, the combined results from the various studies show that the difference in adsorption energy for various adsorption configurations is considerable smaller than for various surface coverages.

#### 4.7 Linear Fit of the Coverage Dependence of NO, NO<sub>2</sub>, CO<sub>2</sub> and H<sub>2</sub>O

In order to use the DFT results obtained above for a quantification of the competitive adsorption of the four gas-phase species (the results of this study are presented in Chapter 6), a linear fit of the coverage dependence results was considered.

The coverage dependence is described using a simple linear relationship,

$$E_{\text{ads DFT}} = E_{\text{ads}}^0 + \varepsilon * \theta, \quad (4.9)$$

where the parameters  $E_{\text{ads}}^0 = E_{\text{ads}}(\theta=0)$  and  $\varepsilon$  are obtained by linear regression of the data shown in Figs. 4.2, 4.5, 4.12 and 4.15. Their values are given in Table 4.6.

	$E_{\text{ads}}^0$ [eV]	$\varepsilon$ [eV]
NO (ads)	-1.69	1.46
NO <sub>2</sub> -O <sub>surf</sub> (ads)	-1.23	1.09
NO <sub>2</sub> -Ba <sub>surf</sub> (ads)	-1.43	1.72
CO <sub>2</sub> (ads)	-1.96	2.29
H <sub>2</sub> O (ads)	-0.54	1.27

**Table 4.6:** Linear fit parameters of the coverage dependence of NO, NO<sub>2</sub>, CO<sub>2</sub> and H<sub>2</sub>O (cf. Eq. 4.9)

## 4.8 Conclusions

The adsorption of four gas-phase species important in automotive exhaust gas catalysis (NO, NO<sub>2</sub>, CO<sub>2</sub> and H<sub>2</sub>O) on a BaO storage catalyst surface was investigated with quantum chemical calculations based on density-functional theory. Adsorption geometries and energies were calculated in dependence of surface coverage. All species form stable adsorbates on the BaO(100) surface. The adsorption energies strongly depend on surface coverage through electronic effects.

The most important observations are summarized as follows.

- NO adsorbs as stable nitrite-like species.
- NO<sub>2</sub> may adsorb in various geometries on both barium and oxygen surface sites. Variation in adsorption energy for different geometries at constant coverage is considerably smaller (~25%) than for varying surface coverage (~100% increase between coverages of 0.5 and 0.125). This observation allows to explain the disagreement of calculated adsorption energies in the existing literature.
- Upon interaction of CO<sub>2</sub> with a BaO surface, three local minima representing three different states: a gas-phase, a physisorbed and a chemisorbed species have been found on the potential-energy surface (PES). The chemisorbed state is very stable ( $E_{\text{ads}}(\theta = 0.125) = -1.7$  eV) and together with one surface oxygen atom forms a carbonate-type structure.
- H<sub>2</sub>O adsorbs strongly on BaO surface, with adsorption energies in the same range as NO, NO<sub>2</sub> and CO<sub>2</sub>.

## **Chapter 5: Oxygen Adsorption, Dissociation and Surface Diffusion on Pt(111)**

The platinum surface plays an essential role in automotive exhaust gas purification as an oxidation catalyst. In order to understand these reactions, oxygen interactions with platinum have been intensively investigated using various experimental [46,90-110] and theoretical [42,43,47,111-115] methods. A first review of oxygen adsorption on this surface has been presented by Gland [90]. More recently, previous work of oxygen interaction with Pt (111) has been summarized by Gustafsson [104]. It has been shown that oxygen may adsorb on platinum molecularly, dissociatively or forming a layer of adsorbed oxide.

For molecular adsorption different spectroscopic techniques have been used to characterize the molecular states: ultra-violet photoemission spectroscopy (UPS) [91,93,98,110], electron energy loss spectroscopy (EELS) [91,93,95,101,102], thermal desorption spectroscopy (TDS) [91-93,95,96,106,110], scanning tunneling microscopy (STM)[100], low energy electron diffraction (LEED) [46,90,92,93,98,103,106], infrared reflection absorption spectroscopy (IRAS) [104] and near edge X-ray absorption spectroscopy (NEXAFS) [94,97,98]. Three molecular states have been identified: at low temperature ( $T < 40$  K) one weakly physisorbed species and at higher temperatures ( $40 \leq T \leq 150$  K) two strongly chemisorbed species [98,104]. The experimental results assigned the two chemisorbed states to a peroxo ( $\text{O}_2^{2-}$ ) species adsorbed on the hollow site and to a superoxo ( $\text{O}_2^-$ ) species formed on the bridge site. IRAS [104] and EELS [93,101] measurements observed two distinct vibrational frequencies for the chemisorbed states:  $700 \text{ cm}^{-1}$  and  $870 \text{ cm}^{-1}$ , respectively. *Ab-initio* DFT calculation performed by Eichler *et al.* [47] supported the existence of two different chemisorbed molecular states. Two local minima representing two different states have been identified on the potential-energy surface (PES). The conclusion of all these studies was that the physisorbed state acts as precursor to the chemisorbed states. At temperatures  $T > 150$  K, the  $\text{O}_2$  molecule dissociates.

In case of dissociative adsorption, the atomic oxygen was found to be chemisorbed in an fcc or hcp threefold site with the former as the most favorable one [42,111,112,115].

It has been shown previously that the surface coverage can have a significant effect on thermodynamic and kinetic properties of surface-attached species via steric or electronic (surface-mediated) adsorbate-adsorbate interactions [41,90,92,99,116]. These effects also influence the observed catalyst behavior on a macroscopic scale. This has been shown, for example, in the context of exhaust-gas catalysis by Inderwildi [117]. Kinetic simulations needed to take into account coverage-dependent reaction rates in order to achieve agreement with experimental data.

In the present work density-functional theory (DFT) quantum chemical calculations were performed to investigate O<sub>2</sub> adsorption and decomposition on clean and oxygen pre-covered Pt(111) surfaces. Furthermore, diffusion of atomic oxygen between fcc-threefold and hcp-threefold positions as well as the influence of different coadsorbates on the diffusion process was studied. Kinetic parameters of the reactions of dioxygen and the diffusion of atomic oxygen on the surface and their dependence on surface coverage were determined.

The Pt surface is modeled as a slab consisting of three atomic layers, extending by symmetry to an infinite surface. Adsorbate coverages were obtained either by increasing the number of surface ad-atoms on a (2×4) supercell (studies of molecular oxygen reactions) or by choosing various lateral sizes of the supercell (studies of atomic oxygen diffusion). The influence of different coadsorbates on the diffusion process has been investigated on a (2×2) supercell. In all investigated cases, the adsorbate's coordinates were allowed to geometry-optimization while the periodic slab cleaved from the optimized bulk geometry was frozen. The three-dimensional periodic slabs were separated from the subsequent slabs by a 1000 pm vacuum thickness.

Adsorption energies  $E_{\text{ads}}$  were calculated as the difference between the total surface energy (slab with adsorbate after geometry optimization) and the sum of the energies of the surface slab precovered with atomic oxygen and gas-phase oxygen molecule after geometry optimization. The adsorption energies were calculated according to

$$E_{\text{ads}} = E_{(\text{slab} + n \times \text{O} + \text{O}_2)} - (E_{\text{slab} + n \times \text{O}} + E_{\text{O}_2}) \quad (5.1)$$

where  $n$  is the number of oxygen atoms on the surface.

## 5.1 Platinum Bulk and Molecular Oxygen

Using the DFT method as described in Chapter 2 the geometry of bulk platinum was optimized prior to all subsequent calculations on the Pt surface. The calculated Pt bulk lattice constant of 401.8 pm is in good agreement with previous reported experimental [105,118] and theoretical [42,47,112,119] values. For the optimized gas-phase oxygen molecule a bond length of 123 pm was obtained again in good agreement with previous DFT studies [41,111] and experiments [73].

## 5.2 Molecular Oxygen Adsorption on Pt (111)

Experiments [90-94,97,98,100-104] and theoretical [43,47,111-113] studies have been intensively used to investigate molecular oxygen adsorption on the Pt(111) surface. Former studies identified a stable oxygen molecule adsorbed in a side-on geometry with the O–O bond parallel to the surface.

In this work, initially, the stability of three single adsorbate configurations, (1) oxygen molecule parallel to the surface (side-on) adsorbed on a bridged configuration, (2) oxygen molecule perpendicular (end-on) to the surface considering adsorption on an fcc site and (3) end-on adsorption on a hcp hollow site, was investigated. The calculations were performed on a (2×4) supercell corresponding to a surface coverage  $\theta = 0.125$ . The optimized geometries for the stable adsorbates are shown in Fig. 5.1 and energetic and geometrical parameters of the optimized structures are given in Table 5.1. The results showed stable structures for all investigated cases, with a more favorable configuration of molecular oxygen adsorbed on a side-on bridged geometry. In this case, the O<sub>2</sub> molecule interacts strongly ( $E_{\text{ads}} = -1.89$  eV) with the Pt(111) surface; it has a bridge position with a distance above the surface of 188 pm, a platinum-oxygen distance of 204 pm and an intermolecular oxygen-oxygen distance of 135 pm (slightly longer compared to the gas phase). The calculated geometrical parameters are in very good agreement with previous theoretical [47,112,113] and experimental [97] results. For the adsorption energies of molecular oxygen there is a large variation from 0.38 to 4.21 eV in reported values. This is probably due to the different experimental or theoretical methods.

The calculated adsorption energy for the side-on (bridged) geometry is higher than theoretical results obtained by Bocquet *et al.* [112] (0.53 eV) and Eichler *et al.* [47] (0.72 eV), and experimental results obtained by Gland *et al.* [91] (0.38 eV), but lower than microcalorimetric measurements obtained by Brennan *et al.* [105] (3.05 eV) and theoretical calculations performed by Chan *et al.* [43] (4.21 eV; note: the extended Hückel method used by Chan *et al.* is known for overestimating adsorption energies).

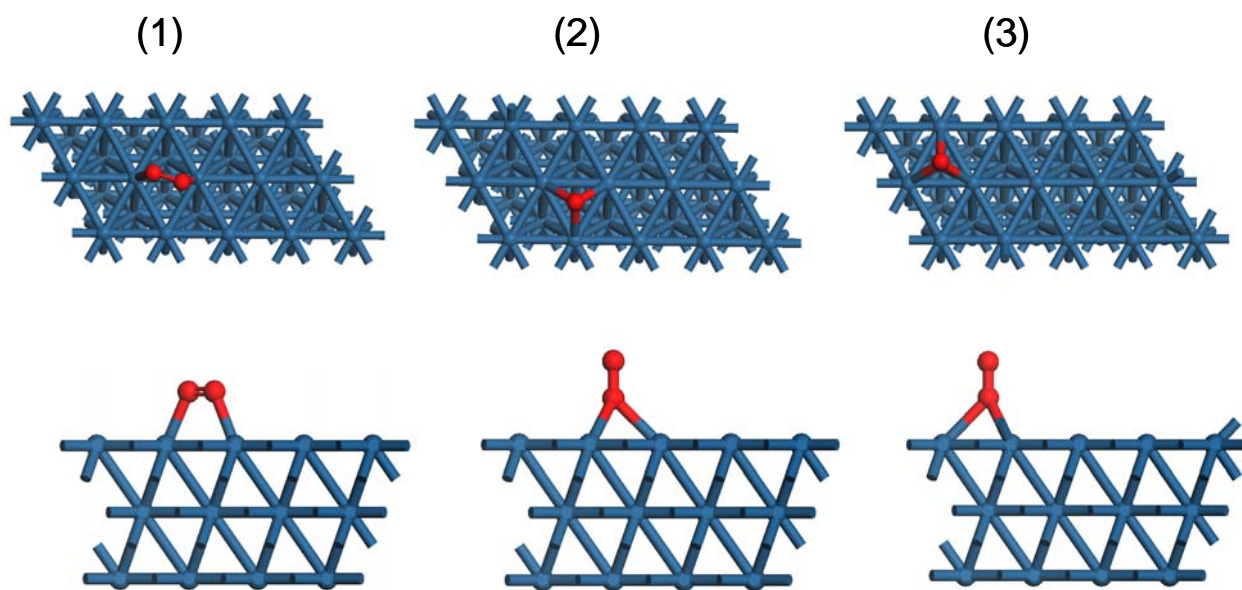


**Fig. 5.1** : Top and side views of the optimized geometries of molecular oxygen adsorption on Pt(111): (1) side-on geometry adsorbed in an bridged configuration; (2) end-on geometry adsorbed on an fcc threefold site; (3) end-on geometry adsorbed on a hcp threefold site.



	side-on (bridge)	end-on (fcc)	end-on (hcp)
$E_{\text{ads}}$ [eV]	-1.89	-0.98	-0.89
$d(\text{O}^1\text{-surface})$ [pm]	188.0	159.8	168
$d(\text{O}^2\text{-surface})$ [pm]	188.9	-	-
$d(\text{O}^1\text{-O}^2)$ [pm]	135.4	128.1	127.2
$d(\text{O}^1\text{-Pt})$ [pm]	205.4	$a = b = 228.6$ $c = 229.8$	$a = 234.4$ $b = 234.9$ $c = 235.3$
$d(\text{O}^2\text{-Pt})$ [pm]	204.2		

**Table 5.1:** Energetic and geometrical parameters of three configurations of the  $\text{O}_2$  molecule adsorbed on Pt(111) surface in a  $(2 \times 4)$  supercell.  $\text{O}^1$  is the oxygen atom pointing towards the surface of the end-on geometry.  $\text{O}^2$  is the uppermost oxygen atom of the end-on geometry.  $a$ ,  $b$ ,  $c$  are the distances of the oxygen atom pointing ( $\text{O}^1$ ) towards the surface to the three closest Pt atoms.

The bonding strength of the oxygen molecule adsorbed in an fcc-threefold position (end-on manner) was furthermore analyzed in dependence on surface coverage varying the number of pre-adsorbed oxygen atoms on the platinum surface. The adsorption energies were calculated according to Eq. 5.1. The obtained geometrical parameters of the optimized structures, energetic and charge values of molecular oxygen adsorption on Pt(111) for all investigated surface coverages are given in Table 5.2.

Surface coverage	O <sub>2</sub> molecular adsorption					O <sub>2</sub> dissociation		
	$E_{\text{ads}}$ [eV]	$d(\text{O}^1\text{-O}^2)$ [pm]	$d(\text{O}^1\text{-surf.})$ [pm]	$d(\text{O-Pt})$ [pm]	Mulliken charge [e]	$E_a$ [eV]	$\Delta H$ [eV]	Mulliken charge transition state [e]
$\theta = 0.125$	-0.98	128.1	159.8	$a = 228$ $b = 228$ $c = 229$	-0.31	0.40	-1.69	-0.35
$\theta = 0.25$	-0.97	128.3	160.5	$a = 228$ $b = 229$ $c = 230$	-0.31	0.62	-1.53	-0.64
$\theta = 0.375$	-1.00	128.8	149.7	$a = 221$ $b = 222$ $c = 223$	-0.35	0.72	-1.2	-0.64
$\theta = 0.50$	-0.96	127.9	177.4	$a = 215$ $b = 240$ $c = 294$	-0.26	0.91	-0.87	-0.64
$\theta = 0.625$	-1.01	129.6	168.4	$a = 220$ $b = 221$ $c = 293$	-0.30	0.95	-0.17	-0.65
$\theta = 0.750$	-1.14	125.8	202.5	$a = 204$ $b = 326$ $c = 342$	-0.15	1.65	-1.70	-0.63
$\theta = 0.875$	-1.05	125	203.2	$a = 204$ $b = 364$ $c = 369$	-0.11	2.67	1.00	-0.63

**Table 5.2:** Calculated kinetic parameters of molecular oxygen on Pt(111) at different surface coverages. O<sup>1</sup> is the oxygen atom pointing towards the surface. O<sup>2</sup> is the uppermost oxygen atom of the end-on geometry.  $a$ ,  $b$ ,  $c$  are the distances of the oxygen atom pointing (O<sup>1</sup>) towards the surface to the three closest Pt atoms.

Fig. 5.2 shows the resulting binding energies as a function of coverage. The results show almost constant adsorption energies with increasing surface coverage, indicating molecular oxygen adsorption is essentially unaffected by precovering the surface with atomic oxygen. For the more reactive Pt(110) surface, King *et al.* [99] obtained experimentally an initial adsorption heat of 3.44 eV which decreased rapidly with coverage to 2.22 eV at  $\theta = 0.35$  and to 1.58 eV in the steady-state regime. For this surface Freyer *et al.* [107] suggested a change in adsorption site at  $\theta = 0.2$  and estimated it as the saturation coverage. For the less reactive Pt(111) surface, molecular oxygen has a saturation coverage of  $\theta = 0.15$  to 0.5 in the previous reported values [93,98,106,110]. Gland *et al.* [90] performing microcalorimetric measurements observed a decrease in adsorption energy with increasing initial surface coverage. They found that molecular oxygen is bound to a clean surface by 0.35 eV while to a surface saturated with adsorbed atomic oxygen by 0.16 eV.

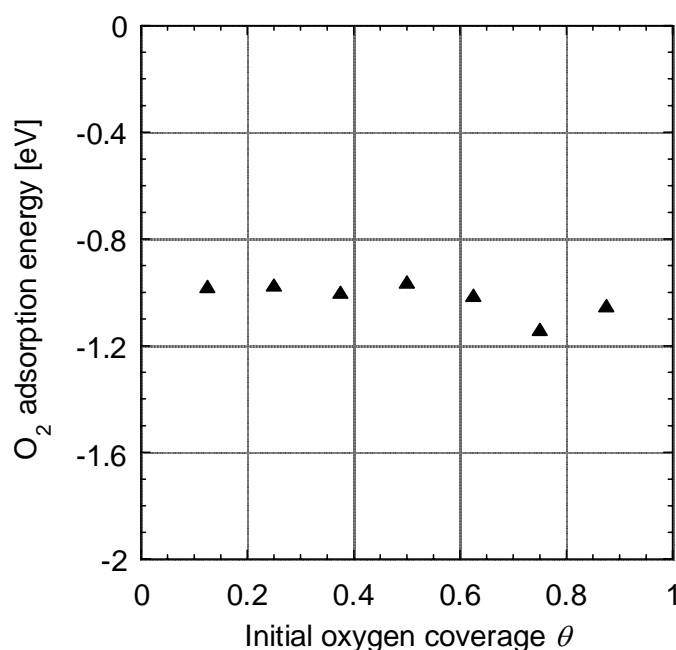


**Fig. 5.2:** O<sub>2</sub> adsorption energy dependence on surface coverage.

Analyzing the intermolecular O–O bond length with increasing coverage the present calculations indicate that the oxygen molecule is adsorbed slightly weaker with increasing surface coverage. The oxygen-oxygen bond distance decrease from 128.1 pm at surface coverage  $\theta = 0.125$  to 125 pm for the highest investigated coverage  $\theta = 0.875$ . The following interpretation of the observed behavior can be given: The electronegative oxygen withdraws

electrons from the metal surface and hence lowers the back-donation effect of the metal into the antibonding  $\pi$  orbital of the adsorbed molecular oxygen species. This effect is increased when further oxygen withdraws electrons from the metal surface. The suggested weaker back-donation effect is supported by bond length analysis: The distance above the surface of the  $O_2$  molecule increase with increasing surface coverage from 159 pm at surface coverage 0.125 to 203 pm at coverage 0.875. The geometry of the oxygen molecule is bent at high coverages ( $\theta \geq 0.625$ ) towards the decomposed configuration due to repulsive interactions between the O atoms. The result is further supported by the Mulliken charge analysis performed. Fig. 5.3 displays the net electron transferred from the platinum surface to the adsorbed molecule versus coverage. An almost constant net electron donation is observed with increasing surface adatoms.

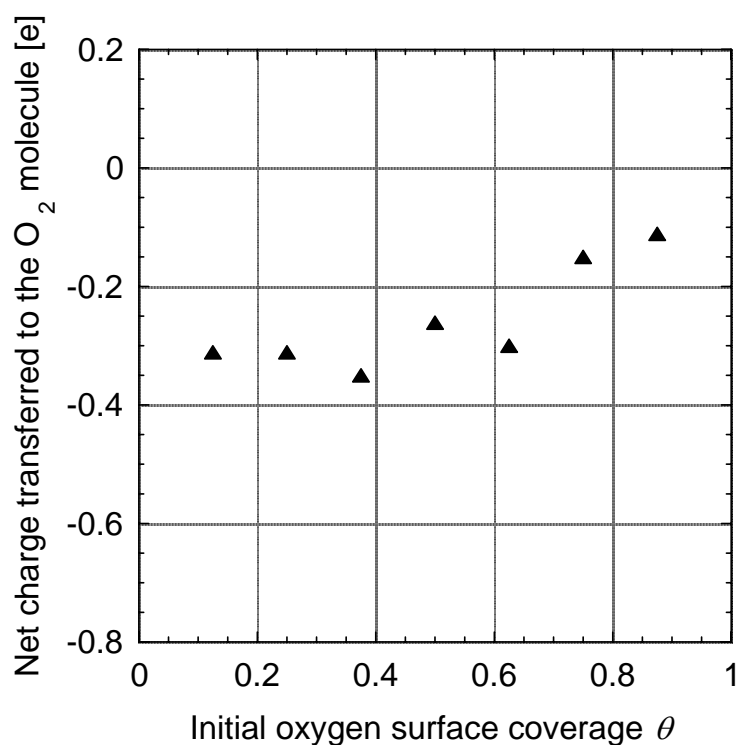


**Fig. 5.3:** Net electron transferred to the oxygen molecule versus coverage.

### 5.3 Molecular Oxygen Decomposition

The dissociation of molecularly adsorbed oxygen was initially analyzed by considering three cases: dissociation of either (1) the side-on geometry adsorbed in the bridge configuration, (2) end-on geometry decomposing from an fcc-threefold site to an hcp-threefold site, or (3) end-on geometry decomposing from an hcp-threefold site to an fcc-threefold site. The obtained activation energies are given in Table 5.3. The calculations show a most favorable (smallest activation energy) decomposition process of the end-on geometry from an fcc-threefold site to an hcp-threefold. This is in agreement with previous theoretical (DFT) studies performed by van Santen [120] as well as with the principle of least atom sharing [121] (after decomposition the surface ad-atoms share the smallest number of surface metal atoms).

	(1)	(2)	(3)
$E_a$ [eV]	0.90	0.40	0.76

**Table 5.3:** Activation energy of O<sub>2</sub> decomposition: (1) side-on in the bridge configuration, (2) end-on geometry decomposing from an fcc-threefold site to an hcp-threefold site, (3) end-on geometry decomposing from an hcp-threefold site to an fcc-threefold site.

Based on these results, the oxygen decomposition from an fcc-threefold to a hcp-threefold site on a surface pre-covered with atomic oxygen was investigated. The calculations have been performed on a (2×4) unit cell with different atomic oxygen coverages. Activation energies and reaction energies of the decomposition process have been determined by locating the transition state on the potential energy surface (PES) between the optimized structures of the oxygen molecule and its decomposition products. (Note that the surface coverages used in the following are calculated as the number of surface sites occupied by oxygen atoms and the oxygen molecule before decomposing divided by total number of platinum surface sites.) Fig. 5.4 shows the optimized geometries of the decomposed O<sub>2</sub> for surface coverages  $\theta = 0.625$  and 0.75.

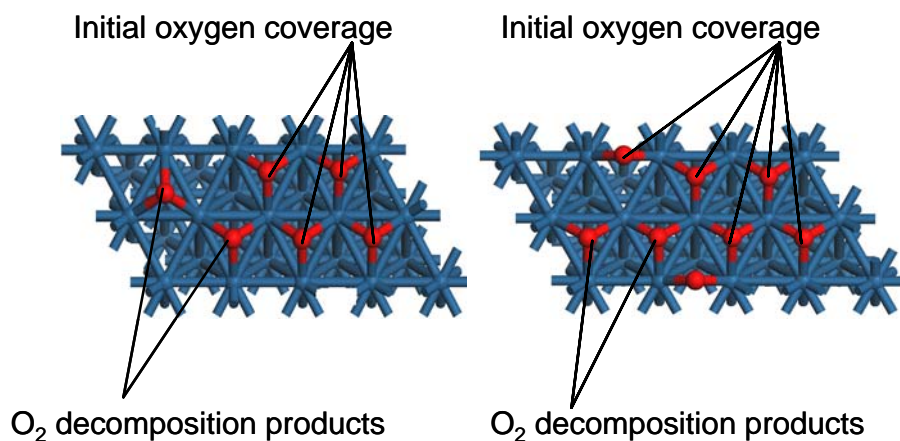


**Fig. 5.4:** Optimized structures of decomposed O<sub>2</sub> on Pt(111) for surface coverages  $\theta = 0.625$  (left panel) and  $0.75$  (right panel).

At surface coverages higher than 0.625 the decompositions process occurs from the fcc three fold site to the next available fcc three fold surface site. This is due to electronic interactions of adsorbed oxygen atoms as well as from an increasing competition for the surface sites (steric effects). The obtained activation energies of O<sub>2</sub> dissociation are plotted versus coverage in Fig. 5.5. The results show an increase of activation barrier as the surface atomic oxygen coverage increases. Activation energies vary from 0.40 eV to 2.67 eV for surface coverages  $\theta = 0.125$  and  $0.875$ , respectively. The calculations indicate that with increasing atomic oxygen preoccupation the decomposition process is inhibited.

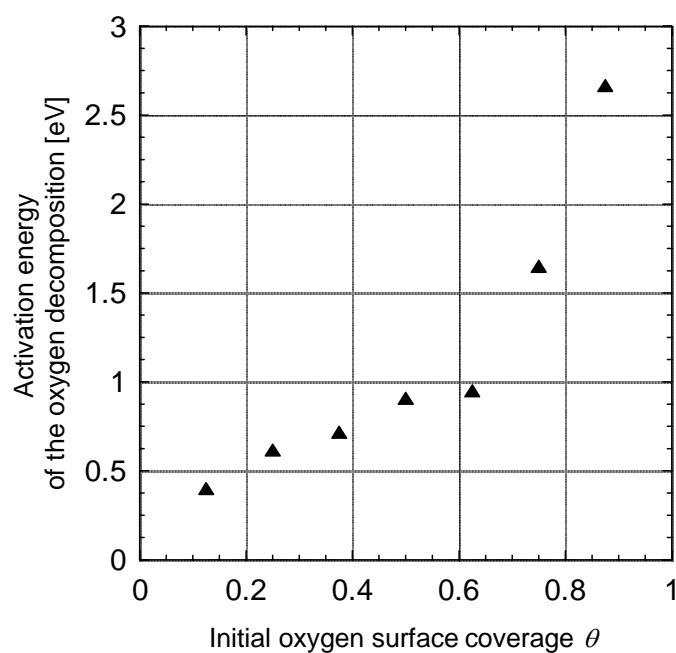


**Fig. 5.5:** Activation energy of the oxygen decomposition dependence on surface coverage.

The influence of surface coverage on reaction energies of oxygen decomposition is shown in Fig. 5.6. The reaction energies decrease with increasing coverage, the decomposition process becoming even endothermic for surface coverages  $\theta > 0.75$ .

In order to further understand the electronic effect between molecular oxygen and the platinum surface a Mulliken charge analysis of the transition states was performed. The net electron transfer from the surface to the decomposing molecule in the transition state is given in Table 5.2. The calculations show an increased net transfer between surface coverages 0.125 and 0.25 from -0.35 to -0.64 while for higher coverages ( $\theta \geq 0.25$ ) there is an almost constant net electron transfer with increasing the coverage. This may arise from an increasing competition between the adsorbed oxygen atoms for the surface charge.

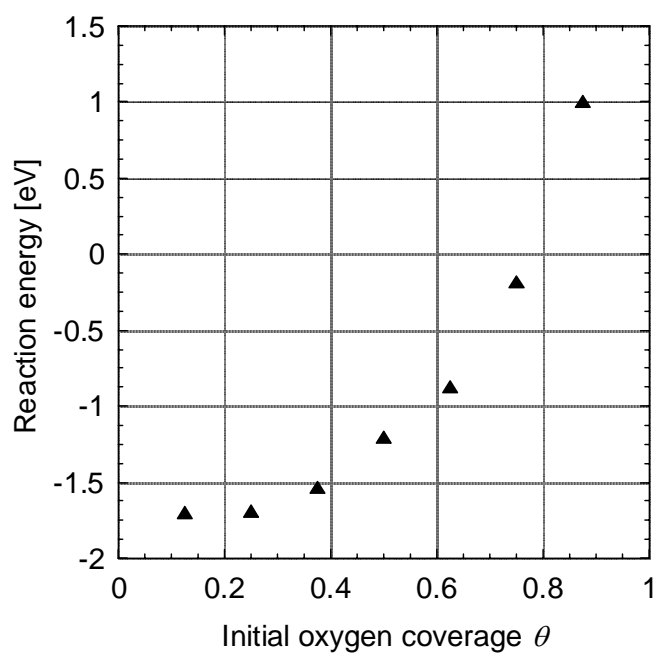


**Fig. 5.6:** Reaction energies dependence on surface coverage.

Fig. 5.7 shows the relationship between activation energies and reaction energies for surface coverage dependence of  $O_2$  dissociation on Pt(111) surface. The behavior is almost linear. This is known as the Brønsted-Evans-Polanyi (BEP) relationship [122]. The existence of such a linear relationship between activation energies and reaction energies has been previously demonstrated for various dissociation reactions [89,123].



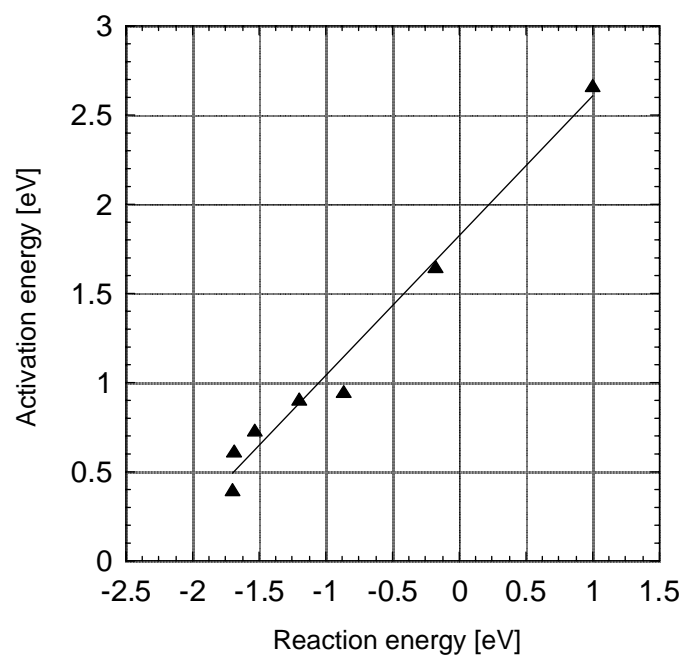


**Fig. 5.7:** Activation energy of the  $O_2$  decomposition dependence on reaction energy (Brønsted-Evans-Polanyi relationship).

#### 5.4 Atomic Oxygen Adsorption on Platinum (111)

Previous [42,91,111,112,115] studies of atomic oxygen interaction with Pt(111) surfaces have found that adsorption takes place in a threefold hollow site and that the fcc site is more stable than the hcp site. The same preference of atomic oxygen adsorption was also observed for a Rh(111) surface [41].

In the present work, the adsorption energies were calculated with respect to the  $O_2$  molecule in the gas phase. The obtained energetic and geometrical parameters are shown in Table 5.4. The calculated adsorption energies for a  $(2 \times 2)$  supercell ( $\theta = 0.25$ ) show, in agreement with previous studies, that the fcc structure ( $E_{\text{ads}} = -1.81$  eV) is more stable than the hcp structure ( $E_{\text{ads}} = -1.36$  eV). The optimized geometry of atomic oxygen in the fcc threefold site has a distance of 122 pm above the surface and a metal-oxygen distance of 205 pm. The adsorption in the threefold hcp hollow site shows slightly longer distances above the surface ( $d(\text{O-surface}) = 126$  pm) and from the platinum atom ( $d(\text{Pt-O}) = 207$  pm). The obtained

geometrical parameters are in good agreement with previous *ab-initio* calculations [42,111,115].

Atomic oxygen	fcc threefold site	hcp threefold site
$E_{\text{ads}}$ [eV]	-1.81	-1.36
$d(\text{O-surface})$ [pm]	122.4	126.5
$d(\text{O-Pt})$ [pm]	$a = 205.0$ $b = 204.5$ $c = 204.5$	$a = 207.7$ $b = 206.9$ $c = 206.9$

**Table 5.4:** Energetic and geometrical parameters of two configurations of the atomic oxygen adsorbed on Pt(111) surface in a (2×2) supercell. a, b, c are the distances of the oxygen atom to the three closest Pt atoms.

The influence of surface coverage on atomic oxygen adsorption on Pt(111) was studied for coverages  $\theta = 0.125, 0.25$  and  $0.5$ . Geometric, energetic and charge-transfer values of these structures are given in Table 5.5, and the adsorption energies are plotted versus coverage in Fig. 5.8. The calculations show that the adsorption energy slightly decreases with increasing coverage. The results are in good agreement with previously reported values. A strong interaction of atomic oxygen with Pt(111) has also been observed by Gland [91] with adsorption energies varying from  $-1.65$  eV to  $-5.18$  eV for coverages of  $0.8$  and  $0.02$  respectively. For a surface coverage  $\theta = 0.5$ , Eichler *et al.* [111] calculated adsorption energies of  $-0.98$  and  $-1.65$  eV for the hcp and fcc structure, respectively.

Surface coverage	O adsorption, fcc site			O diffusion, fcc-hcp sites		
	$E_{\text{ads}}$ [eV]	$d(\text{O-surface})$ [pm]	$d(\text{O-Pt}^{a,b,c})$ [pm]	$E_a$ [eV]	$\Delta H$ [eV]	Partial charge of O atom in the transition state [e]
$\theta = 0.125$	-1.77	122.4	$a = b = 204$ $c = 205$	0.59	0.41	-0.46
$\theta = 0.25$	-1.81	122.4	$a = 204.5$ $b = 204.5$ $c = 205$	0.63	0.45	-0.46
$\theta = 0.5$	-1.55	120.5	$a = 204.6$ $b = 204.5$ $c = 201.6$	0.66	0.48	-0.44

**Table 5.5:** Energetic and geometrical parameters of atomic oxygen adsorbed on Pt(111) surface in an fcc threefold site at different surface coverages.  $a$ ,  $b$ ,  $c$ , are the distances of the oxygen atom to the three closest Pt atoms.

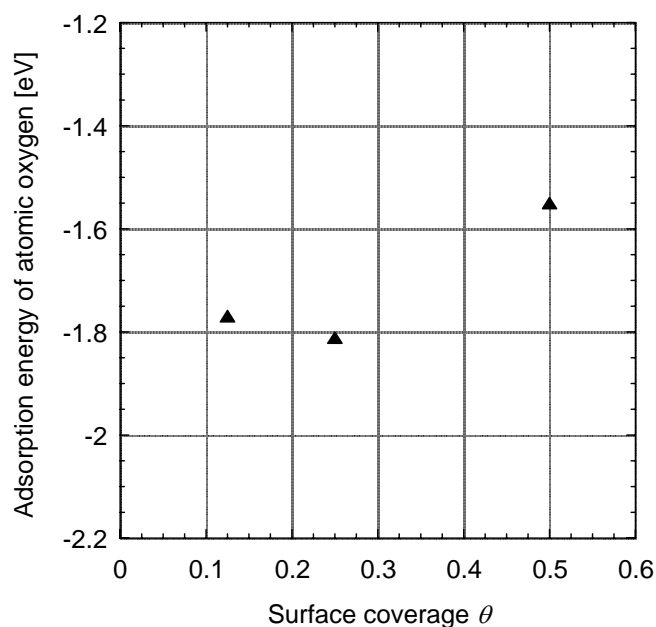


**Fig. 5.8:** Adsorption energies of atomic oxygen versus surface coverage.

## 5.5 Surface Diffusion of Atomic Oxygen

In order to have a more detailed insight into the atomic oxygen behavior on Pt(111), diffusion on the surface from an fcc hollow site to a hcp site was studied. Transition states located on potential energy surfaces were calculated for coverages  $\theta = 0.125$ , 0.25 and 0.5. The optimized geometries of the reactant, transition state and the product of the diffusion process for  $\theta = 0.25$  are shown in Fig. 5.9. The optimized structure of the transition state is located in the bridged position between the fcc and hcp threefold sites.

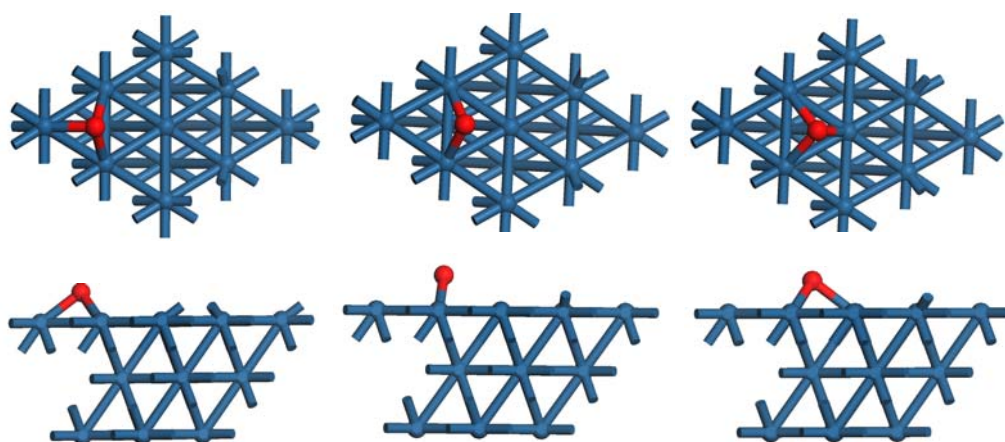


**Fig. 5.9:** Atomic oxygen diffusion from an fcc-threefold position to an adjacent hcp-threefold position and the corresponding transition state.

The dependence of the calculated activation energies on surface coverages is displayed in Fig. 5.10. The results show an increase of the activation energy with increasing coverage. Results of a Mulliken charge analysis show a decrease of the net electron transferred from the platinum surface to the oxygen atom in the transition state with increasing surface coverage from 0.46 e to 0.44 e at coverages  $\theta = 0.125$  and  $\theta = 0.5$ , respectively. The calculated oxygen diffusion barrier is in good agreement with previous STM measurements (0.43 eV) [124] and DFT calculations (0.58 eV) [125].

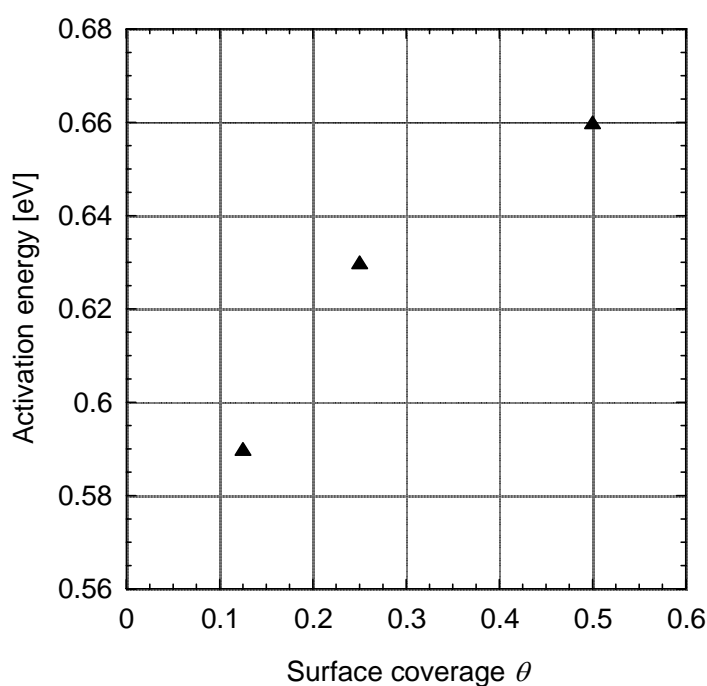


**Fig. 5.10:** Activation energy of the atomic oxygen diffusion as a function of surface coverage.

## 5.6 Influence of Coadsorbates on the Surface Diffusion of Atomic Oxygen

The atomic oxygen diffusion between fcc and hcp threefold sites was furthermore investigated in the presence of different atomic species as coadsorbates. As coadsorbates H, N, Cl and F atoms were considered. The calculations were performed on a (2×2) unit cell. The atomic coordinates of the adsorbates were fully mobile for optimization while the platinum atoms of the periodic slab were constrained. The obtained kinetic parameters (activation energies and reaction energies) of atomic oxygen diffusion in the presence of coadsorbates are given in Table 5.6.

The dependence of the calculated activation energies on coadsorbate electronegativity is shown in Fig. 5.11. The results show a decrease of the activation energy with increasing coadsorbate electronegativity. The higher the coadsorbate electronegativity is, the lower is the diffusion barrier. This effect is likely due to the electron withdrawing by the electronegative coadsorbate from the metal surface, lowering the activation barrier of the diffusion process of the oxygen atom. The back-diffusion (energy barrier of the product) process of atomic oxygen

is also shown in Fig. 5.11. The energy barrier of the product is increasing with increasing electronegativity. Plotting the reaction energies versus coadsorbates's electronegativity, a linear relationship (Fig. 5.12) was observed. The fcc-hcp diffusion process is endothermic for low electronegativities while for values above three the process becomes exothermic. The Brönsted-Evans-Polanyi (BEP) relationship is observed also for the diffusion process. The linear relationship between the activation energies and reaction energies of atomic oxygen diffusion is shown in Fig. 5.13.

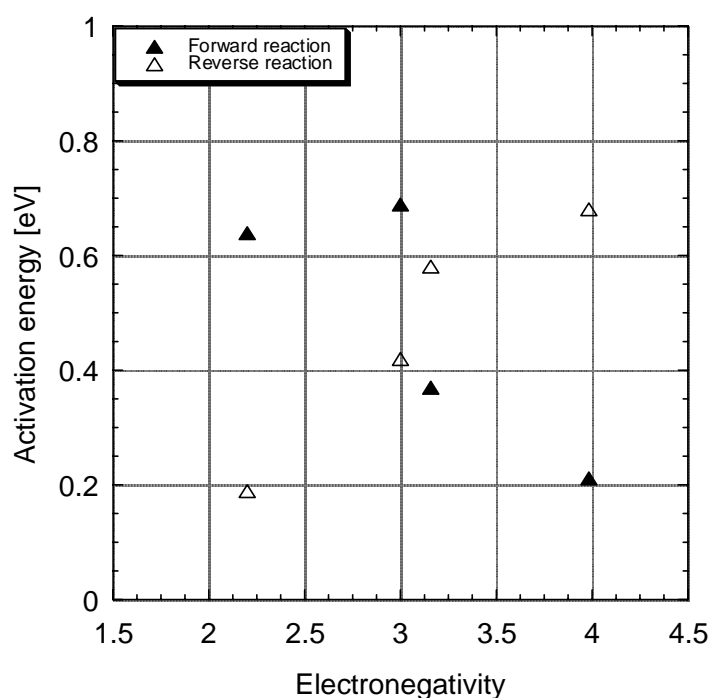


**Fig. 5.11:** Activation energies of atomic oxygen diffusion as a function of coadsorbate electronegativity.

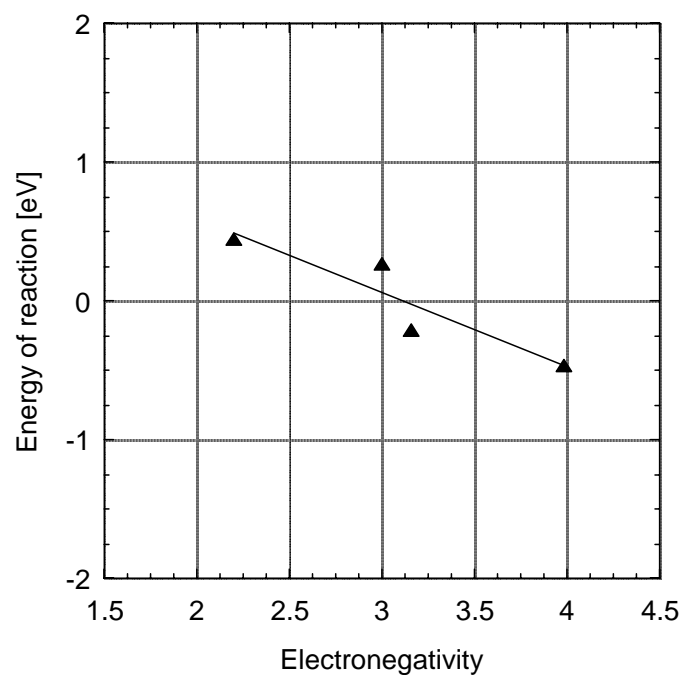


**Fig. 5.12:** Reaction energies of atomic oxygen diffusion as a function of coadsorbate electronegativity.

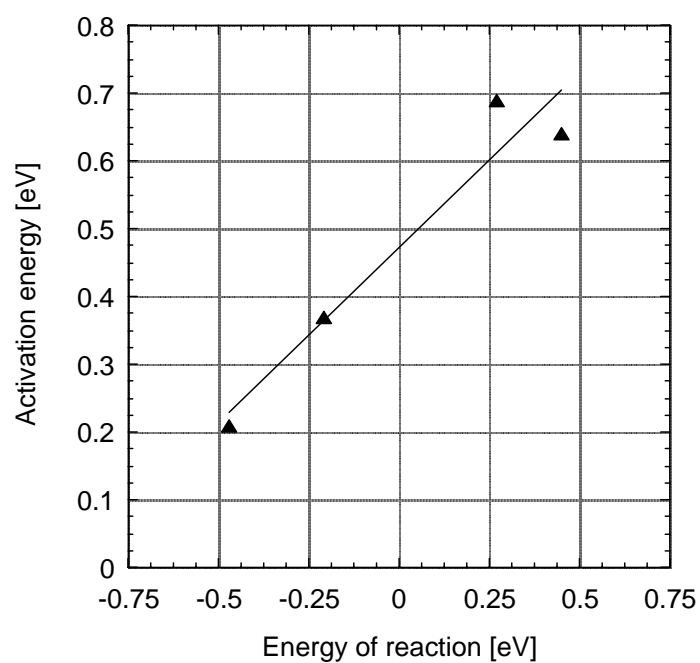


**Fig. 5.13:** Activation energy of atomic oxygen diffusion dependence on reaction energy (Brønsted-Evans-Polanyi relationship).

O adsorption			O diffusion, fcc-hcp sites			
Coadsorbate	Electronegativity	$E_{\text{ads}}$ [eV]	$E_{\text{a}}$ [eV]	Energy barrier of the product	$\Delta H$ [eV]	Mulliken charge of oxygen atom in transition state
H	2.2	-1.54	0.64	0.19	+0.45	-0.46
N	3.0	-1.00	0.69	0.42	+0.27	-0.46
Cl	3.16	-0.96	0.37	0.58	-0.21	-0.43
F	3.98	-1.4	0.21	0.68	-0.47	-0.43

**Table 5.6:** Calculated kinetic parameters of oxygen diffusion on Pt(111) in the presence of different coadsorbates.

## 5.7 Conclusions

In the present work density-functional theory (DFT) calculations were performed to determine thermodynamic and kinetic parameters of reactions of oxygen on a Pt(111) surface and their dependence on surface coverage. Three processes were investigated that play a role in the functionality of Pt-based oxidation catalyst: (1) the adsorption of molecular oxygen, (2) the dissociation into atomic oxygen, and (3) the surface diffusion of atomic oxygen. The main results are summarized as follows.

In all cases, the energies of adsorption, activation, and reaction depend on the surface coverage. This dependence is particularly strong for the activation barrier of molecular oxygen dissociation, and weak for the adsorption of molecular and atomic oxygen as well as for surface diffusion. A higher surface coverage generally reduces or even inhibits the reactivity of the various processes.

Upon adsorption of molecular oxygen, the side-on geometry was observed more stable than end-on configurations. For atomic oxygen, adsorption in the fcc site is favored over the hcp site.

The diffusion barrier between fcc and hcp sites was observed to depend not only on surface coverage, but also on the nature of coadsorbates present on the surface.



For both, the dissociation of molecular oxygen, and the surface diffusion of atomic oxygen, linear Brønsted-Evans-Polanyi relationships were observed between the reaction energies and the activation energies.

The results contribute to a better understanding of the reactivity of platinum surfaces towards oxygen. In particular, the obtained data on coverage dependence will help to improve kinetic simulations of oxidation catalysts.



## Chapter 6: Simulations of Surface Coverages and Transport Processes

### 6.1 Thermodynamic Simulation of the BaO Surface Coverage

The calculations presented in Chapter 4 show that NO, NO<sub>2</sub>, CO<sub>2</sub> and H<sub>2</sub>O all have negative adsorption energies, i.e., they form stable adsorbates on a BaO(100) surface. The adsorption energies are, however, very different, and they furthermore strongly depend on surface coverage. These findings make it likely that carbon dioxide and water, both present as majority species in engine exhaust gases, adsorb on BaO in competition to the minority species NO and NO<sub>2</sub>. They may thus play an important role in the NO<sub>x</sub> storage mechanism, if not as chemically active species, then at least by blocking available surface sites.

In order to study the effects of the competitive adsorption of the four gas-phase species in a more quantitative way, in the following a computational analysis of the surface concentrations for a realistic exhaust gas composition was performed. The model system consists of a total of ten species: NO (gas), NO<sub>2</sub> (gas), CO<sub>2</sub> (gas), H<sub>2</sub>O (gas), NO(ads, O-site), NO<sub>2</sub>(ads, O-site), NO<sub>2</sub>(ads, Ba-site), CO<sub>2</sub> (ads, carbonate-type), H<sub>2</sub>O (ads), and free BaO surface sites, that can undergo a total of five adsorption/desorption reactions. The adsorption/desorption equilibrium for each single surface species is given by

$$K = \theta_{\text{adsorbate}} / \left( p_{\text{gas-phase}} / p^0 \theta_{\text{BaO}} \right) = \exp(-\Delta G_{\text{R}}(\theta_{\text{adsorbate}}) / RT), \quad (6.1)$$

where  $K$  is the equilibrium constant,  $T$  is the temperature,  $p_{\text{gas-phase}}$  is the gas-phase partial pressure,  $p^0 = 101325$  Pa,  $\theta_{\text{BaO}}$  is the fraction of free barium oxide surface sites,  $\Delta G_{\text{R}}$  is the free enthalpy of the reaction, and  $R$  is the universal gas constant.

Each of the five investigated adsorption/desorption reactions is described by one equation of Type (6.1). The surface coverages are calculated by solving these equations under the boundary condition that the total surface coverage must not exceed unity. In order to use the DFT results for evaluating Eq. (6.1) the following assumptions were made:

(1) No surface species can exceed a coverage of unity. Here, the free ( $\text{Ba}_{\text{surf}} + \text{O}_{\text{surf}}$ ) adsorption site pairs are respectively treated as one single species. This is a reasonable assumption as the investigated molecules are considerably bigger than a single surface site (cf. Figs. 4.1, 4.4, 4.7 and 4.14, Chapter 4). Thus, each of the surface species in fact occupies a total of two surface sites (one  $\text{Ba}_{\text{surf}}$  and one  $\text{O}_{\text{surf}}$  site). The boundary condition for the total coverage is then

$$\theta_{\text{NO-O(surf)}} + \theta_{\text{NO}_2\text{-O(surf)}} + \theta_{\text{NO}_2\text{-Ba(surf)}} + \theta_{\text{CO}_2\text{-ads}} + \theta_{\text{H}_2\text{O-ads}} + \theta_{\text{BaO}} = 0.5 \quad (6.2)$$

(2) The free enthalpy  $\Delta G_{\text{R}}$  can be obtained from the reaction enthalpy  $\Delta H_{\text{R}}$  and the reaction entropy  $\Delta S_{\text{R}}$  according to

$$\Delta G_{\text{R}}(T) = \Delta H_{\text{R}}(T) - T \Delta S_{\text{R}}(T) \quad (6.3)$$

It is strongly temperature dependent. The DFT results presented in the previous chapters, however, correspond to  $\Delta H_{\text{R}}(T = 0 \text{ K})$  only. In order to obtain the free enthalpy at realistic temperatures, a correction for the entropies are necessary (cf. [69,126]). This property is not known for the surface species in this study. Still, a simple approach based on kinetic theory allows to estimate the entropy of an adsorption/desorption reaction, when reasonable assumptions of the sticking coefficient and the desorption attempt frequency are made (see Appendix A). For the following calculations, is therefore assumed

$$\Delta G_{\text{R}}(T) = F E_{\text{ads,DFT}} - T \Delta_{\text{R}} S^{\text{estimated}}(T) \quad , \quad (6.4)$$

where  $F$  is Faraday's constant needed for the unit conversion of eV to kJ/mol. The calculation of  $\Delta_{\text{R}} S^{\text{estimated}}(T)$  is given in the appendix A; it is negative by around 80J/kmol - 100 J/kmol.

(3) The adsorption energies are assumed to depend on the coverage of the respective adsorbate only. Coadsorption effects such as energy gain through pair formation are

neglected. The coverage dependence was described using a linear relationship. The parameters obtained by linear regression were presented in detail in Subchapter 4.7.

These assumptions represent considerable simplifications. They nevertheless allow calculating the thermodynamic surface state versus temperature based on the results obtained from the DFT calculations. They thus enable a qualitative discussion of the species' competitive adsorption based on first principles. The complete mathematical description consists of a set of six coupled equations (five equations of Type (1) and Equation (2)). They are solved numerically for a range of temperatures using a Newton algorithm.

Calculation results are shown in Fig. 6.1 for assumed gas-phase concentrations corresponding to typical lean engine operating conditions (250 ppm NO, 250 ppm NO<sub>2</sub>, 7% CO<sub>2</sub>, 10% H<sub>2</sub>O). Over a large temperature range relevant to exhaust gas catalysis, the BaO surface is almost completely covered (total surface coverage  $\geq 99\%$  for temperatures  $\leq 900$  K). The main surface species are the carbonate-type CO<sub>2</sub> and H<sub>2</sub>O, while the NO<sub>x</sub> species have considerably lower coverages, in particular at elevated temperatures. With increasing temperature, the fraction of free BaO sites keeps increasing due to the increasing importance of the negative adsorption entropies.

Fig. 6.2 shows similar calculations where CO<sub>2</sub> and H<sub>2</sub>O are assumed to be absent. This corresponds to conditions studied before experimentally [58,127-129]. Over a wide range of temperatures, the surface is now completely covered with nitrogen oxide species (total surface coverage  $\geq 90\%$  for temperatures  $\leq 700$  K).

An important conclusion from these calculations is that the relatively large stability of involved species (CO<sub>2</sub>, H<sub>2</sub>O, NO, NO<sub>2</sub>:  $E_{\text{ads}} < -0.7$  eV) causes an almost complete (>99%) coverage of the surface at temperatures relevant for exhaust gas catalysis. As the thermodynamic surface state is the setting under which storage kinetics must take place, this needs to be taken into account when considering mechanistic aspects of NO<sub>x</sub> storage:

(1) Reactions between two surface-attached species (e.g. the disproportionation reaction  $2 \text{NO}_2(\text{ads}) \rightarrow \text{NO}(\text{ads}) + \text{NO}_3(\text{ads})$  as proposed by Broqvist *et al.* [66]) are more likely than simple surface dissociation reactions that require the presence of free surface sites (e.g.  $\text{NO}_2(\text{ads}) + \text{free site} \rightarrow \text{NO}(\text{ads}) + \text{O}(\text{ads})$ ). Pair formation effects, as, e.g., studied by Schneider and Broqvist *et al.* [66,67], are likely to play an important role.

(2) NO<sub>x</sub> storage may be kinetically controlled through the availability of free surface sites for adsorption of reactants.

(3) For further mechanistic studies, quantum chemical calculations should be performed in the limit of highly covered surfaces. Periodic-slab calculations using isolated molecules on large supercells (e.g., the large supercells of Schneider [67] and Broqvist [69]) or cluster calculations do not seem to represent realistic conditions.

(4) The observation of high coverages of carbonate-type adsorbates supports the possibility of barium carbonate (instead of barium oxide) being the active storage species under realistic gas-phase compositions.

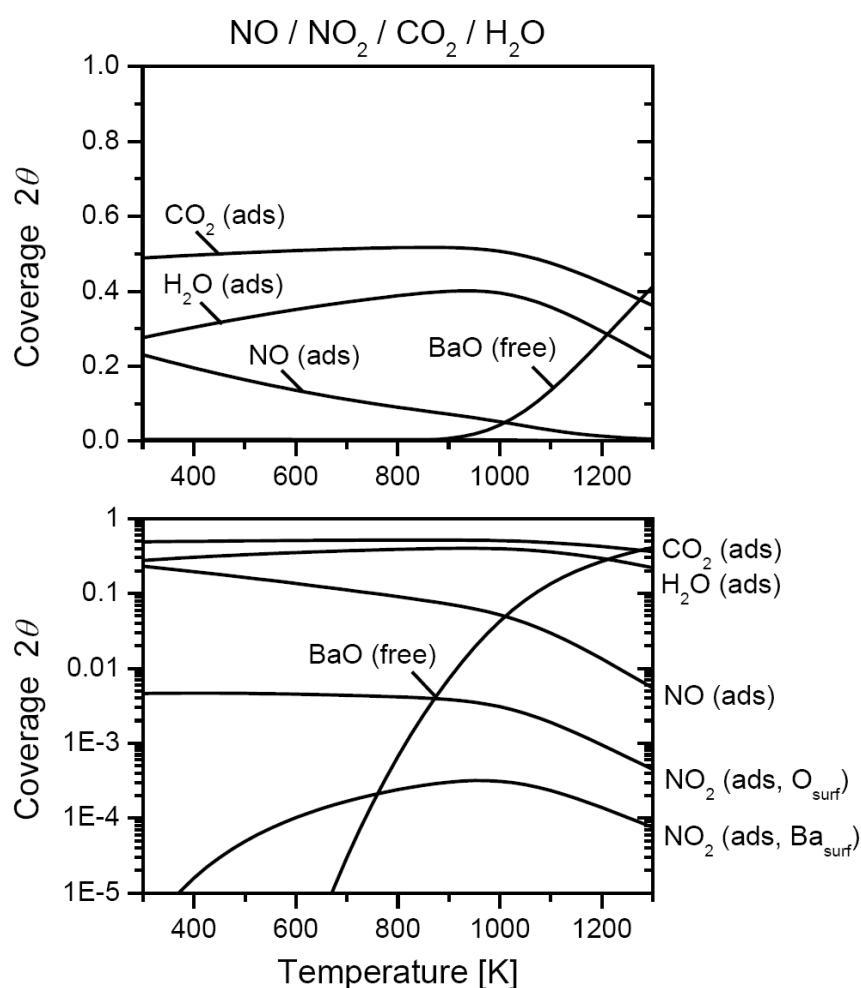


**Fig. 6.1:** Equilibrium surface coverages for the ten-species system (four gas-phase species  $\text{NO}$ ,  $\text{NO}_2$ ,  $\text{CO}_2$  and  $\text{H}_2\text{O}$ , five adsorbate species as given in Table 5 plus free  $\text{BaO}$  surface sites) simulated for a typical lean engine exhaust gas (250 ppm  $\text{NO}$ , 250 ppm  $\text{NO}_2$ , 7%  $\text{CO}_2$ , 10%  $\text{H}_2\text{O}$ ) versus temperature. Both panels show the same data on different scales. The coverage is given in units of  $2\theta$  because each species is assumed to occupy one ( $\text{BaO}$ ) surface pair.

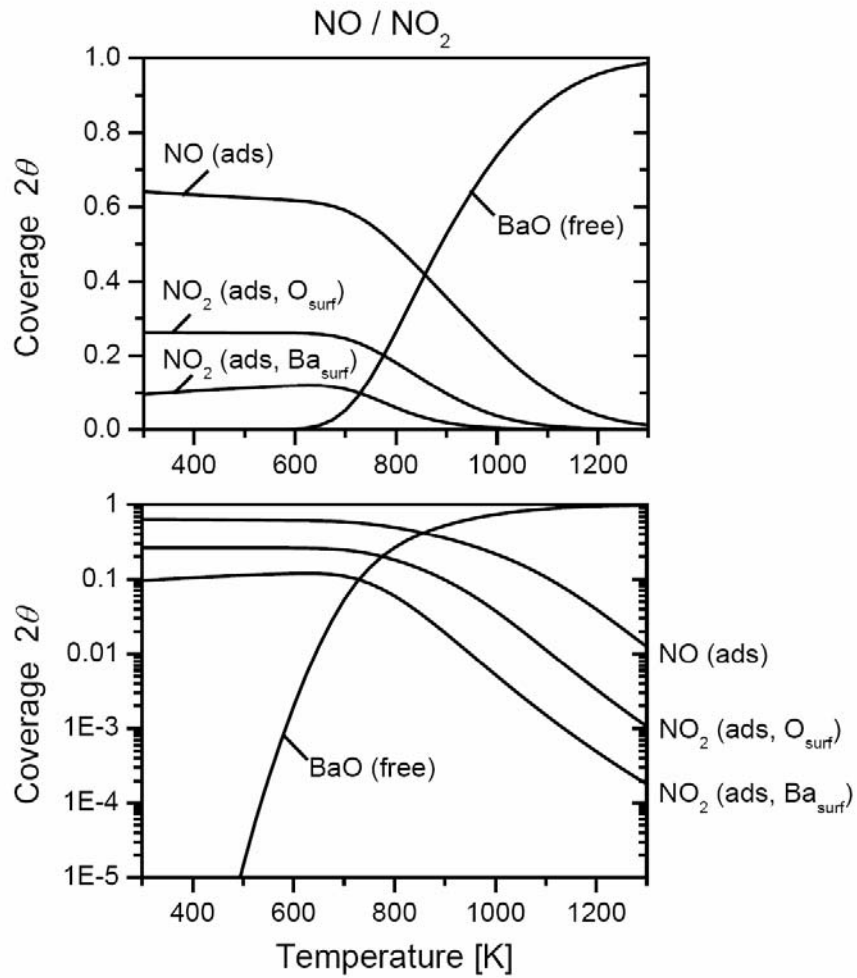


**Fig. 6.2:** Equilibrium surface coverages for the ten-species system for a gas atmosphere without carbon dioxide and water (250 ppm NO, 250 ppm NO<sub>2</sub>) versus temperature. Both panels show the same data on different scales. The coverage is given in units of  $2\theta$  because each species is assumed to occupy one (BaO) surface pair

### 6.1.1 Conclusions

Numerical thermodynamic calculations of the competitive adsorption/desorption equilibria of the four gas-phase species under realistic engine exhaust gas conditions show that the surface is almost completely covered with carbon dioxide and water over a wide range of temperatures. The results indicate that these species play an essential role in the surface processes during NO<sub>x</sub> storage on BaO, where they can block a large part of available surface sites. This finding also supports the possibility of barium carbonate being the active storage species under realistic gas-phase compositions.

## 6.2 Kinetic Simulation of Oxygen Reaction and Surface Spillover Processes on Platinum

### 6.2.1 Background

The NO<sub>x</sub> storage and reduction (NSR) concept has been developed as a consequence to the need to decrease pollutant emissions as well as fuel consumption from internal combustion engines. As mentioned in Chapter 1, the NO<sub>x</sub> storage and reduction mechanism can be divided into four steps:

1. NO oxidation to NO<sub>2</sub> on Pt surface,
2. NO<sub>2</sub> storage on BaO surface,
3. regeneration of the storage component,
4. NO<sub>x</sub> reduction to N<sub>2</sub>.

Few studies for kinetic modeling of NO<sub>x</sub> storage in catalysts used in lean-burn engines can be found in the literature [51,52,63,130-132]. The most detailed kinetic model of the mechanism of nitrogen oxides (NO<sub>x</sub>) storage was performed by Olsson *et al.* [51], investigating the following subsystems: oxygen adsorption/desorption on Pt/Al<sub>2</sub>O<sub>3</sub>, NO oxidation on Pt/Al<sub>2</sub>O<sub>3</sub>, NO oxidation on Pt/BaO/Al<sub>2</sub>O<sub>3</sub>/ and the NO<sub>x</sub> storage on BaO/Al<sub>2</sub>O<sub>3</sub>.



The kinetic modeling of NO<sub>x</sub> storage mechanism is a complex process involving reactions on the Pt surface, reactions on the BaO surface and reactions on both Pt and BaO surfaces. The kinetic model proposed by Olsson *et al.* [51] is summarized in the following:

1. The reactions steps for NO oxidation to NO<sub>2</sub> (reactions involving Pt sites) may proceed through the following elementary steps:

- Oxygen adsorption/desorption on Pt,



- NO adsorption on Pt,

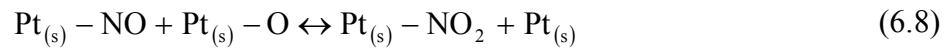


- NO<sub>2</sub> adsorption on Pt,

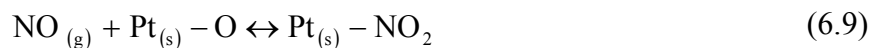


- To describe NO oxidation, three different models were analyzed:

a) a Langmuir-Hinshelwood (LH) model,



b) an Eley-Rideal (ER) model,

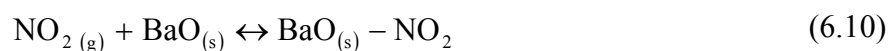


c) a combined LH-ER model, where both Reactions 6.8 and 6.9 were used.

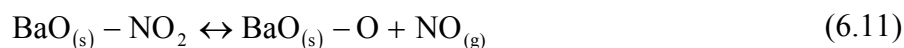
The Langmuir-Hinshelwood (LH) mechanism was concluded to be the most probable for NO oxidation.

2. The NO<sub>x</sub> storage on BaO (reactions involving BaO surface) was described by the following elementary reaction steps:

- NO<sub>2</sub> adsorption on BaO,



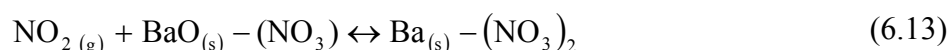
- Surface oxidation (peroxide formation),



- NO<sub>2</sub> oxidation to nitrate formation,



- Barium nitrate formation,



- Oxygen formation,



### 3. Spillover between Pt and BaO surfaces (reaction involving both Pt and BaO surfaces)

- The NO<sub>2</sub> spillover reaction from Pt sites to the BaO sites to form barium nitrate,



The NO<sub>x</sub> storage mechanism involves a variety of surface nitrogen-oxygen species, possibly competing reaction pathways and a strong competition with CO<sub>2</sub> and H<sub>2</sub>O. The spillover reaction plays an essential role in the NO<sub>x</sub> storage mechanism [64]:

- It couples the two surfaces (Pt and BaO),
- it is potentially faster than the gas-phase transport,
- it has been postulated to be at the origin of metal-support interactions [133,134].

#### 6.2.2 Simulation of Pt(111) Surface Reaction, Diffusion and Spillover

In order to better understand the properties of the spillover reaction as well as its coupling with surface transport (diffusion), in the following the model system Pt/YSZ was studied. The system is chosen for two reasons:

1. Oxygen spillover can be induced electrochemically (i.e., by applying a voltage between Pt and YSZ) and therefore be well controlled.
2. There are detailed experimental studies by Luerßen *et al.* [135] that can be used for model validation.

Therefore, in the present work, a kinetic model of oxygen surface reactions, atomic diffusion and oxygen spillover on platinum/YSZ system (YSZ = yttria-stabilized zirconia) is presented. The study allows a detailed insight into the oxygen surface reaction mechanism on platinum. In this section, literature values for kinetic parameters are used. In the next section (6.2.3) the DFT results obtained in Chapter 5 will be applied.

The present kinetic simulations, were performed using the DENIS [136,137] package developed by Bessler and co-workers. DENIS simulates the kinetics of complex electrochemical systems from detailed models of elementary reactions and transport processes using the DETCHEM [138] chemistry library.

In order to verify if the DENIS package can simulate oxygen surface reaction mechanisms applied in NSR catalysis, a comparative study between a model based on elementary steps and measurements [135] of O spillover mechanism on Pt/YSZ system was performed.

The experimental measurements performed by Luerßen *et al.* [135] report the oxygen spillover mechanism as follows: Upon applying an electrochemical potential between the Pt and YSZ surfaces, oxygen ions are transported through the YSZ bulk to the YSZ surface. Atomic oxygen is generated at the three-phase boundary (tpb), spills over and then diffuses on the platinum surface forming a layer of chemisorbed oxygen. The three-phase boundary is given by the boundary between the YSZ surface, the gas-phase and the platinum surface.

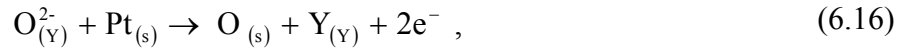
The starting point of this study was to use the simplest possible model of oxygen surface reactions on platinum applied in TWC catalysis developed by Deutschmann *et al.* [139]. This chemistry model is based on elementary reaction steps of oxygen adsorption/desorption on platinum. The kinetic parameters of the model are shown in Table 6.1.

	$A$ [mol, cm, s]	$\beta$ -	$E_a$ [kJ/mol]
1. Adsorption			
Stick			
$O_{2(g)} + Pt_{(s)} + Pt_{(s)} \rightarrow O_{(s)} + O_{(s)}$	$2.3 \times 10^{-02}$	0	0
2. Desorption			
$O_{(s)} + O_{(s)} \rightarrow Pt_{(s)} + Pt_{(s)} + O_{2(g)}$	$3.7 \times 10^{+21}$	0	213
$\$O_{(s)}$	0	0	60

**Table 6.1:**  $O_2$  mechanism on Pt developed by Deutschmann *et al.* [139].

Note:  $A$  [mol, cm, s] is the pre-exponential factor,  $\beta$  is the temperature exponent,  $E_a$  [kJ/mol] is the activation energy. Stick denotes the reaction is defined using a sticking coefficient;  $Pt_{(s)}$  denotes a free adsorption site of the platinum surface;  $O_{(s)}$  denotes atomic oxygen adsorbed on a platinum surface site;  $\$$  denotes that the corresponding reaction takes into account the coverage dependence of the kinetic parameters.

To this model a spillover step of oxygen from the YSZ surface to the Pt surface was included according to



where  $O_{(Y)}^{2-}$  denotes double negatively charged oxygen atom on the YSZ surface,  $Pt_{(s)}$  denotes a free adsorption site of the platinum surface,  $O_{(s)}$  denote atomic oxygen adsorbed on a platinum surface site,  $Y_{(Y)}$  denotes the yttria-stabilized zirconia surface sites.

In the present study, transient simulations reflecting the experiments shown in [135] were performed: At a time  $t = 0$ , a voltage is applied. Spillover, diffusion and reactions on the Pt surface are monitored over time. In the simulations, the voltage is set back to zero after 10 seconds. The total simulated time was 20 seconds. The experimental conditions are given in Table 6.2.

Temperature [K]	670
Pressure [Pa]	$1 \times 10^{-05}$ [135]
Surface diffusion coefficient [ $\text{m}^2/\text{s}$ ]	$9.8 \times 10^{-08}$ [135]
Platinum surface site density [ $\text{mol}/\text{cm}^2$ ]	$2.72 \times 10^{-09}$ [140]
Voltage applied [V]	0.2

**Table 6.2:** Experimental conditions.

The simulated surface coverages at a distance of  $50 \mu\text{m}$  from the tpb versus the time of the simulation performed are shown in Fig. 6.3. The results show that after applying a voltage, the O atoms spill over from the YSZ surface to the Pt surface, diffuse on the surface and reach a steady state. Changing the voltage after 10 seconds to 0 V reestablishes equilibrium.

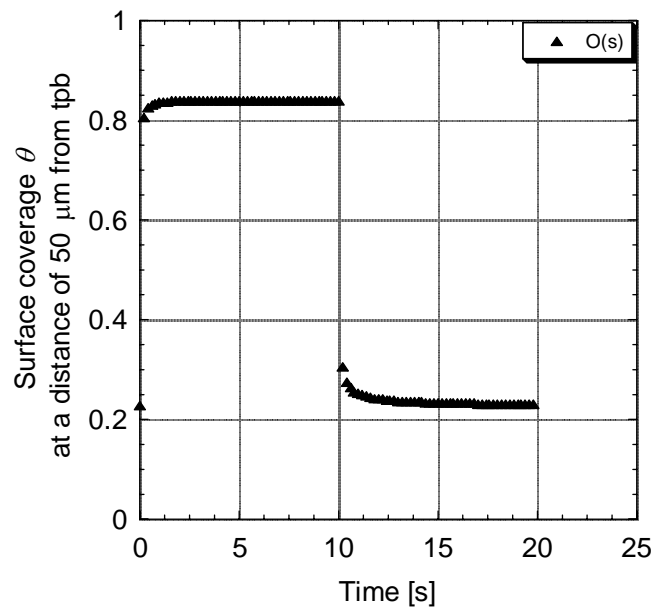


**Fig. 6.3:** Calculated surface coverages at a distance of  $50 \mu\text{m}$  from the tpb of O on platinum as a function of the time.

The simulated surface coverages versus the distance from the three-phase boundary (tpb) at different times are shown in Figs. 6.4 and 6.5. The results show that the surface coverage decreases with increasing distance from the three-phase boundary system (tpb). This is due to

the desorption reaction. In agreement with the experimental observations [135], a front movement of the oxygen surface coverage with time is observed.

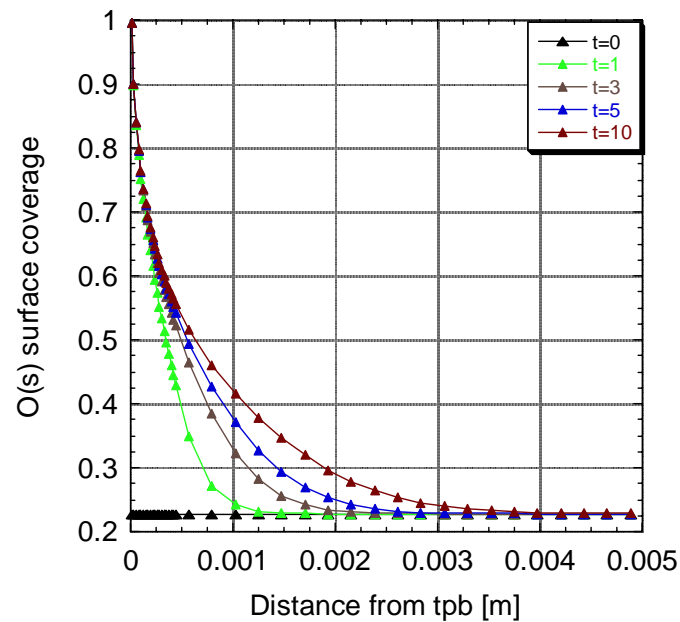


**Fig. 6.4:** O surface coverage as a function of distance from the three-phase boundary (tpb). A voltage is applied at  $t = 0$  s, inducing spillover at the tpb.

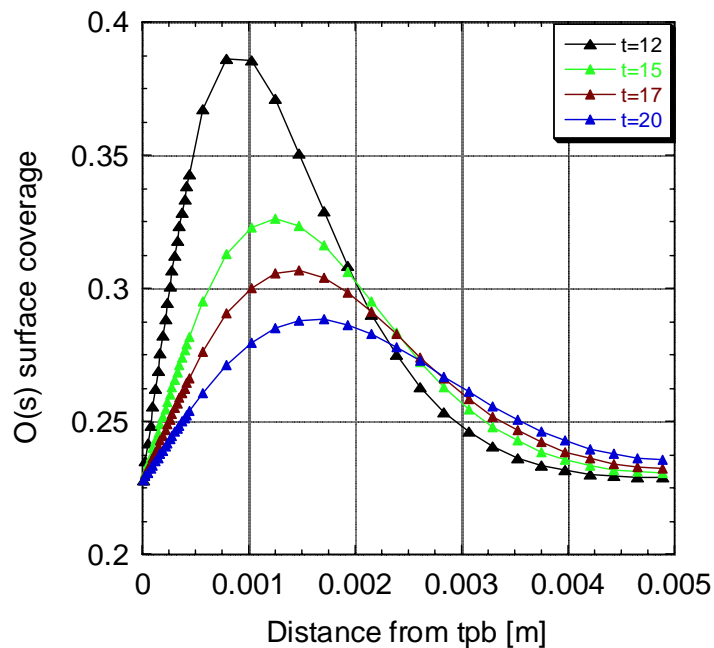


**Fig. 6.5:** O surface coverage as a function of distance from the three-phase boundary (tpb) after the voltage has been set to zero (stopping spillover) at  $t = 10$  s.

Fig. 6.6 shows the electrical current variation with the time of the simulations.

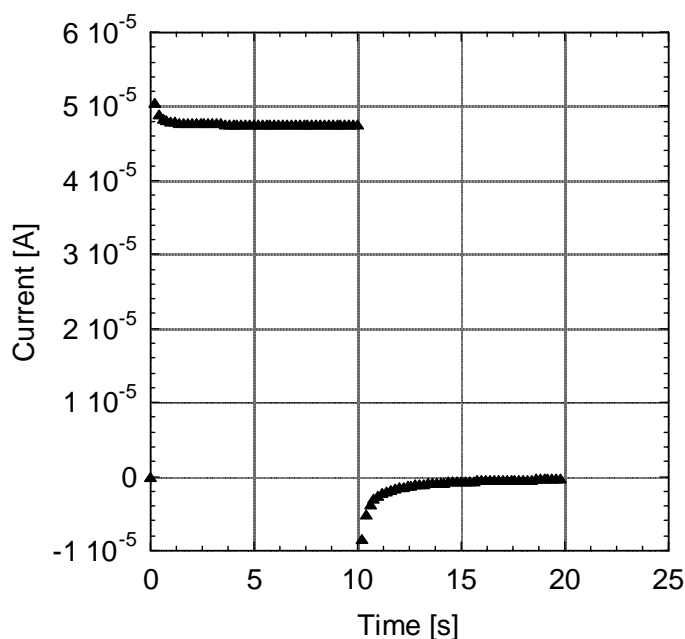


**Fig. 6.6:** Current variation versus time of the simulation.

### 6.2.3 Application of DFT Results

One objective of this thesis was to apply the kinetic parameters (adsorption energies, activation energies and their coverage dependencies) obtained from DFT calculations in kinetic simulations of reaction mechanisms applied in NSR catalysis. Therefore, in the following a kinetic simulation of oxygen reactions on Pt based on DFT results obtained in previous chapter is presented.

The kinetic model considered here is similar to the one described in the previous subchapter. The model consists of oxygen surface reactions, atomic oxygen diffusion and oxygen spillover reaction on YSZ/Pt system.

The oxygen surface reaction model is based on four elementary reactions steps of molecular oxygen adsorption, desorption, dissociation and atomic oxygen recombination. The reactions as well as the kinetic parameters considered are given in Table 6.2.

	$A$ [mol, cm, s]	$\beta$ -	$E_a$ [kJ/mol]
1. O <sub>2</sub> adsorption Stick O <sub>2(g)</sub> + Pt <sub>(s)</sub> → O <sub>2(s)</sub>	$2.3 \times 10^{-02}$	0	0
2. O <sub>2</sub> desorption O <sub>2(s)</sub> → Pt <sub>(s)</sub> + O <sub>2(g)</sub> \$O <sub>(s)</sub>	$1.0 \times 10^{+13}$	0	90.27 15.43
3. O <sub>2</sub> dissociation O <sub>2(s)</sub> + Pt <sub>(s)</sub> → O <sub>(s)</sub> + O <sub>(s)</sub> \$O <sub>(s)</sub>	$3.7 \times 10^{+21}$	0	16.25 -250.84
4. O + O recombination O <sub>(s)</sub> + O <sub>(s)</sub> → O <sub>2(s)</sub> + Pt <sub>(s)</sub> \$O <sub>(s)</sub>	$3.7 \times 10^{+21}$	0	229.62 73.60

**Table 6.2:** O<sub>2</sub> mechanism on Pt based on DFT results obtained in this work.

The coverage dependency for each reaction was considered through a linear dependence according to equation

$$E_{a\text{DFT}} = E_a^0 + \varepsilon * \theta \quad (6.17)$$

where the parameters  $E_a^0 = E_a(\theta=0)$  and  $\varepsilon$  are obtained by linear regression. Their values are given in Table 6.3.

	$E_a^0$ [kJ/mol]	$\varepsilon$ [kJ/mol]
O <sub>2</sub> desorption	90.27	-15.43
O <sub>2</sub> dissociation	16.25	250.84
O + O recombination	229.62	-73.60

**Table 6.3:** Linear fit parameters of the coverage dependence of oxygen reaction on Pt.



The oxygen spillover reaction between the YSZ and Pt surfaces was taken into account according to Eq. (6.16). The simulation conditions are shown in Table 6.4. The surface diffusion coefficient used in the simulation was calculated based on the activation energy of atomic oxygen jump between the fcc and hcp threefold sites of the Pt surface. The calculation is given in appendix B.

Temperature [K]	670
Pressure [Pa]	$1 \times 10^{-05}$ [135]
Surface diffusion coefficient [ $\text{m}^2/\text{s}$ ]	$1.23 \times 10^{-12}$ [this work, see appendix B]
Platinum surface site density [ $\text{mol}/\text{cm}^2$ ]	$2.72 \times 10^{-09}$ [140]
Voltage applied [V]	0.2

**Table 6.4:** Simulation conditions.

The simulations were performed for 20 seconds applying at time  $t = 0$  s a voltage of 0.2 V. The simulated surface coverages at a distance of 0.5  $\mu\text{m}$  from the tpb of atomic and molecular oxygen on the Pt surface versus the time of the simulation are shown in Figs. 6.7 and 6.8, respectively. Applying the electrical potential between the YSZ and Pt surfaces causes O spill over from the YSZ surface to the Pt surface, diffuse on the surface and reach a steady state of  $\theta = 0.8$ . For molecular oxygen a very low surface coverage with a steady state of  $\theta = 3.5 \times 10^{-8}$  is observed.

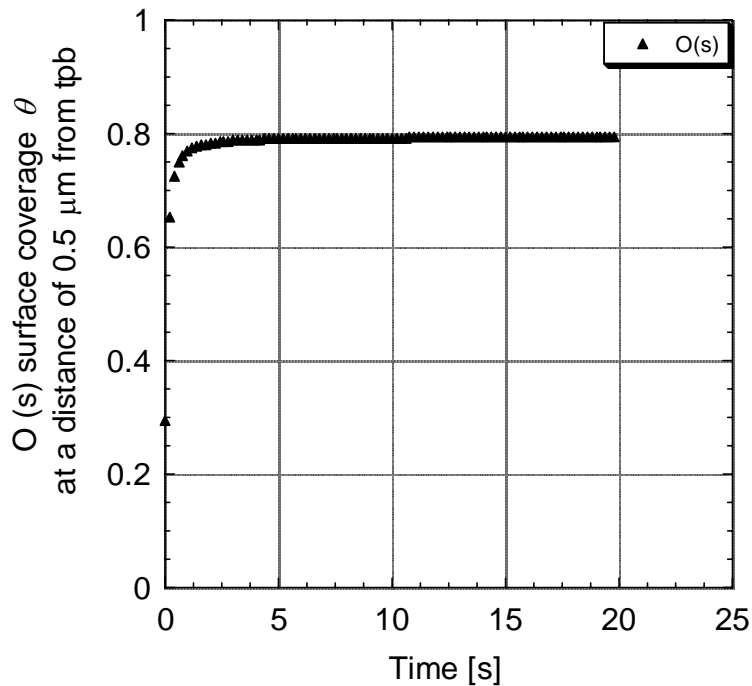


**Fig. 6.7:** Calculated surface coverages at a distance of  $0.5 \mu\text{m}$  from tpb of atomic oxygen on platinum as a function of the time.

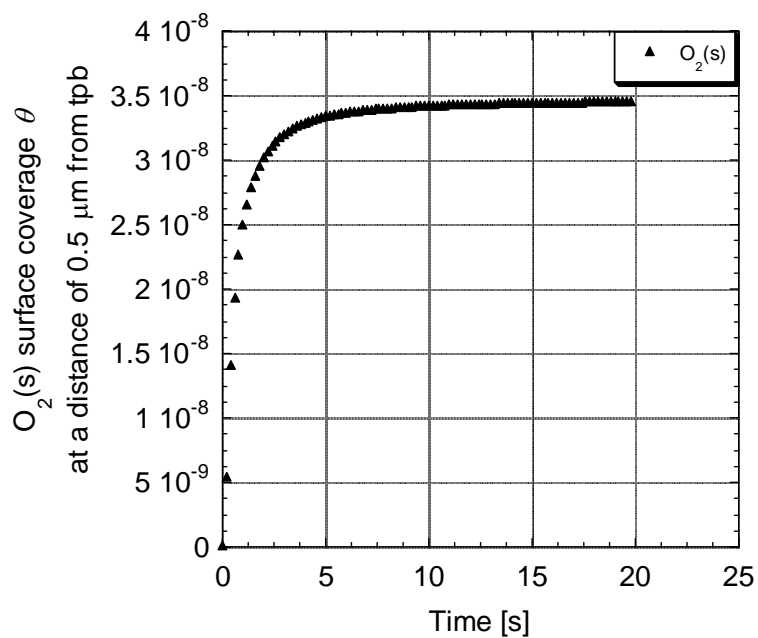


**Fig. 6.8:** Calculated surface coverages at a distance of  $0.5 \mu\text{m}$  from tpb of  $O_2$  on platinum as a function of the time.

The simulated surface coverages of atomic oxygen versus the distance from the three-phase boundary (tpb) at different times is shown in Fig. 6.9. As in the previous subchapter, the study shows that the surface coverage decreases with increasing distance from the three-phase boundary system (tpb) due to the desorption reaction. Again, a front movement of the oxygen surface coverage with time is observed. However, in this model the oxygen concentration is very small due to the smaller surface diffusion coefficients ( $D = 1.23 \times 10^{-12} \text{ m}^2/\text{s}$ ) used in the model.

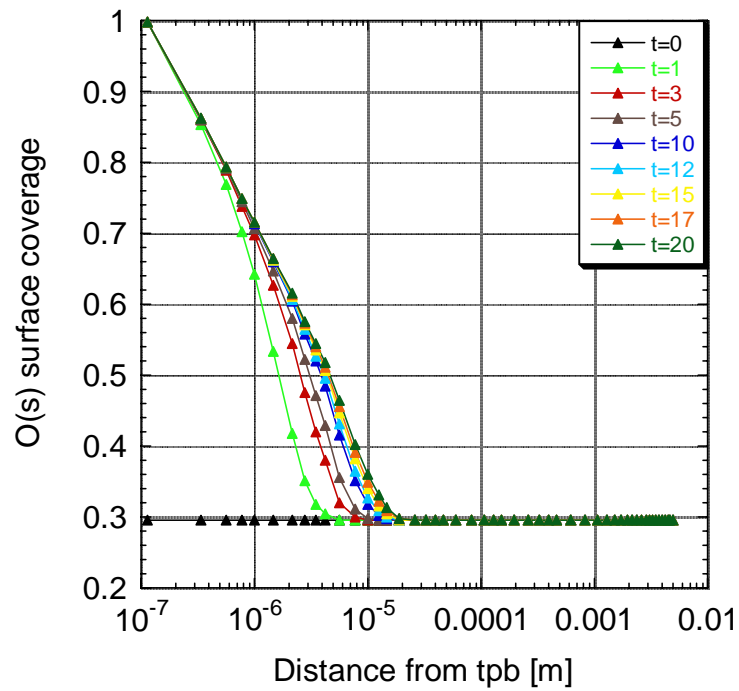


**Fig. 6.9:** O surface coverage as a function of distance from the three-phase boundary (tpb)

Fig. 6.10 shows the electrical current variation with the time of the simulations.

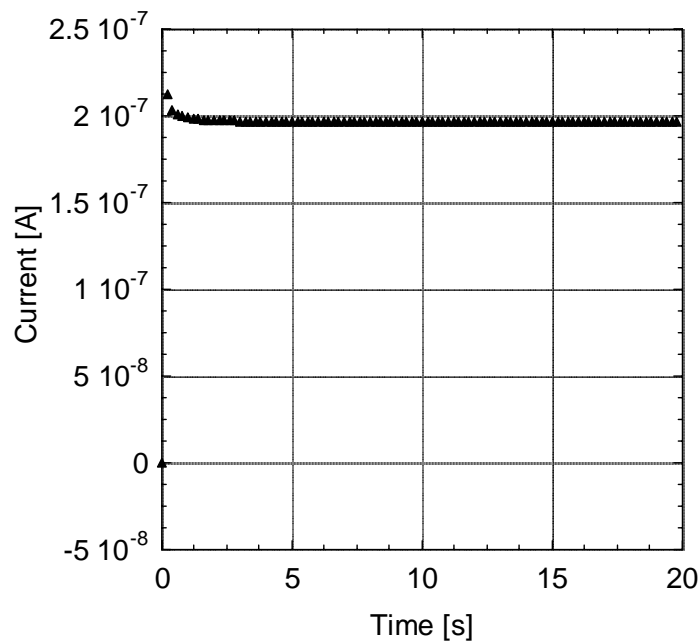


**Fig. 6.10:** Current variation versus time of the simulation.

#### 6.2.4 Conclusions

Kinetic modeling of oxygen surface reactions, atomic diffusion and surface spillover on Pt/YSZ was performed. The reaction model considered four elementary reactions steps of molecular oxygen adsorption, desorption, dissociation and atomic oxygen recombination. The kinetic parameters (activation energies, their coverage dependencies) and diffusion coefficients from the DFT results were applied in the present kinetic simulation.

Oxygen spillover from the YSZ surface to the Pt surface could be induced upon applying an electrical potential between the two surfaces. The results showed that atomic oxygen spills over, diffuses on the Pt surface and reaches a steady state after a few seconds.

A discrepancy with the experimental studies is observed for the surface diffusion process. Due to a larger diffusion coefficient used, the concentration wave extends far onto the surface in the experiments while in the present results the concentration wave does not extend far onto the surface.

## Chapter 7: Summary

The demand for lower pollutant emissions from internal combustion engines as well as for lower fuel consumption has led to the introduction of lean-burn gasoline engines. These engines are operated at higher air-fuel ratios than traditional stoichiometric gasoline engines. Under lean oxidizing conditions the conventional Three-Way Catalysts (TWC) cannot reduce nitrogen oxides ( $\text{NO}_x$ ). In this context a new concept, the so called  $\text{NO}_x$  storage and reduction (NSR) concept, of catalytic converters has been developed. The operation principle is based on periodic alternation of long lean engine-combustion phases with short rich phases. A material with storage potential, i.e., metal oxides ( $\text{BaO}$ ,  $\text{CeO}_2$ ), is included into the catalytic converter and its storage function is combined with mixed operation conditions of the engine. Mechanistic details of this storage process are of vital importance for model simulations and optimization of such storage catalysts.

The aim of this thesis was to obtain a microscopic understanding of the  $\text{NO}_x$  storage reaction mechanism by means of *density functional theory* (DFT). Electronic structure calculations were performed for adsorption of different molecules on two surfaces relevant in automotive exhaust gas purification: barium oxide and platinum. The obtained detailed knowledge by means of quantum mechanical calculations were further applied in kinetic simulations of surface reaction mechanisms relevant for NSR catalysis.

Quantum chemical studies of adsorption on  $\text{BaO}(100)$  surface of four gas-phase species relevant for exhaust gas catalysis were presented. It was found that  $\text{NO}$ ,  $\text{NO}_2$ ,  $\text{CO}_2$  and  $\text{H}_2\text{O}$  adsorption energies strongly depend on surface coverage through electronic effects. Furthermore, it was shown that  $\text{NO}$  adsorbs as stable nitrite-like species,  $\text{NO}_2$  may adsorb in various geometries on both, barium and oxygen surface sites, while  $\text{CO}_2$  forms a carbonate-type structure.  $\text{H}_2\text{O}$  adsorbs strongly on  $\text{BaO}$  surface with adsorption energies in the same range as  $\text{NO}$ ,  $\text{NO}_2$  and  $\text{CO}_2$ .

Similar DFT calculations were performed to determine thermodynamic and kinetic parameters of reactions of oxygen on a Pt(111) surface and their dependence on surface coverage. Three processes were investigated that play a role in the functionality of Pt-based oxidation catalyst: (1) the adsorption of molecular oxygen, (2) the dissociation into atomic oxygen, and (3) the surface diffusion of atomic oxygen. The investigations showed that energies of adsorption, activation, and reaction depend on the surface coverage. It was found that molecular adsorption has a more favorable configuration in the side-on geometry, while for atomic oxygen, adsorption in the fcc site is favored over the hcp site. The diffusion barrier between fcc and hcp sites was observed to depend not only on surface coverage, but also on the nature of coadsorbates present on the surface. For both the dissociation of molecular oxygen and the surface diffusion of atomic oxygen, linear Brønsted-Evans-Polanyi relationships were observed between the reaction energies and the activation energies.

The kinetic data obtained by DFT investigations for the BaO surface were further applied in a thermodynamic study of the competitive adsorption of NO, NO<sub>2</sub>, CO<sub>2</sub> and H<sub>2</sub>O on BaO surface during catalyst operation. Numerical calculations for a typical exhaust gas composition showed that CO<sub>2</sub> plays an essential role in the surface processes during NO<sub>x</sub> storage on BaO.

The DFT results of reactions of oxygen on a Pt(111) surface and their dependence on surface coverage were used in a kinetic model of oxygen surface reactions on platinum. The study contributes to a better understanding of kinetic simulations of oxidation catalysts.

The development of a detailed kinetic model for understanding of an entire catalytic converter under real working conditions is underway. It will allow the investigation of a NSR catalyst behavior based on kinetic data obtained by means of density functional quantum chemical calculations.

To conclude, the results obtained within this thesis provide a detailed insight into the surface processes relevant in NO<sub>x</sub> storage and reduction catalytic converters. They thus represent an important contribution to the development of the NSR catalysts.

---

## References

1. G. C. Koltsakis and A. M. Stamatelos, "Catalytic automotive exhaust aftertreatment," *Progress in Energy and Combustion Science* **23**, 1-39 (1997).
2. C. Depcik and D. Assanis, "One-dimensional automotive catalyst modeling," *Prog. Energy Combust. Sci.* **31**, 308-369 (2005).
3. E.U., *Directive 2002/80/EC*. 3 October 2002.
4. E.U., *Directive 98/69/EC*. 13 October 1998.
5. E.U., *COM(2005) 683*. 21 December 2005.
6. R. M. Heck and R. J. Farrauto, *Catalytic air pollution control* (Van Nostrand Reinhold, New York, 1996).
7. M. Shelef, "Selective catalytic reduction of NO<sub>x</sub> with N-free reductants," *Chem. Rev.* **95**, 209-225 (1995).
8. W. Bögner, M. Krämer, B. Krutzsch, S. Pischinger, D. Voigtländer, G. Wenninger, F. Wirbeleit, M. S. Brogan, R. J. Brisley, and D. E. Webster, "Removal of nitrogen oxides from the exhaust lean-tune gasoline engine," *Appl. Catal. B* **7**, 153-171 (1995).
9. N. Takahashi, H. Shinjoh, T. Iijima, M. Suzuki, K. Yamazaki, K. Yokota, H. Suzuki, N. Miyoshi, S. Matsumoto, T. Tanizawa, T. Tanaka, S. Tateishi, and K. Kasahara, "The new concept 3-way catalysts for automotive lean-burn engine: NO<sub>x</sub> storage and reduction catalyst," *Catal. Today* **27**, 63-69 (1996).
10. N. Miyoshi, S. Matsumoto, K. Katoh, T. Tanaka, and J. Harada, "Development of new concept three-way catalyst for automotive lean-burn engines," *SAE Paper* **950809**, 121-130 (1995).
11. J.-O. Chae, "Non-thermal plasma for diesel exhaust treatment," *J. Electrostatics* **57**, 251-262 (2003).
12. Y. Dan, G. Dengshan, Y. Gang, S. Xianglin, and G. Fan, "An investigation of the treatment of particulate matter from gasoline engine exhaust using non-thermal plasma," *J. of Hazardous Materials* **B127**, 149-155 (2005).
13. I. Orlandini and U. Riedel, "Oxidation of propene and the formation of methyl nitrate in non-thermal plasma discharges," *Catalysis Today* **89**, 83-88 (2004).

14. S. Masuda and H. Nakao, "Control of NO<sub>x</sub> by positive and negative pulsed corona discharges," *IEEE Trans. Ind. Appl.* **26**, 374-383 (1990).
15. K. Takaki, S. Kudo, S. Kato, S. Mukaigawa, and T. Fujwara, "Removal of nitric oxide in flue gases by multipoint to plane dielectric barrier discharge," *IEEE Trans. Plasma Sci.* **27**, 201-209 (1999).
16. S. Allam and M. Abom, "Acoustic modelling and testing of diesel particulate filters," *J. of Sound and Vibration* **288**, 255-273 (2005).
17. S. Kureti, W. Weisweiler, and K. Hizbullah, "Simultaneous conversion of nitrogen oxides and soot into nitrogen and carbon dioxide over iron containing oxide catalysts in diesel exhaust gas," *Appl. Catal. B* **43**, 281-291 (2003).
18. O. Deutschmann, *Interactions between transport and chemistry in catalytic reactors*. 2001, Habilitationsschrift: University of Heidelberg.
19. P. H. Schmitz and R. J. Baird, "NO and NO<sub>2</sub> adsorption on barium oxide: model study of the trapping stage of NO<sub>x</sub> conversion via lean NO<sub>x</sub> traps," *J. Phys. Chem. B* **106**, 4172-4180 (2002).
20. A. Szabo and N. S. Ostlund, *Modern Quantum Chemistry* (McGraw-Hill, New York, 1989).
21. M. Born and J. R. Oppenheimer, "Zur Quantentheorie der Molekeln," *Annalen der Physik* **84**, 457-484 (1927).
22. R. G. Parr and W. Yang, *Density functional theory of atoms and molecules* (Oxford University Press, New York, 1989).
23. P. Hohenberg and W. Kohn, "Inhomogeneous electron gas," *Phys. Rev.* **136**, B864-B871 (1964).
24. W. Kohn and L. J. Sham, "Self-consistent equations including exchange and correlation effects," *Phys. Rev.* **140**, A1133-A1138 (1965).
25. J. P. Perdew and Y. Wang, "Atoms, molecules, solids, and surfaces: applications of the generalized gradient approximation for exchange and correlation," *Phys. Rev.* **45**, 13244-13249 (1992).
26. J. P. Perdew, J. A. Chevary, S. H. Vosko, K. A. Jackson, M. R. Pederson, and C. Fiolhais, "Atoms, molecules, solids, and surfaces: Applications of the generalized



- 
- gradient approximation for exchange and correlation," *Phys. Rev. B* **46**, 6671–6687 (1992).
27. J. P. Perdew, K. Burke, and M. Ernzerhof, "Generalized gradient approximation made simple," *Phys. Rev. Lett.* **77**, 3865-3868 (1996).
28. B. Hammer, L. B. Hansen, and J. K. Norskov, "Improved adsorption energetics within density-functional theory using revised Perdew-Burke-Ernzerhof functionals," *Phys. Rev. B* **59**, 7413-7421 (1999).
29. M. D. Segall, P. J. D. Lindan, M. J. Probert, C. J. Pickard, P. J. Hasnip, S. J. Clark, and M. C. Payne, "First-principles simulation: ideas, illustrations and the CASTEP code," *J. Phys. Condens. Matter* **14**, 2717-2744 (2002).
30. M. D. Segall, R. Shah, C. J. Pickard, and M. C. Payne, "Population analysis of plane wave electronic structure calculations of bulk materials," *Phys. Rev. B* **54**, 16317 (1996).
31. N. Govind, M. Petersen, G. Fitzgerald, D. King-Smith, and J. Andzelm, "A generalized synchronous transit method for transition state location," *Comp. Mater. Sci.* **28**, 250-258 (2003).
32. N. W. Ashcroft and N. D. Mermin, *Solid state physics* (Saunders College, Fort Worth, 1976).
33. M. C. Payne, M. P. Teter, D. C. Allan, T. A. Arias, and J. D. Joannopoulos, "Iterative minimization techniques for ab-initio total-energy calculations: molecular dynamics and conjugate gradients," *Rev. Mod. Phys.* **64**, 1045-1097 (1992).
34. D. Vanderbilt, "Soft self-consistent pseudopotentials in a generalized eigenvalue formalism," *Phys. Rev. B* **41**, 7892–7895 (1990).
35. D. J. Chadi and M. L. Cohen, "Special points in the Brillouin zone," *Phys. Rev. B* **8**, 5747-5753 (1973).
36. H. J. Monkhorst and J. D. Pack, "Special points for Brillouin-zone integrations-a reply," *Phys. Rev. B* **13**, 5188-5192 (1976).
37. J. D. Pack and H. J. Monkhorst, "Special points for Brillouine-zone integrations," *Phys. Rev. B* **16**, 1748-1749 (1977).

38. R. S. Mulliken, "Electronic population analysis on LCAO-MO molecular wave functions. IV. Bonding and antibonding in LCAO and valence-bond theories," *J. Chem. Phys.* **23**, 2343-2346 (1955).
39. H. Grönbeck, "First principles studies of metal-oxide surfaces," *Topics in Catalysis* **28**, 59-59 (2004).
40. Q. Ge, R. Kose, and D. A. King, "Adsorption energetics and bonding from femtomole calorimetry and from first principles theory," *Advances in Catalysis* **45**, 207-259 (2000).
41. O. R. Inderwildi, D. Lebiez, O. Deutschmann, and J. Warnatz, "Coverage dependence of oxygen decomposition and surface diffusion on Rhodium (111): a DFT study," *J. Chem. Phys.* **122**, 034710 (2005).
42. M. Lynch and P. Hu, "A density functional theory study of CO and atomic oxygen chemisorption on Pt(111)," *Surf. Sci.* **458**, 1-14 (2000).
43. A. W. Edith Chan, R. Hoffmann, and W. Hot, "Theoretical aspects of photoinitiated chemisorption, dissociation, and desorption of O<sub>2</sub> on Pt(111)," *Langmuir* **8**, 1111-1119 (1992).
44. R. Burch, P. J. Millington, and A. P. Walker, "Mechanism of the selective reduction of nitrogen monoxide on platinum-based catalysts in the presence of excess oxygen," *Appl. Catal. B* **4**, 65-94 (1994).
45. O. R. Inderwildi, D. Lebiez, O. Deutschmann, and J. Warnatz, "Influence of initial oxygen coverage and magnetic moment on the NO decomposition on Rhodium (111)," *J. Chem. Phys.* **122**, 154702 (2005).
46. N. Materer, U. Starke, A. Barbieri, R. Döll, K. Heinz, M. A. Van Hove, and G. A. Somorjai, "Reliability of detailed LEED structural analyses: Pt(111) and Pt(112)-p(2x2)-O," *Surf. Sci.* **325**, 207-222 (1995).
47. A. H. Eichler, J., "Molecular precursors in the dissociative adsorption of O<sub>2</sub> on Pt(111)," *Phys. Rev. Lett.* **79**, 4481 - 4484 (1997).
48. R. M. Heck and R. J. Farrauto, "Automobile exhaust catalysts," *Appl. Catal. A* **221**, 443-457 (2001).

49. C. Sedlmair, K. Seshan, A. Jentys, and J. A. Lercher, "Elementary steps of NO<sub>x</sub> adsorption and surface reaction on a commercial storage-reduction catalyst," *J. Catal.* **214**, 308-316 (2003).
50. E. Fridell, H. Persson, B. Westerberg, L. Olsson, and M. Skoglundh, "The mechanism for NO<sub>x</sub> storage," *Catal. Lett.* **66**, 71-74 (2000).
51. L. Olsson, H. Persson, E. Fridell, M. Skoglundh, and B. Andersson, "A kinetic study of NO oxidation and NO<sub>x</sub> storage on Pt/Al<sub>2</sub>O<sub>3</sub> and Pt/BaO/Al<sub>2</sub>O<sub>3</sub>," *J. Phys. Chem. B* **105**, 6895-6906 (2001).
52. U. Tuttlies, V. Schmeißer, and G. Eigenberger, "A new simulation model for NO<sub>x</sub> storage catalyst dynamics," *Topics in Catalysis* **30/31**, 187-192 (2004).
53. F. Rodrigues, L. Juste, C. Potvin, J. F. Tempère, G. Blanchard, and G. Djéga-Mariadassou, "NO<sub>x</sub> storage on barium-containing three-way catalyst in the presence of CO<sub>2</sub>," *Catal. Lett.* **72**, 59-64 (2001).
54. L. Lietti, P. Forzatti, I. Nova, and E. Tronconi, "NO<sub>x</sub> storage reduction over Pt-Ba/-γ-Al<sub>2</sub>O<sub>3</sub> catalyst," *Journal of Catalysis* **204**, 175-191 (2001).
55. I. Nova, L. Castoldi, L. Lietti, E. Tronconi, and P. Forzatti, "On the dynamic behavior of "NO<sub>x</sub>-storage/reduction" Pt-Ba/Al<sub>2</sub>O<sub>3</sub> catalyst," *Catal. Today* **75**, 431-437 (2002).
56. W. S. Epling, L. E. Campbel, A. Yezerets, N. W. Currier, and J. E. Parks, "Overview of the fundamental reactions and degradation mechanism of NO<sub>x</sub> storage/reduction catalysts," *Catalysis Reviews* **46**, 163-245 (2004).
57. H. Mahzoul, J. F. Brilhac, and P. Gilot, "Experimental and mechanistic study of NO<sub>x</sub> adsorption over NO<sub>x</sub> trap catalysts," *Appl. Catal. B* **20**, 47-55 (1999).
58. F. Prinetto, G. Ghiotti, I. Nova, L. Lietti, E. Tronconi, and P. Forzatti, "FT-IR and TPD investigations of the NO<sub>x</sub> storage properties of BaO/Al<sub>2</sub>O<sub>3</sub> and Pt-BaO/Al<sub>2</sub>O<sub>3</sub> catalysts," *J. Phys. Chem. B* **105**, 12732-12745 (2001).
59. X. Li, M. Meng, P. Lin, Y. Fu, T. Hu, Y. Xie, and J. Zhang, "A study on the properties and mechanisms for NO<sub>x</sub> storage over Pt/BaAl<sub>2</sub>O<sub>4</sub>-Al<sub>2</sub>O<sub>3</sub> catalyst," *Topics in Catalysis* **22**, 111-115 (2003).
60. T. Kobayashi, T. Yamada, and K. Kayano, "Study of NO<sub>x</sub> trap reaction by thermodynamic calculation," *SAE Technical Paper* **970745**, 63-72 (1997).

61. N. Cant and M. J. Patterson, "The storage of nitrogen oxides on alumina-supported barium oxide," *Catalysis Today* **73**, 271-278 (2002).
62. E. Fridell, M. Skoglundh, B. Westerberg, S. Johansson, and G. Smedler, "NO<sub>x</sub> storage in barium-containing catalysts," *Journal of Catalysis* **183**, 196-209 (1999).
63. L. Olsson, E. Fridell, M. Skoglundh, and B. Anderson, "Mean-field modelling of NO<sub>x</sub> storage on Pt/BaO/Al<sub>2</sub>O<sub>3</sub>," *Catalysis Today* **73**, 263-270 (2002).
64. A. Paterson, D. Rosenberg, and J. Anderson, "Possible role of spillover processes in the operation of NO<sub>x</sub> storage and reduction catalysts," *Stud. Surf. Sci. Catal.* **138**, 429-436 (2001).
65. I. Nova, L. Castoldi, L. Lietti, E. Tronconi, P. Forzatti, F. Prinetto, and G. Ghiotti, "NO<sub>x</sub> adsorption study over Pt–Ba/alumina catalysts: FT-IR and pulse experiments," *Journal of Catalysis* **222**, 377-388 (2004).
66. P. Broqvist, I. Panas, E. Fridell, and H. Persson, "NO<sub>x</sub> storage on BaO(100) surface from first principles: a two channel scenario," *J. Phys. Chem. B* **106**, 137-145 (2002).
67. W. F. Schneider, "Qualitative differences in the adsorption chemistry of acidic (CO<sub>2</sub>, SO<sub>x</sub>) and amphiphilic (NO<sub>x</sub>) species on the alkaline earth oxides," *J. Phys. Chem. B* **108**, 273-282 (2004).
68. P. Broqvist, I. Panas, and H. Grönbeck, "Toward a realistic description of NO<sub>x</sub> storage in BaO: the aspect of BaCO<sub>3</sub>," *J. Phys. Chem. B* **109**, 9613-9621 (2005).
69. P. Broqvist, I. Panas, and H. Grönbeck, "The nature of NO<sub>x</sub> species on BaO(100): an ab initio molecular dynamics study," *J. Phys. Chem. B* **109**, 15410-15416 (2005).
70. P. Broqvist, H. Grönbeck, E. Fridell, and I. Panas, "Characterization of NO<sub>x</sub> species adsorbed on BaO: experiment and theory," *J. Phys. Chem. B* **108**, 3523-3530 (2004).
71. E. J. Karlsen, M. A. Nygren, and L. G. M. Pettersson, "Comparative study on structures and energetics of NO<sub>x</sub>, SO<sub>x</sub>, and CO<sub>x</sub> adsorption on alkaline-earth-metal oxides," *J. Phys. Chem. B* **107**, 7795-7802 (2003).
72. M. M. Branda, C. Di Valentin, and G. Pacchioni, "NO and NO<sub>2</sub> adsorption on terrace, step, and corner sites of the BaO surface from DFT calculations," *J. Phys. Chem. B* **108**, 4752-4758 (2004).
73. A. F. Holleman and E. Wiberg, *Lehrbuch der Anorganischen Chemie*, ed. N. Wiberg. Vol. 101 (Walter de Gruyter, Berlin, New York, 1995, 507).

- 
74. F. S. Galasso, *Structure and Properties of Inorganic Solids* (Pergamon Press, Oxford, 1970).
  75. B. Westerberg and E. Fridell, "A transient FTIR study of species formed during NO<sub>x</sub> storage in the Pt/BaO/Al<sub>2</sub>O<sub>3</sub> system," *Journal of Molecular Catalysis A: Chemical* **165**, 249-263 (2001).
  76. L. F. Liotta, A. Macaluso, G. E. Arena, M. Livi, G. Centi, and G. Deganello, "A study of the behaviour of Pt supported on CeO<sub>2</sub>-ZrO<sub>2</sub>/Al<sub>2</sub>O<sub>3</sub>-BaO as NO<sub>x</sub> storage-reduction catalyst for the treatment of lean burn engine emissions," *Catalysis Today* **75**, 439-449 (2002).
  77. F. Prinetto, G. Ghiotti, I. Nova, L. Castodli, L. Lietti, E. Tronconi, and P. Forzatti, "In situ FT-IR and reactivity study of NO<sub>x</sub> storage over Pt-Ba/Al<sub>2</sub>O<sub>3</sub> catalysts," *Phys. Chem. Chem. Phys.* **5**, 4428-4434 (2003).
  78. M. Hilgendorff, "NO<sub>x</sub> abatement by catalytic traps: on the mechanism of NO<sub>x</sub> trapping under automotive conditions," *Topics in Catalysis* **30/31**, 155-159 (2004).
  79. T. Toops, D. B. Smith, W. E. Epling, J. E. Parks, and W. S. Partridge, "Quantified NO<sub>x</sub> adsorption on Pt/K/gamma-Al<sub>2</sub>O<sub>3</sub> and the effects of CO<sub>2</sub> and H<sub>2</sub>O," *Appl. Catal. B* **58**, 255-264 (2005).
  80. W. S. Epling, G. Campbell, and J. Parks, "The effects of CO<sub>2</sub> and H<sub>2</sub>O on the NO<sub>x</sub> destruction performance of a model NO<sub>x</sub> storage/reduction catalyst," *Catal. Lett* **90**, 45-56 (2003).
  81. S. Hodjati, P. Bernhardt, C. Petit, V. Pitchon, and A. Kiennemann, "Removal of NO<sub>x</sub>: Part I. Sorption/desorption processes on barium aluminate," *Appl. Catal. B* **19**, 209-219 (1998).
  82. J. Nowotny and L. Dufour, eds. *Surface and near-surface chemistry of oxide materials* (Elsevier, Amsterdam-Oxford-New York-Tokyo, 1988).
  83. Y. Yu, Q. Guo, S. Liu, and E. Wang, "Partial dissociation of water on a MgO(100) film," *Phys. Rev. B* **68**, 115414 (2003).
  84. C. A. Scamehorn, N. M. Harrison, and M. I. McCarthy, "Water chemistry on surface defect sites: chemidissociation versus physisorption on MgO(001)," *J. Chem. Phys.* **101**, 1547-1554 (1994).

85. M. Odelius, "Mixed molecular and dissociative water adsorption on MgO(100)," *Phys. Rev. Lett.* **82**, 3919-3922 (1999).
86. V. A. Tikhomirov and K. Jug, "MSINDO study of water adsorption on the clean MgO(100) surface," *J. Phys. Chem. B* **104**, 7619-7622 (2000).
87. L. Giordano, J. Goniakowski, and J. Suzanne, "Partial dissociation of water molecules in the (3x2) water monolayer deposited on the MgO(100) surface," *Phys. Rev. Lett.* **81**, 1271-1273 (1998).
88. J.-H. Cho, J. M. Park, and K. S. Kim, "Influence of intermolecular hydrogen bonding on water dissociation at the MgO(001) surface," *Phys. Rev. B* **62**, 9981-9984 (2000).
89. O. Inderwildi, D. Lebiecz, and J. Warnatz, "Linear relationship between activation energies and reaction energies for coverage-dependent dissociation reactions on rhodium surfaces," *Phys. Chem. Chem. Phys.* **7**, 1-2 (2005).
90. J. L. Gland, "Molecular and atomic adsorption of oxygen on the Pt(111) and Pt(S)-12(111) x (111) surfaces," *Surf. Sci.* **93**, 487-514 (1980).
91. J. L. Gland, A. S. Brett, and G. B. Fisher, "Oxygen interactions with the Pt(111) surface," *Surf. Sci.* **95**, 587-602 (1980).
92. C. T. Campbell, G. Ertl, H. Kuipers, and J. Segner, "A molecular beam study of the adsorption and desorption of oxygen from a Pt(111) surface," *Surf. Sci.* **107**, 220-236 (1981).
93. H. Steininger, S. Lehwald, and H. Ibach, "Adsorption of oxygen on Pt(111)," *Surf. Sci.* **123**, 1-17 (1982).
94. D. A. S. Outka, J.; Jark, W.; Stevens, P.; Solomon, J.; Madix, R. J., "Orientation and bond length of molecular oxygen on Ag(110) and Pt(111): a near-edge X-ray-absorption fine-structure study," *Phys. Rev. B* **35**, 4119-4122 (1978).
95. N. R. Avery, "An EELS and TDS study of molecular oxygen desorption and decomposition on Pt(111)," *Chem. Phys. Lett.* **96**, 371-373 (1983).
96. G. N. Derry and P. N. Ross, "High coverage states of oxygen adsorbed on Pt(100) and Pt(111) surfaces," *Surf. Sci.* **140**, 165-180 (1984).
97. W. Wurth, J. Stöhr, P. Feulner, X. Pan, K. R. Bauchspiess, Y. Baba, E. Hudel, G. Rucker, and D. Menzel, "Bonding, structure, and magnetism of physisorbed and chemisorbed O<sub>2</sub> on Pt(111)," *Phys. Rev. Lett.* **65** (1990).

- 
98. C. Puglia, A. Nilsson, B. Hernniis, O. Karis, P. Bennich, and N. Martensson, "Physisorbed, chemisorbed and dissociated O<sub>2</sub> on Pt(111) studied by different core level spectroscopy methods," *Surf. Sci.* **342**, 119-133 (1995).
  99. C. E. Wartnaby, A. Stuck, Y. Y. Yeo, and D. A. King, "Microcalorimetric heats of adsorption for CO, NO, and Oxygen on Pt(110)," *J. Phys. Chem.* **100**, 12483-12488 (1996).
  100. B. C. Stipe, M. A. Rezaei, W. Ho, S. Gao, M. Persson, and a. B. I. Lundqvist, "Single-molecule dissociation by tunneling electrons," *Phys. Rev. Lett.* **78**, 4410 - 4413 (1997).
  101. P. D. Nolan, B. R. Lutz, P. L. Tanaka, J. E. Davis, and C. B. Mullins, "Translational energy selection of molecular precursors to oxygen adsorption on Pt(111)," *Phys. Rev. Lett.* **81**, 3179 - 3182 (1998).
  102. P. D. Nolan, B. R. Lutz, P. L. Tanaka, J. E. Davis, and C. B. Mullins, "Molecularly chemisorbed intermediates to oxygen adsorption on Pt(111): A molecular beam and electron energy-loss spectroscopy study," *J. Chem. Phys.* **111**, 3696 - 3704 (1999).
  103. C. R. Parkinson, M. Walker, and C. F. McConville, "Reaction of atomic oxygen with a Pt(111) surface: chemical and structural determination using XPS; CAICISS and LEED," *Surf. Sci.* **545**, 19-33 (2003).
  104. K. Gustafsson and S. Andersson, "Infrared spectroscopy of physisorbed and chemisorbed O<sub>2</sub> on Pt(111)," *J. Chem. Phys.* **120**, 7750 - 7754 (2004).
  105. D. H. Brennan, D. O.; Trapnell, B. M. W., "The calorimetric determination of the heats of adsorption of oxygen on evaporated metal films," *Proc. Roy. Soc. A* **256**, 81-105 (1960).
  106. A. G. Winkler, X.; Siddiqui, H. R.; Hagans, P.L.; Yates, J. T., "Kinetics and energetics of oxygen adsorption on Pt(111) and Pt(112)-a comparison of flat and stepped surfaces," *Surf. Sci.* **201**, 419-443 (1988).
  107. N. K. Freyer, M.; Pirug, G.; Bonzel, H. P., "Oxygen adsorption on Pt (110) - (1x2) and Pt (110) - (1x1)," *Surf. Sci.* **166**, 206-220 (1986).
  108. W. Eberhardt, T. Upton, S. Cramm, and L. Incoccia, "Inner valence levels as a structural probe for chemisorbed molecules: O<sub>2</sub> on Pt(111)," *Chem. Phys. Lett.* **146**, 561-565 (1988).

- 
109. A. C. W. Luntz, M.D.; Bethune, D. S., "The sticking of O<sub>2</sub> on a Pt(111) surface," J. Chem. Phys. **89**, 4381-4395 (1988).
110. A. C. Luntz, J. Grimboldt, and D. E. Fowler, "Sequential precursors in dissociative chemisorption: O<sub>2</sub> on Pt(111)," Phys. Rev. B **39**, 12903-12906 (1989).
111. A. Eichler, F. Mittendorfer, and J. Hafner, "Precursor-mediated adsorption of oxygen on the (111) surfaces of platinum-group metals," Phys. Rev. B **62**, 4744 - 4755 (2000).
112. M.-L. Bocquet, J. Cerda, and P. Sautet, "Transformation of molecular oxygen on a platinum surface: A theoretical calculation of STM images," Phys. Rev. B **59**, 15 437-15 445 (1999).
113. S. Paavilainen and J. A. Nieminen, "Model calculations of STM imaging and manipulation of oxygen on Pt(111)," Surf. Sci. **521**, 69 -76 (2002).
114. N. K. Ray and A. B. Anderson, "Molecular orbital study of CO chemisorption and oxidation on a Pt(111) surface," Surf. Sci. **119**, 35-45 (1982).
115. T. Jacob, R. P. Muller, and W. A. Goddard, "Chemisorption of atomic oxygen on Pt(111) from DFT studies of Pt-clusters," J. Phys. Chem. B **107**, 9465-9476 (2003).
116. M. Tutuianu, O. R. Inderwildi, W. G. Bessler, and J. Warnatz, "Competitive adsorption of NO, NO<sub>2</sub>, CO<sub>2</sub> and H<sub>2</sub>O on BaO(100): A quantum chemical study," J. Phys. Chem. B **110**, 17484-17492 (2006).
117. O. R. Inderwildi: *Multiscale modelling for automotive exhaust-gas aftertreatment*, Ph.D. Thesis (University of Heidelberg, 2005).
118. C. Kittel, *Introduction to solid state physics*, 6 ed (Wiley, New York, 1986).
119. Q. Ge and D. A. King, "Surface diffusion potential energy surfaces from first principles:CO chemisorbed on Pt.110.," J. Chem. Phys. **111**, 9461-9464 (1999).
120. R. A. v. Santen and M. Neurock, "Concepts in theoretical heterogeneous catalytic reactivity," Catal. Rev. Sci. Eng. **37**, 557-698 (1995).
121. R. A. v. Santen, M. C. Zonneville, and A. P. J. Jansen, "The quantum-chemical basis of the catalytic reactivity of transition metals," Phil. Trans. R. Soc. Lond. A **341**, 269-281 (1992).
122. A. Michaelides, Z.-P. Liu, C. J. Zhang, A. Alavi, D. A. King, and P. Hu, "Identification of general linear relationships between activation energies and enthalpy



- changes for dissociation reactions at surfaces," *J. Am. Chem. Soc.* **125**, 3704-3705 (2003).
123. J. K. Nørskov, T. Bligaard, A. Lagadottir, S. Bahn, L. B. Hansen, M. Bollinger, H. Bengaard, B. Hammer, Z. Sljivancanin, M. Mavrikakis, Y. Xu, S. Dahl, and C. J. H. Jacobsen, "Universality in heterogenous catalysis," *J. Catal.* **209**, 275-278 (2002).
124. J. Wintterlin, R. Schuster, and G. Ertl, "Existence of a "hot" atom mechanism for the dissociation of O<sub>2</sub> on Pt(111)," *Phys. Rev. Lett.* **77**, 123-126 (1996).
125. A. Bogicevic, J. Strömquist, and B. I. Lundqvist, "First-principles diffusion-barrier calculation for atomic oxygen on Pt(111)," *Phys. Rev. B* **57**, 4289-4292 (1998).
126. J. K. Nørskov, J. Rossmeisl, A. Logadottir, L. Lindqvist, J. R. Kitchin, T. Bligaard, and H. Jónsson, "Origin of the overpotential for oxygen reduction at a fuel-cell cathode," *J. Phys. Chem. B* **108**, 17886-17892 (2004).
127. K. S. Kabin, R. L. Muncrief, and M. P. Harold, "NO<sub>x</sub> storage and reduction on a Pt/BaO/alumina monolithic storage catalyst," *Catalysis Today* **96**, 79-89 (2004).
128. Y. Su and M. D. Amiridis, "In situ FTIR studies of the mechanism of NO<sub>x</sub> storage and reduction on Pt/Ba/Al<sub>2</sub>O<sub>3</sub> catalysts," *Catalysis Today* **96**, 31-41 (2004).
129. P. Broqvist, H. Grönbeck, E. Fridell, and I. Panas, "NO<sub>x</sub> storage on BaO: theory and experiment," *Catalysis Today* **96**, 71-78 (2004).
130. L. Olsson, B. Westerberg, H. Persson, E. Fridell, M. Skoglundh, and B. Andersson, "A kinetic study of oxygen adsorption/desorption and NO oxidation over Pt/Al<sub>2</sub>O<sub>3</sub>," *J. Phys. Chem. B* **103**, 10433-10439 (1999).
131. A. Scotti, I. Nova, E. Tronconi, L. Castoldi, L. Lietti, and P. Forzatti, "Kinetic study of lean NO<sub>x</sub> storage over the Pt-Ba/Al<sub>2</sub>O<sub>3</sub> system," *Ind. Eng. Chem. Res.* **43**, 4522-4534 (2004).
132. U. Tuttlies, V. Schmeißer, and G. Eigenberger, "A mechanistic simulation model for NO<sub>x</sub> storage catalyst dynamics," *Chem. Eng. Sci.* **59**, 4731-4738 (2004).
133. C. G. Vayenas, S. Brosda, and C. Pliangos, "The double-layer approach to promotion, electrocatalysis, electrochemical promotion, and metal-support interactions," *J. Catal.* **216**, 487-504 (2003).

134. C. G. Vayenas and G. E. Pitselis, "Mathematical modeling of electrochemical promotion and of metal-support interactions," *Ind. Eng. Chem. Res.* **40**, 4209-4215 (2001).
135. B. Luerßen, E. Mutoro, H. Fisher, S. Günther, R. Imbihl, and J. Janek, "In situ imaging of electrochemically induced oxygen spillover on Pt/YSZ catalysts," *Angew. Chem* **45**, 1473-1476 (2006).
136. W. G. Bessler, "A new computational approach for SOFC impedance based on detailed electrochemical reaction-diffusion models," *Solid State Ionics* **176**, 997-1011 (2005).
137. M. Vogler, W. G. Bessler, J. Warnatz, A. Bieberle-Hütter, and L. J. Gauckler, "Towards an understanding of Ni anodes in solid oxide fuel cells: Electrochemical modeling and experimental validation using patterned anodes," in *Proceedings of the 7th European Solid Oxide Fuel Cell Forum*, submitted, Lucerne, Switzerland (2006).
138. O. Deutschmann, S. Tischer, C. Correa, D. Chatterjee, S. Kleditzsch, and V. M. Janardhanan, *DETCHEM Software Package, Version 2.0* (<http://www.detchem.com>, Karlsruhe, 2004).
139. O. Deutschmann, R. Schmidt, F. Behrendt, and J. Warnatz, "Numerical modeling of catalytic combustion," *Proc. Combust. Inst.* **26**, 1747-1754 (1996).
140. D. Chatterjee, O. Deutschmann, and J. Warnatz, "Detailed surface reaction mechanism in a three-way catalyst," *Faraday Discuss.* **119**, 371-384 (2001).
141. R. J. Kee, M. E. Coltrin, and P. Glarborg, *Chemically reacting flow. Theory and practice* (John Wiley & Sons, 2003).
142. F. Behrendt, O. Deutschmann, B. Ruf, R. Schmidt, and J. Warnatz, "Simulation of heterogeneous reaction systems," in *Gas phase chemical reaction systems: experiment and models, 100 years after Max Bodenstein*, J. Warnatz, Editor (Springer, 1996), 265-278.
143. K. Christmann, *Surface physical chemistry* (Steinkopff, Darmstadt, 1991).
144. G. Ertl, H. Knözinger, and J. Weitkamp, eds. *Handbook of heterogeneous catalysis* (VCH, Weinheim, 1997).
145. J. V. Barth, "Transport of adsorbates at metal surfaces: from thermal migration to hot precursors," *Surf. Sci. Rep.* **40**, 75-149 (2000).

146. C. Ratsch and M. Scheffler, "Density-functional theory calculations of hopping rates of surface diffusion," *Phys. Rev. B* **58**, 163-166 (1998).



---

## ***List of Publications***

“Competitive adsorption of NO, NO<sub>2</sub>, CO<sub>2</sub> and H<sub>2</sub>O on BaO(100): A quantum chemical study”, Tutuianu M., Inderwildi O.R., Bessler W.G., Warnatz J., *J. Phys. Chem. B*, 110, 17484-17492 (2006)

“Influence of surface coverage on the oxygen adsorption, dissociation and surface diffusion on platinum (111): a theoretical study”, Tutuianu M., Inderwildi O.R., Bessler W.G., Deutschmann O., Warnatz J., *in preparation* (2007)

“First principle study of surface processes in storage catalytic converters”, Tutuianu M., Inderwildi O.R., Bessler W.G., Warnatz J., 11<sup>th</sup> International Conference on Theoretical Aspects of Catalysis, Schmöckwitz (Berlin), Germany, 11-14/06/2006

“Competitive adsorption of various species relevant in NO<sub>x</sub> storage catalysts on barium oxide”, Tutuianu M., Inderwildi O.R., Bessler W.G., Warnatz J., 39<sup>th</sup> Jahrestreffen Deutscher Katalytiker, Weimar-Germany, 15-17/03/2006

“Competitive Adsorption of NO<sub>2</sub>, CO<sub>2</sub> and H<sub>2</sub>O on BaO(100): A DFT Study”, Tutuianu M., Bessler W.G., Warnatz J., 4<sup>th</sup> International Conference on Environmental Catalysis, Heidelberg-Germany, 5–8/06/2005

“Geometric Aspects of NO<sub>2</sub> Interaction with Barium Oxide (100) studied by DFT”, Tutuianu M., Bessler W.G., Warnatz J., 38<sup>th</sup> Jahrestreffen Deutscher Katalytiker, Weimar-Germany, 16-18/03/2005

“DFT Calculations of Elementary Step Surface Reactions in Catalytic Processes”,  
Tutuianu M., Inderwildi O.R., Bessler W.G., Lebiez D., Warnatz J., Molecular Modelling für  
chemisch-technische Anwendungen, Frankfurt am Main-Germany, 27-28/09/2004

“DFT Calculations of the Interaction of Barium Oxide Surfaces with Different Adsorbates”,  
Tutuianu M., Inderwildi O.R., Lebiez D., Bessler W.G., Warnatz J., 37<sup>th</sup> Jahrestreffen  
Deutscher Katalytiker, Weimar-Germany, 17-19/03/2004

## ***Appendix A: Estimation of the Adsorption Entropy***

In order to calculate the free adsorption energy  $\Delta G_R$  using the results of the DFT calculations, values for the adsorption entropy  $\Delta S_R$  are needed. These values were estimate based on kinetic theory using certain reasonable assumptions, as given in the following.

Following from transition state theory, the forward and reverse rates  $k_f$  and  $k_r$  [1/s] for a chemical reaction (here: adsorption/desorption reaction) are given by

$$k_f = k_f^0 \exp\left(-\frac{E_f}{RT}\right), \quad (1)$$

$$k_r = k_r^0 \exp\left(-\frac{E_r}{RT}\right), \quad (2)$$

where  $k_f^0$  and  $k_r^0$  [1/s] are the preexponential factors and  $E_f^{\text{act}}$  and  $E_r^{\text{act}}$  [J/mol] the thermal activation energies of forward and reverse reaction, respectively. The relationship between these kinetic data and the thermodynamical reaction parameters is given by

$$k_f^0 / k_r^0 = \exp(\Delta S_R / R), \quad (3)$$

$$E_f^{\text{act}} - E_r^{\text{act}} = \Delta H_R, \quad (4)$$

i.e., the reaction entropy is related to the pre-exponential factors and the reaction enthalpy (which is available from DFT calculations) is related to the activation energies.

For a surface adsorption reaction,  $k_f^0$  can be calculated based on kinetic gas theory from the number of gas-phase molecule/surface collisions, weighed with the dimensionless sticking coefficient  $S$  which is the probability that a collision leads to an adsorption.

This results in [141,142]

$$k_r^0 = S \frac{p^0}{\Gamma} (2\pi MRT)^{-1/2}, \quad (5)$$

where  $p^0 = 101325$  Pa,  $\Gamma$  is the surface density of adsorption sites (here we use a value of  $5.37 \cdot 10^{-6}$  mol/m<sup>2</sup>, following from the lattice constant of the Ba(100) surface),  $M$  [kg/mol] is the molar mass of the adsorbing molecule,  $R$  is the universal gas constant and  $T$  [K] is the temperature.

For a surface desorption reaction, it can be assumed that  $k_r^0$  represents the so-called attempt frequency, i.e. the vibrational frequency of the adsorbed species in the direction perpendicular to the surface. Under the assumption that the adsorbed species and the transition state of the desorption reaction have the same partition function, i.e., the same degrees of freedom [143] (which is a reasonable assumptions for a strongly adsorbed species), it can be estimated that [143]

$$k_r^0 = \frac{kT}{h}, \quad (6)$$

where  $k$  is the Boltzmann constant and  $h$  is Planck's constant.

Equations (3), (5) and (6) allow to calculate the temperature-dependent entropy of the adsorption/desorption reaction when the sticking coefficient  $S$  is known. In the present calculations constant sticking coefficients of unity for all species, which is a common assumption for chemisorbed species, were assumed.

Using this approach, calculated reaction entropies for NO<sub>2</sub> adsorption/desorption, for example, vary between -76 J/kmol at 300 K and -94 J/kmol at 1300 K. The entropies are quite negative, which is typical for an adsorption reaction [141]: The largest part of the gas-phase molecule's entropy comes from translational motion, which is lost upon chemisorption.



## ***Appendix B: Calculation of Atomic Oxygen Diffusion Coefficients on the Pt(111) Surface***

The motion of adsorbed atoms or molecules plays an essential role for many surface processes, in particular in heterogeneous catalysis where usually reactant particles adsorb and diffuse on the surface before the product is formed. The process is considered to occur as a random walk across the surface where ad-particles hop between adjacent sites, i.e., from an occupied site to an adjacent empty site [144].

In the following diffusion coefficients  $D$  of atomic oxygen diffusion on Pt(111) were calculated using an Arrhenius formula, according to

$$D = D_0 \exp\left(-\frac{E_a}{RT}\right), \quad (1)$$

with  $D_0$  for the threefold site of an (111) surface:

$$D_0 = \frac{1}{4} \times \nu_0 \times \left(\frac{a}{\sqrt{3}}\right)^2 \quad (2)$$

where:  $\nu_0$  [1/s] is the attempt frequency,  $E_a$  [kJ/mol] is the activation energy for atomic oxygen diffusion of single site jump from an fcc threefold site to an hcp threefold site, obtained from DFT calculations presented in Chapter 5,  $R$  ( $8.314 \times 10^{-3}$  kJ/mol·K) is the universal gas constant,  $T$  [K] is the temperature and  $a$  [m] is the jump length ( $a = 2.8 \times 10^{-10}$  m). When the adsorbate binds at the hollow site of an (111) surface, the jump length is reduced to  $\left(\frac{a}{\sqrt{3}}\right)$  [145]. The attempt frequency  $\nu_0$  [1/s] can be associated with a vibrational

frequency of the adsorbate. It is commonly assumed that  $\nu_0 \sim 1 \times 10^{13}$  1/s and this value was used in the present work [146].

The coverage dependence plays an essential role in surface diffusion and has to be considered. For example, if a particle wants to move to an empty site, the probability to hop depends on the number of empty sites in the neighborhood. Coverage dependences may be introduced through the coverage dependence of the activation energy,

$$D(\theta) = A_0 \exp\left(-\frac{E_a(\theta)}{RT}\right) . \quad (3)$$

In the present work diffusion coefficients of atomic oxygen diffusion from an fcc threefold site to an hcp threefold site on Pt(111) at surface coverages  $\theta$  of 0.125, 0.25 and 0.5 were calculated according to Eqs. (1) and (2). The Arrhenius plot for the obtained diffusion coefficients at temperatures between 100 K and 1000 K is shown in Figure 1:

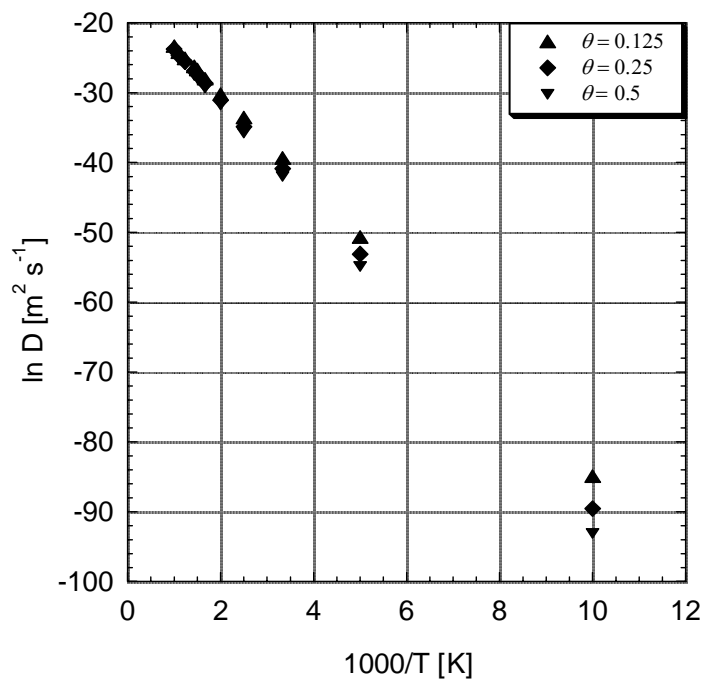


**Fig. 1:** Arrhenius plot for surface diffusion coefficients.

The values of the diffusion coefficients for different surface coverages at  $T = 670$  K are given in Table 1:

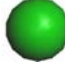


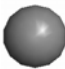

Temperature [K]	Surface Coverage	Diffusion coefficients [m <sup>2</sup> s <sup>-1</sup> ]
670	0.125	$2.45 \times 10^{-12}$
	0.25	$1.23 \times 10^{-12}$
	0.5	$7.30 \times 10^{-13}$

**Table 1:** Diffusion coefficients of atomic oxygen on Pt(111) for surface coverages 0.125, 0.25 and 0.5 at  $T = 670$  K.

The calculated value for the diffusion coefficient of atomic oxygen on Pt(111) is smaller than the reported value by Luerßen *et al.*[135].



**Appendix C: Atom Coloring in Surface Visualizations (Chapters 3, 4 and 5)**

Atom	Visualization
Barium	
Oxygen	
Nitrogen	
Carbon	
Hydrogen	



## ***Acknowledgments***

Looking back to the last three and a half years during my PhD studies, there are many people who contributed to this work and to whom I am grateful and I would like to thank.

First of all, I would like to thank Prof. Jürgen Warnatz to offer me the PhD position. Thank you, Prof. Warnatz, for this great opportunity, thank you for the supervision, for guidance of this work and for the great science in the Reactive Flow Group.

Financial support from the Deutsche Forschungsgemeinschaft through the International Graduate College 710 gave me the opportunity of the international collaboration with Poland is gratefully acknowledged. I am thankful to Prof. Jerzy Gorecki (Institute of Physical Chemistry, Polish Academy of Science, Warsaw, Poland) for many discussions and his critical points. I am grateful also to Wojciech Grochala (ICM, Warsaw University) and Jacek Piechota (ICM, Warsaw University) for helpful discussions and support of this work. Thanks also to Anna Trykozko and all colleagues from ICM for friendly accommodation, making the stays in Warsaw so pleasant.

I am very much indebted to my mentor, Wolfgang G. Bessler, for his daily assistance, guidance throughout this work, encouragements, friendly support in the hard moments during my PhD studies and also for the careful revision and correction of this thesis at the end. I have learned so much from you and I could not have hoped for more support. Thank you, Wolfgang!

I am also very thankful to Oliver Inderwildi for many fruitful discussions and for the introduction to CASTEP making *Density Functional Theory* so pleasant.

I gratefully acknowledge Prof. Olaf Deutschmann for giving me the possibility to collaborate in an industry research project in the framework of the Forschungsvereinigung Verbrennungskraftmaschinen (FVV).

I would also like to thank to Marcel Vogler for the introduction to DENIS, for many nice discussions and his suggestions.

To Priv. Doz. Dr. Uwe Riedel many thanks for all the help in solving financial problems.

To my Heidelberg colleagues, the Reactive Flow group, thank you for your support and the nice atmosphere at work and also during the social events.

To Ingrid Hellwig: Thank you for the help in solving administrative problems.

To my friends: Sasha, Lilia, Cris, Cani, Mona, Julien, Oana, Radu, Mihaela, Razvan, Monica, Nicolae, Jens, Steffen, Dan, Oxana, Georgiana, Naşul Nucu, Naşa Mona, Naşul Calin, Ella, for their encouragements and keeping me in a good mood. Thank you all!

Last but not least, I thank my family who has been by my side during these years, and to which this thesis is dedicated. To my parents (Neculai and Neculina), my brother (Catalin) and my sister (Carmen); thank you for your support. To my husband (Florin) for his continuous encouragements, his patience during my PhD studies (which seemed much longer than three and a half years) and his love (I love you too).



## **Eidesstattliche Erklärung**

Hiermit versichere ich, dass ich die vorgelegte Dissertation selbständig verfasst und keine anderen als die angegebenen Quellen und Hilfsmittel verwendet habe.

Heidelberg, den 24. 05. 2007

Monica Țuțuianu

